Universidade Federal do Espírito Santo

Programa de Pós-Graduação em Astrofísica, Cosmologia e Gravitação

Dark matter, modified gravity and galaxy rotation curves analyses: Novel methods

Alejandro Hernández-Arboleda

Thesis submitted as part of the requirements for the degree of
Doctor of Philosophy in Astronomy & Physics

Supervisor: Prof. Davi C. Rodriges
PPGCosmo, Universidade Federal do Espírito Santo (Brazil)

Co-supervisor: Prof. Luca Amendola
Institut für Theoretische Physik, Heidelberg University (Germany)

2023

Universidade Federal do Espírito Santo
Centro de Ciências Exatas
Programa de Pós-Graduação em Astrofísica, Cosmologia e Gravitação

Dark matter, modified gravity and galaxy rotation curves analyses: Novel methods

Alejandro Hernández-Arboleda

A presente tese "*Dark matter, modified gravity and galaxy rotation curves analyses: Novel methods*" foi submetida por *Alejandro Hernández-Arboleda* ao PPGCosmo, tendo sido apresentada e aprovada no ano de 2023 como parte dos requisitos para a obtenção do título de Doutor em Astronomia e Física.

Comissão avaliadora:

Prof. Dr. Davi Cabral Rodrigues (UFES/PPGCosmo), orientador, presidente da banca,
Prof. Dr. Luca Amendola (Ruprecht-Karls-Universitat Heidelberg/PPGCosmo), co-orientador,
Prof. Dr. Nadja (to be defined), examinador externo,
Prof. Dr. Karin (to be defined), examinador externo,
Prof. Dr. Valerio Marra (UFES/PPGCosmo), examinador externo,
Prof. Dr. Martin Makler (CBPF/PPGCosmo), examinador interno,
Prof. Dr. Oliver F. Piatella (UFES/PPGCosmo), examinador interno.

Abstract

The current ΛCDM cosmological model considers dark matter to be the most abundant type of matter on the universe, encompassing approximately 26.8% of it. As its name suggests, dark matter cannot be directly observed by means of electromagnetic radiation, it only interacts through gravitational fields. Historically, the discover of dark matter was made based on the study of the internal dynamics of clusters of galaxies and galaxy rotation curves. The latter provide the most precise local determination of dark matter. Currently, they continue to be one the main ways to study dark matter not only in the context of the ΛCDM but also modified theories of gravity. Here, we focus on the study of galaxy rotation curves in the context of modified gravity theories in two different but related ways: the first is an alternative approach to test whether modified gravity theories can provide or not a good fit for galaxies without previously needing individual fits. And the second one is a more focused study on a specific modified gravity theory called Vainshtein Screening. Our goal is to both develop a fast way to test viability of modified theories of gravity with rotation curves, and then focus on a specific modified gravity theory which is so far poorly explained with rotation curve data.

Keywords: Modified gravity – rotation curves – dark matter – bayesian analysis – vainshtein screening

---

Resumo

O atual modelo cosmológico ΛCDM considera a matéria escura o tipo de matéria mais abundante no universo, abrangendo aproximadamente 26.8% dele. Como o próprio nome sugere, a matéria escura não pode ser observada diretamente por meio de radiação eletromagnética, ela apenas interage através de campos gravitacionais. Historicamente, a descoberta da matéria escura foi feita com base no estudo da dinâmica interna de aglomerados de galáxias e das curvas de rotação das galáxias. Estes últimos fornecem a determinação local mais precisa da matéria escura. Atualmente, as curvas de rotação continuam a ser uma das principais formas de estudar a matéria escura não apenas no contexto do ΛCDM, mas também de teorias modificadas da gravidade. Aqui, nos concentramos no estudo das curvas de rotação de galáxias no contexto das teorias da gravidade modificada de duas maneiras diferentes, mas relacionadas: a primeira é uma abordagem alternativa para testar se as teorias de gravidade modificada podem fornecer ou não um bom ajuste para galáxias sem a necessidade prévia de ajustes individuais. E a segunda é um estudo mais focado em uma teoria específica da gravidade modificada chamada blindagem de Vainshtein. Nosso objetivo é desenvolver uma maneira rápida de testar a viabilidade de teorias de gravidade modificadas com curvas de rotação e, depois disso, focar em uma teoria de gravidade modificada específica que até agora é deficientemente explicada com dados de curvas de rotação.

Palavras chave: gravidade modificada – curvas de rotação – matéria escura – análise bayesiana – vainshtein screening

---

List of Papers

During my PhD, I have performed research in modified theories of gravity, focusing on determining the viability of them by using mostly individual galaxy rotation curves and data analysis. This has led me to publish three papers in different scientific journals, and there are two more currently under preparations. Here, I list the papers that are included in this thesis.

- Rodrigues, Davi C., and **Hernández-Arboleda, Alejandro**, "Rotação de galáxias e matéria escura", *Cadernos de Astronomia*, vol. 2, 2021, doi:10.47456/Cad.Astro.v2n1.33939
- Rodrigues, Davi C., **Hernández-Arboleda, Alejandro**, and Wojnar, Aneta, "Normalized additional velocity distribution: Testing the radial profile of dark matter halos and MOND", *Physics of the Dark Universe*, vol. 41, 2023, doi:10.1016/j.dark.2023.101230 [$arXiv : 2204.03762$]
- **Hernández-Arboleda, Alejandro**, Rodrigues, Davi C., Toniato, Júnior D., and Wojnar, Aneta, "Palatini $f(R)$ gravity tests in the weak field limit: Solar System, seismology and galaxies", *International Journal of Geometric Methods in Modern Physics*, vol. 0, 2023, doi:10.1142/S0219887824500282 [$arXiv : 2306.04475$]
- **Hernández-Arboleda, Alejandro**, Rodrigues, Davi C., and Amendola, Luca, "Vainshtein Screening and Galaxy Rotation Curves". In preparation for future publishing.
- Rodrigues, Davi C., **Hernández-Arboleda, Alejandro**, and Wojnar, Aneta, "Normalized additional velocity II: testing the radial profile of modified theories". In preparation for future publishing.

Acknowledgments / Agradecimentos

I would like to thank Prof. Dr. Davi Rodrigues, my supervisor, for all the support and guidance provided during my PhD. I also want to thank Prof. Dr. Luca Amendola, my co-advisor, for his very warm welcome to his group in Heidelberg, as well as for his support during my stay visit to the ITP Heidelberg and his willingness to help me. I would like to thank the CAPES foundation for funding my PhD's scholarship and I would also like to thank both CAPES and the German Academic Exchange Service DAAD for funding my stays in Heidelberg, Germany.

This work made use of the CHE cluster, managed and funded by COSMO/CBPF/MCTI, with financial support from FINEP and FAPERJ, and operating at the Javier Magnin Computing Center/CBPF. The authors would like to acknowledge the use of the computational resources provided by the Sci-Com Lab of the Department of Physics at UFES, which was funded by FAPES (Brazil, TO 1081/2022).

Contents

CHAPTER 1

Introduction

Two of the biggest scientific and philosophical questions in the history of human beings are "Who we are?" and "Why are we here?". Pondering deeply about those fundamental questions is far beyond the scope of this work and, maybe, beyond any individual human mind, but it is currently clear that a relevant ingredient for the existence of life as we know on Earth is either the presence of dark matter, or some gravitational effect that mimics it. According to the current standard understanding of cosmology, without that elusive material content of the Universe, which is about five times more abundant than ordinary baryonic matter, nothing as we know could exist because all gravitationally bound structures in the universe, such as the Milky Way and all other galaxies, could have never formed.

Here we try to contribute a grain of sand to the scientific study of dark matter, and even to the study of gravity theories beyond general relativity. On that regard, galaxy rotation curves were the pioneer tool to both suggest the existence of dark matter, and also to study its general properties [1, 2, 3, 4, 5]. They currently continue to be one of the main ways to study the effects of dark matter at the scale of galaxies or even galaxy clusters. Galaxy clusters are out of the scope of this work, therefore, the main focus will be galaxy rotation curves, an example of which is shown in Figure 1.1.

Despite the fact that the dark matter paradigm is well established, and also the methodology for galaxy rotation curves has been greatly developed since the initial works of Oort in the 1940 decade and Rubin in the 1970 decade, there are still some unresolved issues in this research field. One of such issues deals with the computational resources required either to test whether a particular dark matter profile provides a good fit for a galaxy sample, or how different profiles compare to each other. Although the Navarro-Frenk-White (NFW) profile [8] is generally the standard dark matter profile used for many applications, there are several other alternatives to it, including the generalized Navarro-Frenk-White (gNFW) profile, the Einasto profile, the Burkert profile, among others. Determining the best fit parameters for a single profile over several galaxies can be challenging and very time consuming, even more when several profiles are to be compared. And occasionally, the output of several lengthy tests can just be that a particular profile does not provide a good fit for the vast majority of the galaxies in a sample. In light of that predicament, in this thesis we propose an alternative fast way to determine the viability of a dark matter profile using the collective data of a galaxy sample, and not the individual galaxy fits. Our proposal is not only significantly faster to determine whether a profile provides a good fit for the overall sample or not, but also allows one to quickly compare the performance of one profile against other. It is not intended to be a replacement of individual fits, but a handy tool

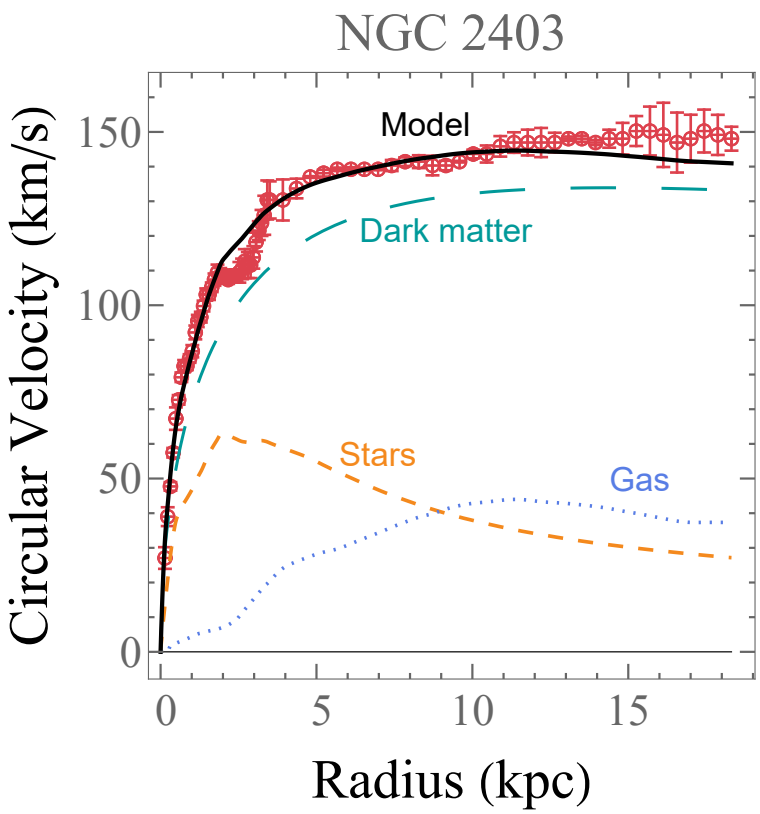

Figure 1.1: Rotation curve example. For this example, the data corresponds to the galaxy NGC 2403 [6], the fit and the overall image were generated with the MAGMA code [7], assuming a particular dark matter halo (the Navarro Frenk White or NFW halo). The red points with error bars are the observational data for the circular velocity, the dotted blue line is the atomic gas contribution (hydrogen and helium), the short dashed orange line is the stellar contribution, the long dashed green line is the dark matter halo contribution, and finally, the solid black line is the best fit for the entire model, including both the baryonic and non-baryonic matter. The entire model contribution is calculated from the square root of the sum of the squares of the individual components, not a simple sum.

to use before them in order to be more efficient in the process of determining whether a profile is good or not for a determined sample of galaxies.

Apart from that, we also use galaxy rotation curves to test a particular effect in modified gravity theories called Vainshtein screening. In a broad sense, modified theories of gravity generally introduce a "fifth force" which is capable to properly explain some features of rotation curves than Newtonian gravity cannot, such as the plateau that many rotation curves show towards the outskirts of the galaxy. If that fifth force were to act equally at all locations inside a galaxy, the modified theory could properly explain stringent restrictions coming, for example, from solar system test (see [9] for an updated review), among others. Therefore, a screening or "shielding" mechanism generally acting at smaller scales withing the galaxy, is required to allow the modified theory to be feasible. Vainishtein screening is one of such mechanisms, and we show our prelim-

inary results of exploring the actual effects of such mechanism when incorporated in the galaxy rotation curve analysis. Again, our goal is not to completely substitute dark matter with the modified theory of gravity, but just to evaluate by how much the amount of dark matter inside a galaxy is changed when incorporating the screening mechanism into the model.

Having stated our main objectives, this thesis is organized as follows. In Chapter 2 we will present the general theory, foundations and methodology for measuring rotation curves. Although this work does not explicitly deal with measuring the data used, understanding the basics of how the measurements are done is crucial for latter interpreting the results of our studies. Then, in Chapter 3, we specifically present the actual data that we used in our investigation, focusing on the most relevant aspects that we will be using on our studies. Then the following two chapters show the original contributions made by this work: in Chapters 4 we present the so-called Normalized Additional Velocity (NAV) method for studying dark matter models using collective rotational curves data, and in Chapter 5 we show some preliminary results of an ongoing investigation on screening effects at the scale of galaxies, something that has been primarily theoretically done in recent years, and put to test with some specific modified gravity models such as $f(\mathrm{R})$ gravity, but to our knowledge, this will be one of the first studies specifically targeting the effects of screening gravity modifications onto the dark matter content of galaxies inferred from rotation curves. Finally, our conclusions are presented in Chapter 6.

CHAPTER 2

Brief history and introduction to rotation curves

2.1 Galaxies

2.1.1 History of the "galaxy" denomination

Historically, galaxies have always marveled both scientific and non scientific minds, specially when they are displayed in an artistic way such as depicted in Figure 2.1. Until the 20th century, all

Figure 2.1: Example of NGC4414 galaxy. Image created by The Hubble Heritage Team (AURA/STScI/NASA)NASA Headquarters - Greatest Images of NASA (NASA-HQ-GRIN) - http://nix.larc.nasa.gov/info;jsessionid=1sl2so6lc9mab?id=GPN-2000-000933&orgid=12http://imgsrc.hubblesite.org/hu/db/images/hs-1999-25-a-full_tif.tif, Public Domain, https://commons.wikimedia.org/w/index.php?curid=127019.

such objects were called nebulae. The french astronomer Charles Messier (1730-1817) made the

famous "*Catalogue des Nébuleuses et des Amas d'Étoiles*", a compendium of 110 non-comet objects (comets were the primary interest of Messier), some of which continue to be named according to their number in the catalog. For example, object M87 in the catalog is a giant elliptic galaxy, with almost perfect spherical shape, which recently gained substantial popularity due to the image of its supermassive black hole [10].

Galaxies were only named that way after it was clear that the distance to some of the "nebulae" was much larger than the typical stars observed. Therefore, our own galaxy, the Milky Way, was a large set of stars, including the Sun, and the other galaxies were separated "islands" in the universe. This was only made clear by the works of Oepik and Hubble in the 20th century [11, 12]. Specifically, in the year of 1923, Edwin Hubble proved, based on observations of Cefeids stars [13, 14], that the Andromeda galaxy (M31) was much farther that previously thought.

Hubble introduced a new galaxy classification which is still used today [15], with some concrete modifications suggested by De Vaucouleurs[16] and Sandage [17]. The four general categories for the galaxies in Hubble classification are elliptical, lenticular, spiral and irregular galaxies, and the full classification can be seen in Figure 2.2.

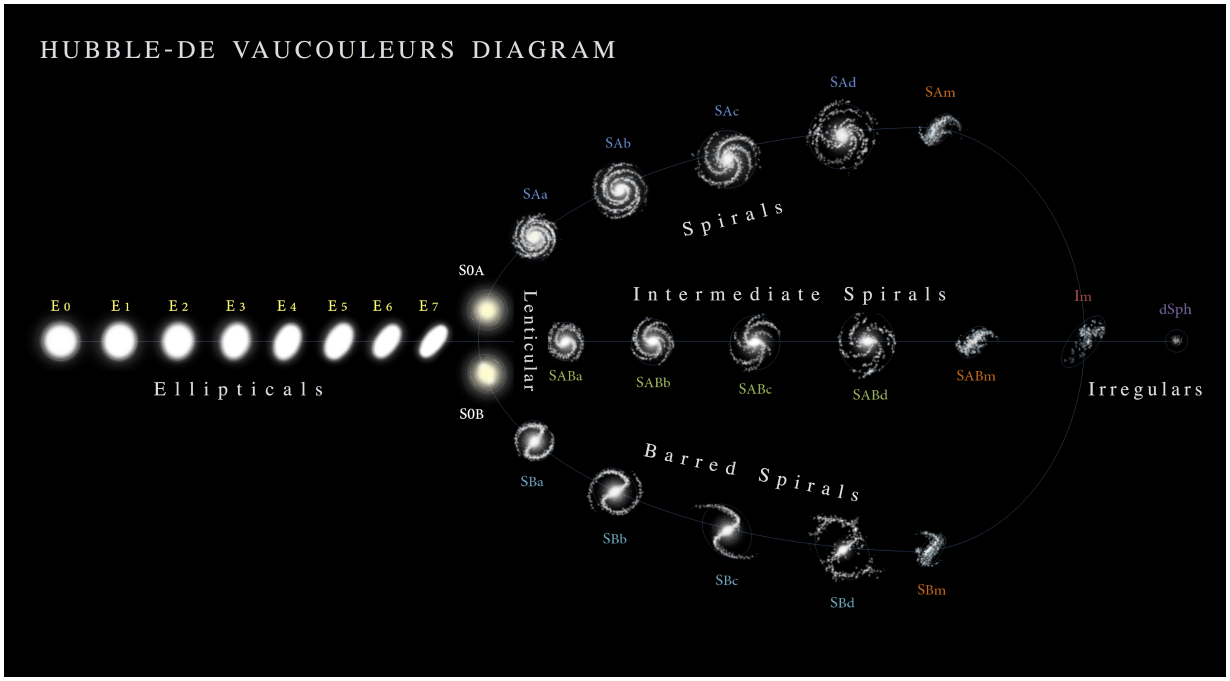

Figure 2.2: Hubble-De Vaucouleurs galaxy Classification. The SIMBAD (simbad.u-strasbg.fr/simbad) can be used to find the classification of any galaxy according to the classes presented above. Figure used with Creative Commons license, by Antonio Ciccolella / M. De Leo - https://en.wikipedia.org/wiki/File:Hubble-Vaucouleurs.png,CCBY3.0, https://commons.wikimedia.org/w/index.php?curid=50260841.

2.2 Components of a galaxy

In a broad sense, galaxies are a large compendium of stars, gas and dark matter held together by the gravitational force between its own components. Stars are the most evident of the constituents because of its brightness, nevertheless, the conversion of brightness measurements to stellar mass is not trivial, but several advancements have been made in order to achieve that conversion.

2.2.1 Stellar component

The mass of a single star can be estimated by means of comparing its individual spectrum with other stars whose mass is known. That process can be done for stars in the Milky Way or in its satellite galaxies, but for other galaxies, the spectrum is observed as a composite. To estimate the mass from a composite measure of brightness, a star population model is required. In essence, the higher the flux intensity, the higher the stellar mass is, but the measurements can be affected by the frequency of the observed light, extinction effects and the stellar population on each region. Detailed reviews about the measurements can be found in [18, 19, 20, 21], but the key point is that the conversion can be made through a proportionality factor Γ_X, generally called the mass-to-light ratio for the band or frequency interval X. The mass-to-light ratio can be defined for both the stellar disk and the stellar bulge (in case there is one), but since the latter one is less abundant in the SPARC sample that we use for our analysis, we will mainly refer here to the disk one. This proportionality factor is only locally constant, but for some frequencies, Γ can be approximated as single constant for the entire galaxy. That is precisely the case for the $3.6\mu m$ observations by the Spitzer satellite, which is the infrared region [22].

The surface brightness density $I(R)$ of the stellar disk of the vast majority of disk galaxies can be modeled with an exponential function of the form [5]

$$I(R) = I_0 e^{-R/h}, \tag{2.1}$$

and the total luminosity L, for a given frequency interval, is given by

$$L = 2\pi \int_0^{R_{lim}} I(R) R \, dR, \tag{2.2}$$

where R is the radial position measured from the center of the galaxy ($R = 0$), I_0 is a constant, h is the disk scale length, and R_{lim} defines the maximum integration limit used computational simplicity. For example, using $R_{lim} = 5h$ only yields a result 4% lower than $R_{lim} = \infty$. This exponential disk approximation is especially good for larger radii, while for smaller radii, it describes the average behavior but with a higher dispersion, normally related to the possibility for the existence of a bulge.

Although the presence of a stellar bulge typically has no significant relevance for the overall dynamics of a galaxy, it is particularly relevant and dominant towards the center of it. The bulge is typically modeled with a Sérsic profile given by [23]

$$I(R) = I_e e^{-b_n \left[\left(\frac{R}{R_e} \right)^{1/n} - 1 \right]}, \tag{2.3}$$

where I_e, b_n, R_e and n are constants that change from galaxy to galaxy. The effective radius R_e is defined as the radius encompassing half of the total luminosity $l = 2 \times 2\pi \int_0^{R_{lim}} I(R) R \, dR$.

Converting this surface brightness into a mass is not trivial and it requires knowing the geometry the galaxy and Abel transforms [19, 20, 24].

2.2.2 Gas component

It is known that atomic gas is particularly abundant in disk galaxies, specifically, atomic hydrogen H I. Contrary to this, observations have shown elliptical galaxies to have insignificant contributions of that gas [25]. Atomic hydrogen (H I) is particularly important for galaxy rotation curves because it emits a specific type of radiation with 21cm wavelength, that is, within the range of radio waves. The 21cm radiation is due to the hyper-fine structure of the atom, which is due to the interaction between the spin of the nucleus and the surrounding electron cloud. Since the micro-physics of the hydrogen atom is better understood than the radiation of far away stars, and there are no relevant extinction effects for the 21cm radiation, then the conversion from brightness measurements to mass can be simplified.

The H I radiation provides two important properties about the galaxy. The first one is the H I mass density, which can be obtained since that density is directly proportional to the 21cm radiation flux measured. And the second one is the internal kinematics of the galaxy, which can be inferred from the Doppler effect of the detected light. Besides those, a key characteristic of the H I disks is their extension. The H I gas can be detected in regions much farther than the stellar component [19, 26, 27, 28], therefore, they are essential to determine a galaxy mass distribution far away from its center. However, the observations indicate that far away from the center the gas disk changes with the radius, so as the orientation of the main rotation axis. To deal with these perturbations known as warps, Begeman [29] introduced the tilted ring model, which is the main code used to process the measurements leading to rotation curves [30, 31].

2.3 Dark matter component

It is appropriate to mention briefly some of the history of dark matter. In the way it is now used, the denomination of dark matter was introduced by Fritz Zwicky in 1933 [32], while he was working on the Coma galaxy cluster. Zwicky found a significant discrepancy for the mass of the cluster inferred by velocities of the constituent galaxies of the cluster, and the mass derived from the light emitted: the dynamical mass (the one associated to the velocities), was much higher than the one coming from the brightness. Although Zwicky explicitly used the term "dark matter" ("*dunkle materie*"), he did so to refer to non-luminous, ordinary baryonic matter that could not be seen probably due to absorption effects, or because it corresponded to extremely low brightness stars. Recently, the efforts towards understanding the nature of dark matter are rather focused towards it being made of non-ordinary matter, which cannot be directly seen because it does not have electromagnetic interactions but only gravitational ones.

Disk galaxies, such as the Milky Way, rotate at different rates at different radius. In most of such disk galaxies, the motion of visible matter is mainly rotational. That rotational motion is

governed by the general equations 2.4 and 2.5:

$$\Phi(\boldsymbol{r}) = -G \int \frac{\rho(\boldsymbol{r'})}{|\boldsymbol{r} - \boldsymbol{r'}|} d^3 r' \,, \tag{2.4}$$

$$\partial_r \Phi = \frac{V_c^2}{r} \,, \tag{2.5}$$

$$\tag{2.6}$$

where $\rho(\boldsymbol{r})$ is a mass density, $\Phi(\boldsymbol{r})$ is the Newtonian potential generated by it and V_c is the circular velocity. Using these equations for the study of the NGC 3115 galaxy, the astronomer Jan Oort concluded that "the distribution of mass in this system appears to bear almost no relation to that of light" [33]. In summary, the work of Oort suggested the dynamical mass (coming from velocity measurements) was fundamentally different from the luminous mass, therefore, those masses could not have the same nature.

After Oort, astronomers such as Kent Ford, Vera Rubin, Morton Roberts, Robert Whitehurst, among others, went above and beyond on the study of galaxy rotation curves both in the optical and also in the atomic radiation emission (which corresponds to the 21 cm radiation). These astronomers set the foundation for the modern study of galaxy rotation curves, and they further cemented the fact that there was an unknown aspect dominating the rotation curves, specially for long distances from the galactic center.

The discovery of the 21 cm radiation was key for astronomy in general, but specially for the measurement and study of galaxy rotation curves. That radiation is emitted by atomic hydrogen, which is abundant in disk galaxies and can be detected at significantly larger radius than the observed light coming from stars. Only because of the 21 cm radiation was that galaxy rotation curves were able to be extended to much larger radius, that way providing more information about the mass distribution and confirming there was much more mass than the one that could be seen (in the optical).

Beginning in the 80's decade, several other indications emerged about the existence of dark matter, based on many different physical principles. Among those evidences, a few that can be named are X-rays of galaxy clusters, cluster and galaxy lensing, the Bullet cluster [34], the power spectrum of cosmic background radiation, baryonic acoustic oscillations, microlensing for limiting the abundance of non observed compact objects (MACHO's), numerical simulations, among many others. All of those evidences lead to the current framework for dark matter, in which dark matter itself is not ordinary matter because it is not made out of electrons, protons and neutrons. Besides that, it does not have electromagnetic interactions, and it is the main gravitational source present in galaxies, galaxy clusters and even structures at bigger scales than clusters.

There are two main classes of dark matter profiles generally discussed in the literature. The first class is the phenomenological one, which refers to profiles which have been proven to fit well many galaxies, a canonical example of which is the Burkert profile [35], given by

$$\rho_{Burkert}(r) = \frac{\rho_c}{\left(1 + \frac{r}{r_c}\right)\left(1 + \frac{r^2}{r_c^2}\right)}, \tag{2.7}$$

where r_c is core radius and ρ_c the core density are parameters changing from galaxy to galaxy, reflecting its formation properties. It is typically favored by small galaxies with masses of the

order of $\sim 10^8 M_\odot$ but also galaxies of similar size to the Milky Way, at around $\sim 10^{10} M_\odot$. The core name of its parameters is due to the fact that $\rho_{Burkert}(r \ll r_c) \sim \rho_c$, which is precisely the opposite behavior of the other class of profiles.

The second class of DM profiles are the ones motivated by numerical simulations, the most common example of which is the Navarro-Frenk-White profile [8, 36]. The NFW profile is given by

$$\rho_{NFW}(r) = \frac{\rho_s}{\frac{r}{rs}\left(1 + \frac{r}{r_s}\right)^2}, \tag{2.8}$$

where r_s and ρ_s are characterizing parameters for each galaxy. As it can be seen, this profile grows rapidly when $r \to 0$, and this feature is called a cuspy profile, while the Burkert profile is a cored one. The cuspy behavior does not mean numerical simulations lead to an actual infinitely large density at the center, it just indicates that for the resolution of the simulations (which is around $1kpc$), the density keeps increasing when the radius decreases. Fortunately, the mass is finite and well defined for either profile, which is the most relevant aspect when dealing with rotation curves. The aforementioned profiles are the main ones that were used for this work.

2.4 On rotation curves

It was already mentioned that H I radiation is always the main source of the data from which rotation curves are derived, but other measurements can also be considered to improve precision, specially in the inner regions of a galaxy, where H I is scarce. For example, the radiation Hα, which is emitted by the recombination of ionized hydrogen atoms (H II), is typically more abundant in the inner regions of a galaxy. Also, infrared images captured by space telescopes such as Spitzer and WISE in the near infrared region of the spectrum have facilitated precise assessments of the distribution of stellar mass, aiding in the computation of the gravitational field exerted by stars. Therefore, a mix of several measurements, which are images of a galaxy in multiple frequency intervals associated with different radiations, are typically used for the calculation of the rotation curves.

Codes like 3DBarolo [31] are capable of generating the observational galaxy rotation curve data from such images using a model for a particular galaxy. The main model used to analyze those images is the previously-mentioned tilted-ring model. In a nutshell, the tilted-ring model is a technique used in the analysis of galaxy rotation curves, particularly for spiral galaxies, to model the distribution of mass and velocity in their galactic disks. The basic idea is to assume that the disk of the galaxy is composed of concentric, tilted rings, and the motion of the gas and stars within each ring can be described by circular rotation. Each ring is characterized by parameters such as its center, radius, inclination angle, position angle, and finally, the rotational velocity.

By fitting these parameters for a series of concentric rings, the model aims to reproduce the observed rotation curve for a galaxy. The rotation curve data can then be plotted as a function of radial distance from the galactic center, just as exemplified in Figure 1.1. This approach is particularly useful for disentangling the effects of dark matter, gas, and stars in galaxies, and it allows one to infer the distribution of mass within the disk of the galaxy, providing insights into the overall structure and dynamics of spiral galaxies.

It is important to note that having the galaxy inclination radius by radius is crucial in order to obtain the local rotational velocity. This is because the rotational velocity is derived primarily from the 21 cm radiation images along the line of sight. Any information regarding the perpendicular direction to the line of sight is in principle unknown. Therefore, the inclination correction along the principal axis (which is the semi-major axis of the galaxy) is given by

$$V_{\rm c} = \frac{1}{\sin i} V_{l.o.s} \qquad , \qquad \sigma_{V_{\rm c}} = \frac{1}{\sin i} \sigma_{l.o.s}, \tag{2.9}$$

where i is the inclination of the galaxy (or ring), $V_{l.o.s}$ and $\sigma_{l.o.s}$ are the velocity and its respective uncertainty along the line of sight derived from redshift calculations, while $V_{\rm c}$ and $\sigma_{V_{\rm c}}$ are the circular velocity and its respective uncertainty. Further corrections can be introduced due to the angle θ between the semimajor axis in which the galaxy is moving away and any point of interest, but since we do not deal with such corrections in our work, for completeness, we only mention they can be done.

The inclination angle i allows to distinguish two types of galaxies: the face-on galaxies, for which $i = 0°$, position just as we can see the Milky Way, and the edge-on galaxies, which have $i = 90°$. Edge-on galaxies are ideal redshift measurements, since it can be clearly distinguished the receding from the preceding side of the galaxy, but distance measurements are extremely complicated to be estimated with reasonable errors. On the contrary, distance measurements can be done with more precision for face-on galaxies but all rotation curve data will be associated to the perpendicular component to the line of sight, so that $V_{l.o.s} = 0$ and $V_{\rm c}$ cannot be determined.

2.5 Error budgets

It is clear that the tilted-ring model used by 3DBarolo or other codes has many simplifications and reductions made on top of the raw measurements or images of the galaxies in several frequency intervals. That means there are several errors to be accounted for in the calculations. There are three main sources of error regarding the circular velocity. The first source are errors associated to the redshift measurements themselves, which depends on the instrument or telescope used for taking the measurements. These errors are typically low, of the order of only a few km/s. The second source are asymmetries between the receding and preceding sides of the galaxy. If the asymmetry is too big for a given galaxy, then it is discarded from the analysis, but the criteria for discarding a galaxy is usually not uniform across different research groups. Among galaxies which remain, the bigger the discrepancies between the velocities on each side, the bigger the error $\sigma_{V_{\rm c}}$ must be. The third source is associated to the inclination error, which is customary not accounted for in the calculation of $\sigma_{V_{\rm c}}$ and therefore, for any such inclination error, the uncertainty $\sigma_{V_{\rm c}}$ has to be re-evaluated. This is a simple process for global changes of the inclination and more details can be seen [37] as well as Chapters 4 and 5.

2.6 Baryonic rotation curve and dark matter inference

For a typical galaxy, the contribution to the circular velocity ($V_{\rm c}$) contributed by baryonic masses, which are the stellar and gas components of a galaxy, can be expressed as follows:

$$V^2_{bar} = \Upsilon_{\rm bul} |V_{\rm bul}| V_{\rm bul} + \Upsilon_{\rm disk} |V_{\rm disk}| V_{\rm disk} + \Upsilon_{gas} |V_{gas}| V_{gas}, \tag{2.10}$$

where V_{bul}, V_{disk}, and V_{gas} are the velocities contributed by the stellar bulge, stellar disk, and gas disk, respectively. Υ_{bul}, Υ_{disk}, and Υ_{gas} are dimensionless factors (mass-to-light ratios) that scale the contributions based on the total mass of each component as R approaches infinity.

It is important to remark that the process is essentially simple, all that is required is to find the density ρ of a baryonic component, and then the Newtonian potential and circular velocity of that component can be determined using equations 2.4 and 2.5, but undoubtedly, the hardest part is to obtain the density ρ itself. There lies the importance of 3DBarolo and any other code used to accomplish this delicate task.

The stellar contribution is best traced using near-infrared (NIR) images. In some cases, the bulge contribution is negligible, and for late-type disks, inner mass concentrations ("pseudobulges" [38, 39]) can be modeled together with the disk. However, for early-type disks, it is better to separate bulge and disk components due to differences in geometry and stellar populations.

The mass-to-light ratios (Υ_{bul} and Υ_{disk}) can be estimated in various ways, often using stellar population models. These ratios vary depending on the wavelength used for observations and the star formation history. For instance, at Spitzer 3.6 μm, $\Upsilon_{bul} \sim 0.7 - 1.0$, and $\Upsilon_{disk} \sim 0.3 - 0.7$. For galaxies on the star-forming main sequence, a reasonable assumption is $\Upsilon_{disk} \simeq 0.5$ with a 25% variability. The specific values for these quantities, are crucial for our studies, specifically, for Chapter 4 and Chapter 5.

The gas contribution is mainly determined by atomic hydrogen (H I). The conversion from H I luminosity to H I mass is well understood from atomic physics, and Υ_{gas} should consider Helium and heavier elements. Depending on gas metallicity, $\Upsilon_{gas} \sim 1.34 - 1.41$ (see [40]). Uncertainty in V_{gas} is mostly due to the absolute H I flux calibration, usually around 10% (see [40]). The smaller contribution of molecular gas can be estimated using CO maps, but often CO and H I data are not available for the same galaxies. Warm ionized gas ($T \simeq 10^4 K$) generally contributes negligibly, while hot ionized gas ($T \simeq 10^6 - 10^7 K$) forms low-density halos extending over hundreds of kiloparsecs, leading to negligible gravitational contribution within the H I disk (see [40] for an extended review about the gas contribution).

Having determined the baryonic contribution to the rotation curve, and with a fixed DM profile, it is natural to ask what is what is the most likely set of parameters that fit an individual galaxy or a sample of them. This is done through Bayesian inference and the minimization of a χ^2 function, a process which will be thoroughly detailed in Chapters 4 and 5. And although not as evident as for Figure 1.1, one constant conclusion always remains, which is that baryons alone are not enough to explain the rotation curves of galaxies and DM is required to explain the dynamics observed in them for the vast majority of spiral galaxies.

CHAPTER 3

SPARC Catalog Detailed

This section introduces the SPARC (Spitzer Photometry & Accurate Rotation Curves) dataset, comprising 175 nearby galaxies. This dataset includes new surface photometry measurements at a wavelength of 3.6 μm and high-quality rotation curves obtained from previous studies involving H I (neutral hydrogen) and Hα (ionized hydrogen) observations. SPARC encompasses a wide variety of galaxy morphology (ranging from S0 to Irr), luminosity (spanning approximately 5 orders of magnitude), and surface brightness (covering about 4 orders of magnitude).

We will summarize the main results presented in [6]. In there, Lelli *et. al.* derive surface photometry measurements at 3.6 μm and investigate structural relationships between the stellar and gas components of these galaxies. They find that both the stellar mass-H I mass relation and the stellar radius-H I radius relation exhibit significant intrinsic scatter, while the H I mass-radius relation is exceptionally tight and exhibits little variability.

The authors employ detailed mass modeling techniques to analyze galaxies, allowing for the quantification of the ratio of baryonic mass to observed velocity ($V^2_{\rm bar}/V^2_{\rm obs}$) at different characteristic radii and considering various values of the stellar mass-to-light ratio (Υ_*) at a wavelength of 3.6 μm. Assuming a Υ_* value of approximately $0.5M/L$, as suggested by stellar population models, the study reveals several significant findings.

First, the gas fraction in galaxies exhibits a linear correlation with their total luminosity. This relationship suggests a connection between the amount of gas present in galaxies and their overall luminosity. Second, the study observes a transition from galaxies dominated by stars to those dominated by gas, which roughly corresponds to the shift from spiral galaxies to dwarf irregular galaxies. This alignment with density wave theory implies a connection between the distribution of gas and the morphological characteristics of galaxies. Lastly, the V_{bar}/V_{obs} ratio is found to vary with galaxy luminosity and surface brightness. High-mass, high-surface-brightness galaxies tend to exhibit a nearly maximal ratio, indicating a significant contribution of baryonic mass to the observed velocity. In contrast, low-mass, low-surface-brightness galaxies are characterized by a submaximal ratio, suggesting a lesser impact of baryonic mass on the observed velocity in these systems. These fundamental properties become less evident when assuming lower values of Υ_* (around $0.2M/L$), as suggested by the DiskMass survey [41]. In brighter galaxies, the mean maximum-disk limit is estimated to be Υ_* around $0.7M/L$ at 3.6 μm.

3.1 Introduction

The focus is on understanding the mass distribution in galaxies using rotation curves, which have been crucial in this regard. Atomic hydrogen (H I) is a valuable tool for studying the gravitational potential in galaxies for two main reasons: the first is that H I gas follows nearly circular orbits, directly tracing the gravitational potential because it has low velocity dispersion (around 10 km/s). This means that strong assumptions about velocity tensors, required in studies involving stellar kinematics, are unnecessary in H I studies. The second reason is that H I gas is diffuse and extends beyond the stellar component of galaxies, allowing the gravitational potential to be traced to several effective radii, where dark matter is expected to dominate.

Historically, studies of H I rotation curves have been limited to small galaxy samples due to the time-intensive nature of interferometry H I observations and the modeling of 3D datasets. The mass modeling of galaxies often faces the "disk-halo degeneracy," which results from the difficulty of distinguishing between the contributions of the stellar disk and the dark matter halo to the observed rotation curve. This degeneracy also applies to bulge-dominated spirals and elliptical galaxies. To mitigate this degeneracy, near-infrared (NIR) surface photometry, such as K-band or 3.6 μm measurements, is preferred because they provide a close approximation to the stellar mass. Stellar population synthesis (SPS) models suggest that the stellar mass-to-light ratio (Υ_*) varies less in the NIR than in optical bands and depends weakly on the star formation history of the galaxy [42]. Several models even predict that Υ_* remains nearly constant in the NIR across a wide range of galaxy masses and morphologies, although the overall normalization is uncertain by a factor of about three due to variations in SPS models and assumptions about the stellar initial mass function (IMF).

The whole purpose of the SPARC dataset is to enhance our understanding of mass distribution in galaxies. This dataset consists of 175 galaxies with new surface photometry at 3.6 μm and extensive H I rotation curves sourced from existing literature. Additionally, about one-third of SPARC galaxies have Hα rotation curves from various sources, enabling the study of inner regions at high spatial resolutions. Unlike older samples, SPARC covers a wide range of luminosities, surface brightness, rotation velocities, and Hubble types, making it a representative sample of nearby disk galaxies. SPARC is the most extensive collection of galaxies with both high-quality rotation curves and NIR surface photometry to date.

The SPARC data was used in various papers exploring different aspects of galaxy dynamics and mass distribution. For example, several investigations into the baryonic Tully-Fisher relation (BTFR) [43], the mass discrepancy-acceleration relation in the context of the ΛCDM model [44], and the fitting of different dark matter halo profiles to SPARC rotation curves [45]. This specific review chapter presents the SPARC galaxy sample, derives surface photometry at 3.6 μm, describes the collection of H I and Hα rotation curves, builds mass models, examines scaling relations for stellar and H I components, and explores gas fractions and the degree of baryonic maximality under various Υ_* assumptions.

3.2 Galaxy Sample

This section provides details about the data collection and properties of the SPARC dataset, comprising three key aspects. The first is the kinematic data, that is, the dataset includes more than 200 extended H I rotation curves. These rotation curves were gathered from various sources, including previous compilations, large surveys, and individual studies. The observations were conducted over approximately 30 years, using radio telescopes such as the Westerbork Synthesis Radio Telescope (WSRT), Very Large Array (VLA), Australia Telescope Compact Array (ATCA), and Giant Metrewave Radio Telescope (GMRT).

The second key aspect is the photometric data, for which the authors searched the Spitzer archive and identified useful [3.6] μm images for 175 galaxies. Many of these galaxies are part of the Spitzer Survey for Stellar Structure in Galaxies (S^4G [46]). Additionally, [3.6] μm images from Schombert & McGaugh (2014b) were used for low surface brightness (LSB) galaxies, which are often underrepresented in optical catalogs compared to high surface brightness (HSB) spirals.

The third and final key aspect is the fact that SPARC is not a statistically complete or volume-limited sample, but it is designed to be a representative sample of disk galaxies in the nearby Universe. It aims to cover the widest possible range of properties for galaxies with extended rotation curves.

3.2.1 General Properties

The SPARC dataset constitutes a comprehensive exploration of a myriad of galaxy characteristics, embracing a diverse array of morphologies, luminosities, effective radii, effective surface brightnesses, rotation velocities, and gas content. Morphologically, galaxies within SPARC exhibit a broad spectrum of Hubble types, ranging from $S0$ to Im/BCD, with a notable concentration in the later Hubble types (9 to 10), specifically corresponding to Sm and Im galaxies. This distribution is influenced in part by the tendency of the Hubble classification system to assign LSB (low surface brightness) galaxies to these later stages.

In terms of luminosity, SPARC galaxies showcase a wide range, spanning from approximately 10^7 to 10^{12} times the luminosity of the Sun ($L_{[3.6]}$). The dataset incorporates galaxies with effective radii ranging from around 0.3 to 15 kiloparsecs (kpc) and effective surface brightnesses spanning approximately from 5 to 5000 times the luminosity of the Sun per square parsec ($L_{[3.6]}pc^{-2}$). Rotation velocities among SPARC galaxies exhibit substantial diversity, covering a spectrum from roughly 20 to 300 kilometers per second (km/s).

The gas content of SPARC galaxies, as quantified by the H I mass-to-luminosity ratio ($M_{\rm H\,I}/L_{[3.6]}$), demonstrates a range from 0.01 to 10. Specific types of galaxies are intentionally excluded from the SPARC dataset, namely those with very high luminosities ($L_{[3.6]} > 10^{12}L_{\odot}$), typically observed as gas-poor elliptical galaxies in clusters, and those with very low luminosities ($L_{[3.6]} < 10^{7}L_{\odot}$), typically representing gas-poor spheroidal galaxies near the Milky Way and M31.

While SPARC predominantly comprises late-type galaxies, there is a presence of a few lenticular galaxies in the dataset. Early-type galaxies, especially those with high-density H I disks, have historically received less attention in interferometric H I observations. However, other surveys have unveiled the existence of outer low-density H I disks in certain early-type galaxies [47, 48].

The dataset also reveals a wide variability in the ratio of the extent of the H I disk to the stellar disk among SPARC galaxies, ranging from approximately 1 to 14. This emphasizes the capability of H I rotation curves to provide insights into the gravitational potential at significantly larger radii compared to existing IFU surveys like CALIFA [49] or MANGA [50].

In a comparative analysis with previous estimates, the study introduces values of $R_{\rm H\,I}/R_*$, where R_* is a measure of the extent of the stellar disk. The median value of this ratio across SPARC galaxies is determined to be 1.7, aligning with earlier estimates for different galaxy types. However, variations may arise in dense clusters due to gas-stripping effects.

In summary, the SPARC dataset stands as a rich and diverse compilation of galaxies, offering a valuable resource for the comprehensive exploration of galaxy properties and the intricate mass distribution within galaxies.

3.3 Data Collection and Analysis

3.3.1 Surface Photometry

Homogeneous surface photometry at 3.6 μm was conducted for the 175 galaxies in the SPARC dataset following several procedural steps. Data calibration involved initial flat-fielding and calibration using the standard Spitzer pipeline, with a particular emphasis on the disk scale length (R_d). Subsequently, frames underwent an interactive cleaning process where bright contaminants like foreground stars and background galaxies were masked. Given the prevalence of point sources in [3.6] images, masking was critical, with masked pixels being substituted with the local mean isophotal value to ensure accurate aperture luminosity determination.

Absolute sky values and their errors were estimated using multiple sky-boxes, regions devoid of background/foreground objects. While the standard Spitzer pipeline presented a formal zero-point error below 2%, a more realistic photometric error considered the sky brightness error, which typically dominated uncertainties in surface photometry and aperture magnitudes. The mean error on sky brightness was approximately 3%.

Ellipses were fitted to the frames using a standard Fourier-series least-square algorithm. Pixels above 3σ of the mean isophote were automatically masked and replaced. This step aimed to eliminate unresolved background/foreground objects while preserving genuine asymmetric features in the galaxies. It is noteworthy that low-mass and low-surface-brightness (LSB) galaxies often exhibit irregular morphologies, rendering ellipses a basic approximation of their shape. Errors in

surface brightness profiles primarily stemmed from uncertainties in the sky value.

Curves-of-Growth were constructed by summing both raw and replaced pixels within the best-fit ellipse at a given radius. The proportion of light from replaced pixels ranged from 2% to 15%. To ensure stable curves-of-growth at large radii, where galaxy surface brightness is comparable to the contaminating halos of imperfectly masked sources, aperture values with replaced pixels were substituted with mean isophotal values at large radii, beyond the radius containing approximately 90% of the raw luminosity.

Total magnitudes were calculated using asymptotic fits to the curves-of-growth. Errors were estimated by recalculating total magnitudes with a 1σ variation in the sky value. These total magnitudes assumed a solar absolute magnitude of 3.24 at 3.6 μm.

The effective radius (R_{eff}), encompassing half of the total luminosity, and the effective surface brightness (σ_{eff}), the average surface brightness within R_{eff}, were also computed.

Exponential functions were fitted to the outer parts of the surface brightness profiles to estimate the disk scale length (R_d) and central surface brightness (μ_d). Deviations from exponential profiles were noted in the inner parts of most spiral galaxies due to bulges, bars, and lenses.

3.3.2 Rotation Curves

The SPARC rotation curve dataset consists of 175 rotation curves, primarily derived from Ph.D. theses from the University of Groningen. These rotation curves were obtained using similar techniques and software, making them relatively homogeneous. They were drawn from various publications, and the complete list together with the number of objects of each publication can be seen in the original paper this section is based on [6].

For cases with duplicate galaxies, the most reliable rotation curve was selected. Rotation curves from THINGS and LITTLE-THINGS were not considered for inclusion in the SPARC dataset due to issues of homogeneity. The THINGS and LITTLE-THINGS rotation curves exhibit many small-scale bumps and wiggles that are not observed in other rotation curve samples, possibly arising from non-circular components such as streaming motions along spiral arms. In contrast, SPARC rotation curves are generally smoother but can display large-scale features that directly correspond to features in the surface brightness profile, aligning with the rule of Renzo, which states that there is a corresponding feature in the rotation curve for any feature in the luminosity profile and vice versa.

3.3.2.1 Error budget and rotation curve quality

In the SPARC dataset, errors on the rotation velocities are estimated using the following formula:

$$\delta_V^2 = \sqrt{\delta_{V_{fit}}^2 + \left(\frac{V_{app} - V_{rec}}{4}\right)^2}, \tag{3.1}$$

where δ_V^2 represents the squared error on the rotation velocity, $\delta_{V_{fit}}$ is the formal error obtained from fitting the entire disk, and V_{app} and V_{rec} are the rotation velocities derived separately from the approaching and receding sides of the disk, respectively.

This error estimation takes into account both local deviations from circular motions and global kinematic asymmetries between the two sides of the disk. However, it does not include systematic errors due to the assumed inclination. Changes in inclination (i) would affect the normalization of the rotation curve without altering its shape. Inclination corrections are proportional to sin(i), so they are relatively small for edge-on galaxies but become more significant for face-on galaxies.

The dataset assigns a quality flag (Q) to each rotation curve based on the following scheme:

- Q = 1 is assigned to galaxies with high-quality H I data or hybrid Hα/H I rotation curves (99 objects).
- Q = 2 is assigned to galaxies with minor asymmetries and/or H I data of lower quality (64 objects).
- Q = 3 is assigned to galaxies with major asymmetries, strong non-circular motions, and/or significant offsets between H I and stellar distributions (12 objects).

Galaxies with a Q = 3 flag are not suitable for detailed dynamical studies, but mass models are still provided for completeness. Additionally, face-on galaxies with inclinations (i) less than 30 degrees are excluded from the analysis. This exclusion does not introduce selection bias since galaxy disks are randomly oriented on the sky. Consequently, the final science sample comprises 153 galaxies.

3.3.3 Mass Models

In the SPARC dataset, the methodology for determining contributions from different components to observed rotation curves involves several key steps. The calculation of the gas contribution (V_{gas}) relies on the formula of Casertano [51], addressing the Poisson equation for a disk with finite thickness and an arbitrary density distribution. V_{gas} is obtained either through H I surface density profiles or an approximation assuming an exponential profile with a scale length of 2 times the scale length of the stellar disk (R_d). Notably, molecular gas is excluded due to data limitations but is generally a minor component compared to stars and atomic gas.

The stellar contribution, divided into the disk (V_{disk}) and bulge (V_{bul}), is methodologically determined based on the Hubble type (T) of the galaxy. For galaxies with $T < 4$ (earlier than Sbc), a non-parametric approach is applied. A fiducial radius (R_{bul}) is defined where the bulge dominates in luminosity, and subtracting the stellar disk involves extrapolating an exponential fit to the inner disk structure. V_{bul} is then computed from the residual luminosity profile. For galaxies with $T \geq 4$ (Sbc and later types), it is assumed that all stars lie in a disk, and any light concentration is interpreted as a disky pseudobulge.

The uncertainties in V_{bul} and V_{disk} primarily stem from the chosen stellar mass-to-light ratio (Υ_*). The dataset provides values of V_{bul} and V_{disk} for $\Upsilon_* = 1$, and these values can be adjusted to any desired Υ_*.

The total baryonic contribution to the rotation curve (V_{bar}) is determined by considering individual contributions from gas, stellar disk, and bulge components. The dataset explores the ratio V_{bar}/V_{obs} under various assumptions of Υ_*. Discussions on rotation curve fits with dark matter (DM) halos are detailed separately in [52].

3.4 Dynamical Properties

3.4.1 The Stellar Mass-to-Light Ratio

The major uncertainty in galaxy mass modeling stems from determining the value of Υ_*, which represents the stellar mass-to-light ratio of a galaxy. To address this uncertainty, the DiskMass Survey (DMS) conducted measurements on the vertical velocity dispersion of stars in 30 face-on spiral galaxies. They used a theoretical relation linking vertical velocity dispersion, disk scale height (z_d), and dynamical surface density, which is valid for self-gravitating disks. As z_d cannot be directly measured in face-on galaxies, the DMS statistically estimated it using an empirical correlation between the disk scale length (R_d) and z_d, calibrated using near-infrared (NIR) photometry of edge-on galaxies.

The principal findings from the DMS concerning Υ_* and disk mass can be summarized as follows: Stellar disks in face-on spirals exhibit strong submaximality, contributing less than 30% of the dynamical mass within 2.2 times the disk scale length ($2.2R_d$). This implies a significant influence of dark matter in shaping the dynamics of these galaxies. The initial estimation for Υ_* in the K-band was $0.31M_\odot/L_\odot$, but upon correcting for the dark matter contribution, the value was revised to $0.24M_\odot/L_\odot$ in the K-band. Considering that K-band luminosity (L_K) is approximately 1.3 times the luminosity at 3.6 μm ([3.6]), these values correspond to Υ_* of about $0.2M_\odot/L_\odot$ at [3.6]. Upon a re-analysis of the DMS data, it was noted that when dark matter halos are consistently incorporated, the mean value of Υ_* further decreases to around 0.18 $0.18M_\odot/L_\odot$ in the K-band (approximately $0.14M_\odot/L_\odot$ at [3.6]).

These results conflict with predictions from stellar population synthesis (SPS) models, which suggest higher mean values for Υ_* ranging from approximately 0.4 to $0.8M_\odot/L_\odot$ at [3.6], depending on the specific model and initial mass function (IMF). However, both the DMS and SPS models agree that Υ_* is nearly constant in the near-infrared (NIR) among galaxies of different masses and morphologies. The primary discrepancy lies in the overall normalization of Υ_*.

To address this uncertainty, the authors assume that Υ_* is constant among different galaxies and explore different normalizations. For galaxies with significant bulges, they adopt $\Upsilon_{bul} = 1.4\Upsilon_{disk}$ based on suggestions from SPS models. In their analysis, the different normalizations of Υ_* always refer to the stellar disk, i.e., $\Upsilon_* = \Upsilon_{disk}$. This approach allows for a systematic exploration of the impact of Υ_* on galaxy mass modeling while considering different galaxy morphologies and normalizations.

In summary, the results suggest that assuming $\Upsilon_* = 0.5M_\odot/L_\odot$ provides a more realistic representation of the galaxy population compared to assuming $\Upsilon_* = 0.2M_\odot/L_\odot$. This is in line with previous studies and observations of the gas fraction in galaxies, particularly with respect

to the transition between spiral and irregular galaxies and the extent of gas domination in dwarf irregulars.

CHAPTER 4

Normalized additional velocity distribution

We propose an alternative and efficient method for examining galaxy rotation curves directly from sample data rather than individual fits. This approach involves analytical testing based on a dimensionless difference, denoted as δV^2, between the observed rotation curve and the anticipated curve from baryonic matter. The analysis is conducted as a function of the normalized radius $r_{\rm n}$ (ranging from 0 to 1 for all galaxies). Employing a dataset comprising 153 galaxies from the SPARC galaxy sample, we ascertain the observational distribution of δV^2. Within the range $0.2 < r_{\rm n} < 0.9$, a significant portion of the SPARC data closely aligns with the curve $\delta V^2 = {r_{\rm n}}^{0.42}$. Moreover, approximately 95% of the SPARC data falls between the curves $\delta V^2 = {r_{\rm n}}^{2.2}$ and $\delta V^2 = 2{r_{\rm n}}^{0.38} - {r_{\rm n}}^{1.9}$. To gauge the efficacy of three prevalent dark matter halo models (NFW, Burkert, and DC14), along with a simplified dark matter rotation curve profile (Arctan_α) and a modified gravity model without dark matter (MOND), we compare the observational data distribution with model-derived data. Our findings underscore that the NFW halo model lacks the requisite diversity to faithfully replicate several observed rotation curves. In contrast, Burkert and DC14 models demonstrate better agreement with observational data. Specifically, the lowest δV^2 curves derived from NFW exhibit linearity on the normalized radius ($\delta V^2_{\rm NFW} = r_{\rm n}$), while Burkert yields $\delta V^2_{\rm Bur} = {r_{\rm n}}^2$ irrespective of the halo density parameter ($\rho_{\rm c}$ or $\rho_{\rm s}$). MOND, however, only captures the very central region of the observed distribution, indicative of a lack of necessary diversity, reflected in larger χ^2 values. Future work will extend this methodology to encompass other classes of modified gravity models.

4.1 Introduction

Galaxies offer crucial insights into dark matter-related phenomena, typically explored through a standard approach, aligning various independent probes. This method assumes the cosmological existence of dark matter and postulates that cosmological evolution results in the observed dark matter distribution within galaxies. However, the picture becomes complicated at galactic scales due to the significant impact of baryonic feedback on the dark matter distribution.

Presently, different dark matter halo profiles and modified gravity models vie to explain dark matter-like phenomena in galaxies. Four prominent possibilities under consideration are: i) the Navarro-Frenk-While (NFW) profile derived from N-body dark matter simulations; ii) the Burkert profile, a phenomenological model with a core; iii) the [53] halo (DC14) incorporating hydrodynamical simulations with baryonic feedback; and iv) Modified Newtonian Dynamics (MOND), a well-known modified gravity model. Additionally, for comparison, a less-cited phenomenological option based on an arctan function, referred to as $Arctan_\alpha$, is introduced.

This work introduces a method that tests models using a galaxy sample, focusing on the radial dependence of the dark matter or modified gravity contribution to rotation curves, as opposed to individual fits. The squared additional velocity, denoted as ΔV^2, represents the contribution to

circular velocity not attributable to the anticipated Newtonian baryonic contribution. The normalized additional velocity (NAV), denoted as δV^2, is introduced to study the radial dependence of ΔV^2, reducing the number of model parameters and enabling analytical estimates.

4.2 The method

4.2.1 Outline

The approach involves investigating dark matter or modified gravity models. In the dark matter scenario, the method assesses a given dark matter model using a dataset of galaxy rotation curves by comparing the distinctions between the observed rotation curve (RC) and the baryonic contribution with the dark matter rotation curve contribution. Instead of conducting this analysis on an individual galaxy basis, where uncertainties can be more pronounced, the entire dataset of galaxies is collectively considered. This holistic approach is aimed at providing a broader perspective. Additionally, to streamline the analysis and concentrate on a critical aspect of dark matter halos, the comparison is executed with normalization.

In the context of modified gravity, the method maintains a similar essence. However, in this case, the "baryonic contribution" refers exclusively to the Newtonian baryonic contribution, and the non-Newtonian contribution takes the place of the dark matter contribution. This adjustment allows for a consistent evaluation of the two scenarios while focusing on the specific dynamics of interest.

The observational additional (squared) velocity, $\Delta V^2_{\rm obs}$, is defined as

$$\Delta V^2_{\rm obs} \equiv V^2_{\rm obs} - V^2_{\rm bar}\,. \tag{4.1}$$

and the model additional (squared) velocity, $\Delta V^2_{\rm mod}$,

$$\Delta V^2_{\rm mod} \equiv V^2_{\rm mod} - V^2_{\rm bar}\,. \tag{4.2}$$

In the above, $V_{\rm obs}$ is the the observational RC, $V_{\rm mod}$ is the model RC and $V_{\rm bar}$ is the expected baryonic RC (which is inferred from the stars and the HI regions radiation). To be more explicit,

$$V^2_{\rm bar} = V^2_{*\rm d} + V^2_{*\rm b} + V^2_{\rm gas}\,, \tag{4.3}$$

where $V^2_{*\rm d}$, $V^2_{*\rm b}$ and $V^2_{\rm gas}$ are the squared circular velocity of the following components respectively: stellar disk, stellar bulge and the gas (atomic hydrogen and helium). The mass-to-light ratios are included in these quantities.

These squared velocities are not truly the square of a given physical velocity (this is a common convention), namely

$$V^2_{\rm x}(r) \equiv a_{\rm x}(r)\, r\,, \tag{4.4}$$

that is, the component x contribution is the centripetal acceleration due to the component x times the (cylindrical) radial position r. Hence, since the matter distribution is not spherical, $V^2_{\rm x}$ can be either positive or negative. A negative $V^2_{\rm x}$ means that the component x, in a given radius, reduces the total centripetal acceleration. It is common to use this convention. This detail is relevant depending on the particular model and the particular galaxy considered.

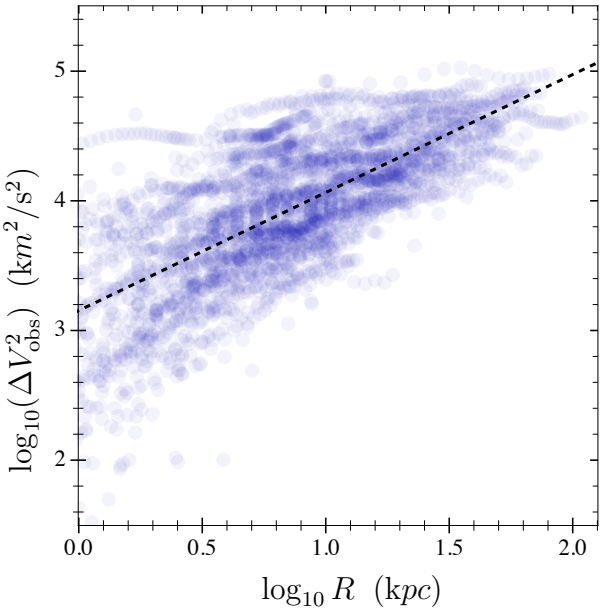

Figure 4.1: The graph depicts the supplementary velocity ($\Delta V^2_{\rm obs}$) for 153 galaxies sourced from SPARC, with fixed values of $Y_{\rm d} = 0.5$ and $Y_{\rm b} = 0.6$. Each data point on the rotation curve is symbolized by a translucent blue disc. The dashed line corresponds to the optimal fit result referenced as (4.6). Image taken from [54].

An analysis on $\Delta V^2_{\rm obs}$ was performed by [55], where it was found the following approximate description[1] $\Delta V^2_{\rm obs} \approx 10^{2.94}\, r\ \mathrm{k}m^2/\mathrm{s}^2$, for $1 < r\,(\mathrm{k}pc) < 74$. This profile was found from 60 galaxies and under assumptions on the stellar mass-to-light ratios that are different from those adopted in the SPARC data. Nonetheless, for the 153 SPARC galaxies we find results that are very similar, namely

$$\Delta V^2_{\rm obs} \approx 10^{3.08}\, r\ \mathrm{k}m^2/\mathrm{s}^2 \ \text{ or,} \tag{4.5}$$

$$\Delta V^2_{\rm obs} \approx 10^{3.15}\, r^{0.91}\ \mathrm{k}m^2/\mathrm{s}^2\,. \tag{4.6}$$

Data with $r < 1$ kpc are neglected, since it is a region with larger dispersion. The first case considers a simpler model, in which $\Delta V^2_{\rm obs}$ is taken as linear on r, like the one adopted by [55], while the latter (4.6) considers a free parameter for the r power. In the end, all the results are similar.

Figure 4.1 displays the analyzed dataset and depicts the final curve. The figure implies that $\Delta V^2_{\rm obs}$ generally increases as the radius increases. However, we note three key considerations about this representation: i) distinct radial zones may exhibit significant variations in the number of data points, ii) the magnitude of $\Delta V^2_{\rm obs}$ for two different galaxies can differ substantially, even if their radial dependencies are similar, and iii) should the magnitude of $\Delta V^2_{\rm obs}$ correlate with the radial span probed by the galaxies, the pattern observed in Fig. 4.1 may not align, even roughly, with the pattern in individual galaxies. Consequently, it is not valid to assume that effective models must adhere to $\Delta V^2_{\rm mod} \propto r$ on average. In fact, a more accurate intermediate radius

[1] This is V_h^2, in their notation.

approximation for the average $\Delta V^2_{\rm obs}$ within the radial scope of observational data for each galaxy would be $\Delta V^2_{\rm mod} \propto \sqrt{r}$, as detailed in Sec. 4.2.2.

The method considered in this paper is based on the normalized additional velocity (NAV) (δV^2) as a function of the normalized radius ($r_{\rm n}$). Namely,

$$\delta V^2(r_{\rm n}) \equiv \frac{\Delta V^2(r_{\rm n}\, r_{\rm max})}{\Delta V^2(r_{\rm max})}\,, \tag{4.7}$$

where $r_{\rm max}$ is the largest radial value with RC data and $r_{\rm n} \equiv r/r_{\rm max}$ is the normalized galaxy radial coordinate, hence $r_{\rm n} \in [0, 1]$.

Alternative model-independent radial values, such as the stellar disk scale length or the effective galaxy radius $r_{\rm eff}$, could be considered for normalizing ΔV^2. However, opting for these alternatives would result in an intermediate radial point where the δV^2 curves from various galaxies intersect. In proximity to this intersection point, there is no pertinent data to extract, as all curves pass through such a point by definition. In contrast, by using $r_{\rm max}$, this intersection occurs at the largest radial value, offering a suitable choice for investigating intermediate radial behavior. Here we will compare the distributions of $\delta V^2_{\rm obs}$, the observational NAV, and $\delta V^2_{\rm mod}$, the model-inferred NAV.

4.2.2 The $\delta V^2_{\rm obs}$ distribution

Figure 4.2 displays the distribution of $\delta V^2_{\rm obs}$ derived from 153 galaxies featured in the SPARC catalogue [6]. These galaxies were the same ones utilized to establish the radial acceleration relation (RAR) [56][2] This figure relies on the central values of galaxy distance and inclination provided by SPARC. Additionally, it assumes that the stellar mass-to-light ratios for the disk and the bulge in the 3.6 μm band from Spitzer are given by $Y_{\rm d} = 0.5$ and $Y_{\rm b} = 0.6$, respectively. The choice for the disk aligns with that of [56], while for the bulge, a slight variation (0.6 instead of 0.7) is adopted, consistent with [22]. Although this choice is reasonable and marginally reduces the negative contribution of $\delta V^2_{\rm obs}$ for small radii, its impact is minor, given that out of the 153 galaxies, 122 lack a significant bulge, and the region with $r_{\rm n} < 0.2$ is not considered in this analysis.

The observational NAV plane, depicted in Fig. 4.2, exhibits a clear correlation, whether including or excluding galaxies with a stellar bulge. This correlation stems directly from the necessity of dark matter or modified gravity. To illustrate this, we first consider the scenario of Newtonian gravity without dark matter. In this case, $V^2_{\rm mod} = V^2_{\rm bar}$, and consequently, $\Delta V^2_{\rm mod} = 0$. In terms of observations, one would anticipate $\Delta V^2_{\rm obs} \sim 0$ in this context, resulting in random oscillations around zero. Therefore, as $\Delta V^2_{\rm obs}(r_{\rm max})$ would be a random number close to zero, the expected $\delta V^2_{\rm obs}$ should fill out the observational NAV plane, encompassing both negative and positive contributions randomly. However, this is clearly not the case for the observational NAV plane inferred from the SPARC data (Fig. 4.2), underscoring the demonstrated correlation and the imperative for dark matter or modified gravity.

[2]The SPARC catalogue initially includes 175 galaxies; however, after excluding those with low inclinations ($i < 30°$) to minimize inclination errors and galaxies deemed not sufficiently symmetric ("quality flag 3"), 153 galaxies remain. The primary RAR plot of [56] also omits data points from certain galaxies (those with a relative uncertainty in $V_{\rm obs}$ exceeding 10%). This step is not considered here, as its effects on this analysis are negligible, particularly in regions with $r_{\rm n} < 0.2$, which will not be examined.

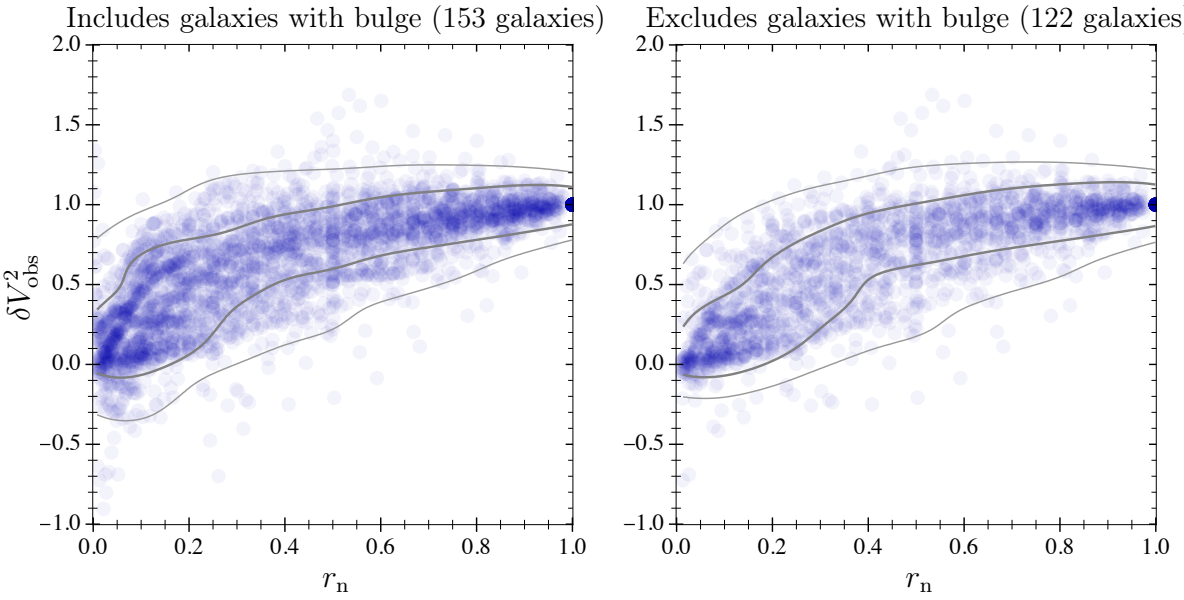

Figure 4.2: **Left plot:** The normalized additional velocity (NAV) plane for 153 galaxies from SPARC with $Y_{\rm d} = 0.5$ and $Y_{\rm b} = 0.6$. Each transparent blue disk represents a data point from a galaxy. The dark blue disk at the point (1, 1) illustrates the superposition of all 153 data points, forming a single point common to all galaxies. The grey curves delineate the 1σ and 2σ highest density regions, determined by a kernel density estimate (KDE) with horizontal and vertical bandwidths set to (0.068, 0.082) following the Silverman rule. **Right plot:** Similar to the left plot, but limited to galaxies without a dynamically relevant bulge, totaling 122 galaxies according to SPARC's classification. The horizontal and vertical bandwidths are adjusted to (0.072, 0.088). Image taken from [54].

To proceed with the method and enable distribution comparisons, we need to derive a smoothed distribution from the data points. A common approach is to utilize a kernel density estimator (KDE). In this work, we employ a Gaussian kernel with the Silverman rule for bandwidths whenever a KDE is applied [57, 58].

Once the KDE for the observational NAV plane is determined, the 1σ and 2σ highest density regions (HDRs) can be identified. These regions encapsulate the majority of the $\delta V^2_{\rm obs}$ data points, representing contours associated with probabilities of 68% and 95%, respectively. These regions are illustrated in Fig. 4.2.

Expectations for good models involve $\delta V^2_{\rm mod}$ distributions resembling $\delta V^2_{\rm obs}$. While a perfect match is not imperative due to observational and KDE errors, it is essential to acknowledge their impact. Errors arising from KDE resolution are notable close to $r_{\rm n} = 0$ and $r_{\rm n} = 1$. To mitigate these issues, we exclude data points within the inferred bandwidth range, particularly neglecting $r_{\rm n} < 0.1$ and $r_{\rm n} > 0.9$. Observational errors near $r_{\rm n} \sim 1$ are inconsequential since, by design, $\delta V^2_{\rm obs}(r_{\rm n} \sim 1) \sim 1$. However, in the vicinity of $r_{\rm n} \sim 0$, where $\Delta V^2_{\rm obs} \lesssim V^2_{\rm bar}$, observational errors significantly influence $\delta V^2_{\rm obs}$. A comparison between the left and right plots in Fig. 4.2, differing in the inclusion of galaxies with a substantial bulge, reveals prominent distinctions for $r_{\rm n} < 0.2$. Consequently, owing to observational and KDE errors, we restrict the $r_{\rm n}$ range of concern to $0.2 < r_{\rm n} < 0.9$.

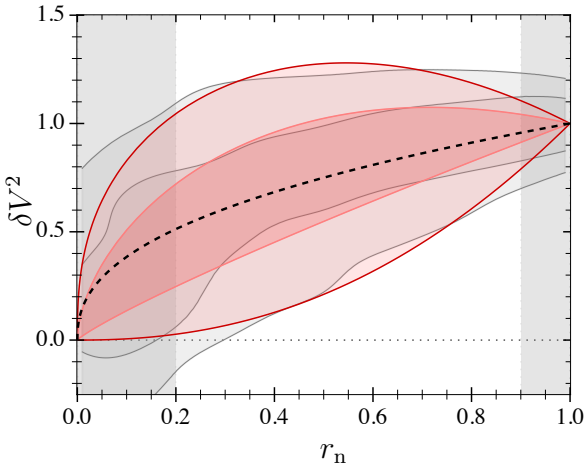

Figure 4.3: A comparison is shown between the 1σ and 2σ regions, as illustrated in Fig. 4.2, utilizing the polynomial models described by eq. (4.8). The vertical shaded regions denote areas excluded from the fits ($r_n < 0.2$ and $r_n > 0.9$), yet the plot incorporates the extensions of curves across all possible r_n values. The dashed black curve represents $(\delta V^2_{obs})_{best}$, the darker red region is bounded by the curves $(\delta V^2_{obs})_{1\sigma_\pm}$, while the lighter red region is delineated by $(\delta V^2_{obs})_{2\sigma_\pm}$. The mean efficiency (4.11) is recorded as $E_M = 0.86$. Image taken from [54].

Understanding simple analytical (polynomial) models capable of approximating the δV^2_{obs} distribution is pertinent, ensuring adherence to constraints such as passing through $(0, 0)$ and $(1, 1)$, as expected in realistic models. Models of the form $\delta V^2 = {r_n}^a$ and $\delta V^2 = 2{r_n}^b - {r_n}^c$, where a, b, and c are constants, are effective for monotonic and non-monotonic curves, respectively. Within the region $0.2 < r_n < 0.9$, we fit these models considering various scenarios: fitting to data from all galaxies collectively (referred to as "best") or to curves describing upper and lower 1σ and 2σ limits. The results are

$$\begin{aligned} \delta V^2_{best} &= {r_n}^{0.42}\,, & & \\ \delta V^2_{1\sigma_-} &= {r_n}^{0.87}\,, & \delta V^2_{1\sigma_+} &= 2{r_n}^{0.58} - {r_n}^{1.66}\,, \\ \delta V^2_{2\sigma_-} &= {r_n}^{2.2}\,, & \delta V^2_{2\sigma_+} &= 2{r_n}^{0.38} - {r_n}^{1.9}\,. \end{aligned} \tag{4.8}$$

The curves above are plotted in Fig. 4.3. Realistic dark matter or modified gravity models are not expect to cover the δV^2_{obs} distribution, in the region $0.2 < r_n < 0.9$, better than this polynomial case, which was built exclusively for this purpose.

4.2.3 The δV^2_{mod} distribution

Frequently, one of the parameters influencing ΔV^2_{mod} is a global multiplicative constant (e.g., ρ_s for the NFW profile, [8]). This parameter, when present, adjusts the magnitude of the dark matter (or modified gravity) contribution. Notably, δV^2_{mod} is independent of such a parameter according to its definition. This characteristic makes δV^2_{mod} commonly dependent on one fewer parameter than the original model—a noteworthy feature of using δV^2_{mod}.

In the initial stages of method application, having an analytical expression of $\delta V^2_{\rm mod}$ before resorting to numerical evaluation proves sufficient for an initial comparison with observational data, as demonstrated in Sec. 4.3.

As a subsequent rapid step, conducting a swift numerical evaluation of extreme parameter cases becomes essential to verify if the region with observational data can be encompassed by the model, at least within specific parameter regions. This task is notably straightforward for two-parameter models, which typically reduce to one-parameter models within the $\delta V^2_{\rm mod}$ analysis.

A third testing phase involves determining the best model curves that replicate the 1σ and 2σ highest density regions (as depicted in Fig. 4.2). The core idea here is to perform a couple of straightforward fits directly to the sample data, in lieu of conducting numerous individual galaxy fits. This approach allows testing whether the model can offer reasonable approximations to such regions and, if possible, identifying the parameter values most commonly required to cover the observational data.

A general procedure to perform the fits described above is by using the following integral,

$$I^{(\pm {\rm k})}(p_i) = \int_0^1 \left(\delta V^2_{\rm mod}(p_i, r_{\rm n}) - \lambda^{(\pm\ {\rm k})}_{\rm obs}(r_{\rm n})\right)^2 \omega(r_{\rm n})\, dr_{\rm n}\,, \tag{4.9}$$

where p_i refers to all the model parameters that $\delta V^2_{\rm mod}$ depends on, $\lambda^{(\pm {\rm k})}_{\rm obs}(r_{\rm n})$ refers to the curve that delimits the kσ region of $V^2_{\rm obs}$, with $+k$ corresponding to the upper limit, and $-k$ with the lower limit. $\omega(r_{\rm n})$ is a weight function. A simple and relevant case, which we adopt here, is $\omega(r_{\rm n}) = \Theta(r_{\rm n} - 0.2)\Theta(0.9 - r_{\rm n})$, where Θ is the Heaviside theta function. Hence, for the latter case, only the data in the range $0.2 < r_{\rm n} < 0.9$ is relevant for the fit.

For certain models, the discrepancy between $\delta V^2_{\rm obs}$ and $\delta V^2_{\rm mod}$ might be significant enough to rule them out as plausible representations. An illustrative instance is Newtonian gravity without dark matter, where the NAV plane would exhibit random distribution. Similarly, specific ranges of the radial parameter in NFW or Burkert profiles can be discounted based on observational data, as extremely low values would lead to curves extending far beyond the observed region. A method for quantifying the similarity between $\delta V^2_{\rm obs}$ and $\delta V^2_{\rm mod}$ is elucidated in Sec. 4.2.4.

In the context of modified gravity theories, $\delta V^2_{\rm mod}$ typically relies on the 3D distribution of baryonic matter for each galaxy, encompassing not only the baryonic circular velocity contributions in the plane but also necessitating the solution of modified Poisson equations. However, there exists a notable modified gravity model, namely the original form of MOND [59], for which $\delta V^2_{\rm mod}$ can be promptly computed using available data. This is possible because $\delta V^2_{\rm MOND}$ can be expressed as a function of the baryonic circular velocity Newtonian contribution ($V^2_{\rm bar}$).

4.2.4 The NAV efficiency

Introducing a numerical comparison between the $V^2_{\rm obs}$ and $V^2_{\rm mod}$ distributions is beneficial. While no single number can encapsulate all the information from the 2D plots, a convenient metric, particularly suitable for our emphasis on the 1σ and 2σ curves, is one based on the respective areas associated with these quantities.

First we introduce three areas:

- $A_{\rm obs}(n)$ is the area of the observational NAV region at $n\sigma$ level.
- $A_{\rm mod\cap obs}(n)$ is the area of the intersection between the model and observational NAV regions at $n\sigma$ level. Hence, a perfect model is expected to satisfy $A_{\rm mod\,\cap\,obs}(n) = A_{\rm obs}(n)$.
- $A_{\rm mod\setminus obs}(n)$ is the area of the region difference between the model and the observational NAV regions, both at $n\sigma$ level. A perfect model should yield $A_{\rm mod\setminus obs}(n) = 0$.

As an initial suggestion for an efficiency coefficient, one could contemplate $A_{\rm mod\cap obs}/A_{\rm obs}$. In this scenario, a perfect model would yield an efficiency of 1, with the lowest possible efficiency being zero, indicating no intersection between the observational and the model NAV regions. While intriguing, there is a need for a penalty system for models predicting regions outside the observational boundaries.

Considering the above, we define the model efficiency at $n\sigma$ level as

$$E_n \equiv \frac{A_{\rm mod\cap obs}(n) - A_{\rm mod\setminus obs}(n)}{A_{\rm obs}(n)}\,. \tag{4.10}$$

Hence, for a given n, the highest efficiency value is $E_n = 1$, and E_n can be arbitrarily negative. Any reasonable model should have positive values for E_n. Models with negative values are those whose predicted area that agrees with the observational data is smaller than the predicted area that is outside the observational region (at the same $n\sigma$ level).

E_n provides a 1D comparison between the model and observational NAV distributions, which is a simplification with respect to the original 2D data. Since we focus on the 1σ and 2σ HDRs, the above model efficiency can be conveniently summarized in a single number as follows, the mean efficiency,

$$E_{\rm M} \equiv \frac{E_1 + E_2}{2}\,. \tag{4.11}$$

This is a number that we will use to compare the models. To avoid the NAV regions where the observational data are less robust, all the areas are computed in the interval $0.2 < r_{\rm n} < 0.9$.

4.2.5 Individual fits

In the comparison presented below, we contrast the NAV results with the conventional approach of individually fitting each of the 153 SPARC galaxies. Throughout the NAV analysis, the stellar mass-to-light ratios are held constant at their central values. Conversely, for the individual fits, Gaussian priors are applied to $\Upsilon_{\rm d} \equiv \log_{10} Y_{\rm d}$ and $\Upsilon_{\rm b} \equiv \log_{10} Y_{\rm b}$, centered on $\log_{10} 0.5$ and $\log_{10} 0.6$ respectively, with a variance of 0.1^2 [22, 60]. While this flexibility in mass-to-light ratio variation significantly influences individual galaxies within the fits, the overall distribution of the sample should not be sensitive to these variations, a point we confirm in this analysis. The NAV method simplifies certain details relevant for individual galaxies but not for the sample results.

From the observational data for each galaxy, a χ^2 quantity is defined for a given model with parameters p_a as

$$\chi^2(p_a) = \sum_i \left(\frac{V(p_a, r_i) - V_i}{\sigma_i}\right)^2\,. \tag{4.12}$$

In the above, V_i is the observational circular velocity, with uncertainty σ_i, and at the radius r_i (as provided by SPARC). $V(p_a, r_i)$ is the model circular velocity at r_i.

Since the priors on Υ_b and Υ_d are Gaussian, it is possible to implement them by using an effective χ^2, which is defined as follows

$$\chi^2_\mathrm{eff}(p_a, \Upsilon_\mathrm{d}, \Upsilon_\mathrm{b}) \equiv \chi^2(p_a) + \left(\frac{\Upsilon_\mathrm{d} - \log_{10} 0.5}{0.1}\right)^2 + \left(\frac{\Upsilon_\mathrm{b} - \log_{10} 0.6}{0.1}\right)^2 . \tag{4.13}$$

For galaxies without a bulge, the last term should not be considered.

The determination of best-fit values involves the minimization of χ^2_eff. This minimization process corresponds to the Maximum *a posteriori* (MAP) estimation [e.g., 61], as detailed in the supplementary information section of [7].

Given that certain galaxies exhibit multiple local minima, we conducted numerous minimizations for each galaxy (a minimum of eight), utilizing distinct starting points and minimization meta-parameters. These minimizations were executed using the `MAGMA`[3] code [7], which employs the differential evolution optimization algorithm [62]. When seeking the best fit, characterized by a global minimum, global optimization techniques like the differential evolution method prove more efficient than MCMC-based procedures, given their specific suitability for this purpose.

4.3 The models and the results

4.3.1 Arctan$_\alpha$ model

4.3.1.1 Model definition

This is a toy model whose purpose is to clarify the method and the relation between other models results. This model is a generalization of a model studied by [63]. It is defined directly from the dark matter circular velocity, that is, it was not defined from a density profile. We generalize the original model by considering

$$V_{arctan}(r) = V_\mathrm{c} \left(\frac{2}{\pi}\right)^\alpha \arctan^\alpha\left(\frac{r}{r_\mathrm{t}}\right) , \tag{4.14}$$

where V_c, r_t and α are constants. The two first constants may change from galaxy to galaxy. The original case of [63] corresponds to $\alpha = 1$.

4.3.1.2 NAV analysis

Since V^2_{arctan} is the dark matter contribution to the circular velocity, then, from eq. (4.1), $\Delta V^2_{arctan}(r) = V^2_{arctan}(r)$. Hence, using eq. (4.7),

$$\delta V^2_{arctan}(r_\mathrm{n}) = \arctan^{2\alpha}\left(\frac{r_\mathrm{n}}{r_\mathrm{tn}}\right) \Big/ \arctan^{2\alpha}\left(r_\mathrm{tn}^{-1}\right) , \tag{4.15}$$

[3] github.com/davi-rodrigues/MAGMA.

with $r_{\rm tn} = r_{\rm t}/r_{\rm max}$. The space of parameters was reduced from three free parameters, in eq. (4.14), to two: $r_{\rm tn}$ and α.

For a given $r_{\rm n}$ value ($0 < r_{\rm n} < 1$), one can analytically compute the cases of very large or very small $r_{\rm tn}$ values,

$$\delta V^2_{arctan} = \begin{cases} 1 & \text{, for small } r_{\rm tn}. \\ {r_{\rm n}}^{2\alpha} & \text{, for large } r_{\rm tn}. \end{cases} \tag{4.16}$$

Upon examination of Fig. 4.3, it becomes evident that the upper limit is overly stringent, resulting in an inadequately covered region. Regardless of the chosen value for α, this issue persists. The lower boundary in the NAV plane is influenced by the α value. When considered alongside eq. (4.8), selecting an appropriate α can enhance alignment with the data. Opting for $\alpha = 1$ (or $\alpha = 1.1$) appears to be a favorable choice, as it associates large $r_{\rm tn}$ values with the lower limit in the NAV plane. Conversely, opting for $\alpha = 1/2$, leading to $\delta V^2_{\rm arctan} \sim r_{\rm n}$, encompasses considerably less observational data compared to the $\alpha = 1$ case. These boundary cases are depicted in Fig. 4.4.

After considering the analytical and numerical evaluations of the extreme cases, one can proceed to the third step as described in Sec. 4.2.3. We use the integral (4.9) in the interval $0.2 < r_{\rm n} < 0.9$ to find the best approximations for the observational 1σ and 2σ regions. The results are

$$\begin{aligned} 1\sigma &: \ 0.04 < r_{\rm tn} < 0.37\,, \\ 2\sigma &: \ 0 < r_{\rm tn} < \infty\,, \end{aligned} \tag{4.17}$$

for the case $\alpha = 1$, and

$$\begin{aligned} 1\sigma &: \ 0.07 < r_{\rm tn} < 1.25\,, \\ 2\sigma &: \ 0 < r_{\rm tn} < \infty\,, \end{aligned} \tag{4.18}$$

for the case $\alpha = 1/2$. The corresponding curves are also plotted in Fig. 4.4.

At last, we compute the NAV efficiency, as defined in Sec. 4.2.4, for $\alpha = 1/2$,

$$\begin{aligned} E_1 &= 0.71 \ \ [0.782 - 0.072]\,, \\ E_2 &= 0.49 \ \ [0.489 - 0.000]\,. \end{aligned} \tag{4.19}$$

The numbers in square brackets refer to the positive and negative contributions from eq. (4.10), they display an intermediate step in the computation.

For $\alpha = 1$,

$$\begin{aligned} E_1 &= 0.69 \ \ [0.764 - 0.070]\,, \\ E_2 &= 0.70 \ \ [0.709 - 0.005]\,. \end{aligned} \tag{4.20}$$

In comparison with $\alpha = 1$, the $\alpha = 1/2$ case lacks data diversity, leading to its efficiency being penalized. Consequently, the individual fits using this model will lead to larger χ^2 values, as it will be shown.

In summary, the mean efficiencies for $\alpha = 1/2$ and $\alpha = 1$ read respectively,

$$E_{\rm M}^{(1/2)} = 0.60\,, \ E_{\rm M}^{(1)} = 0.70 \tag{4.21}$$

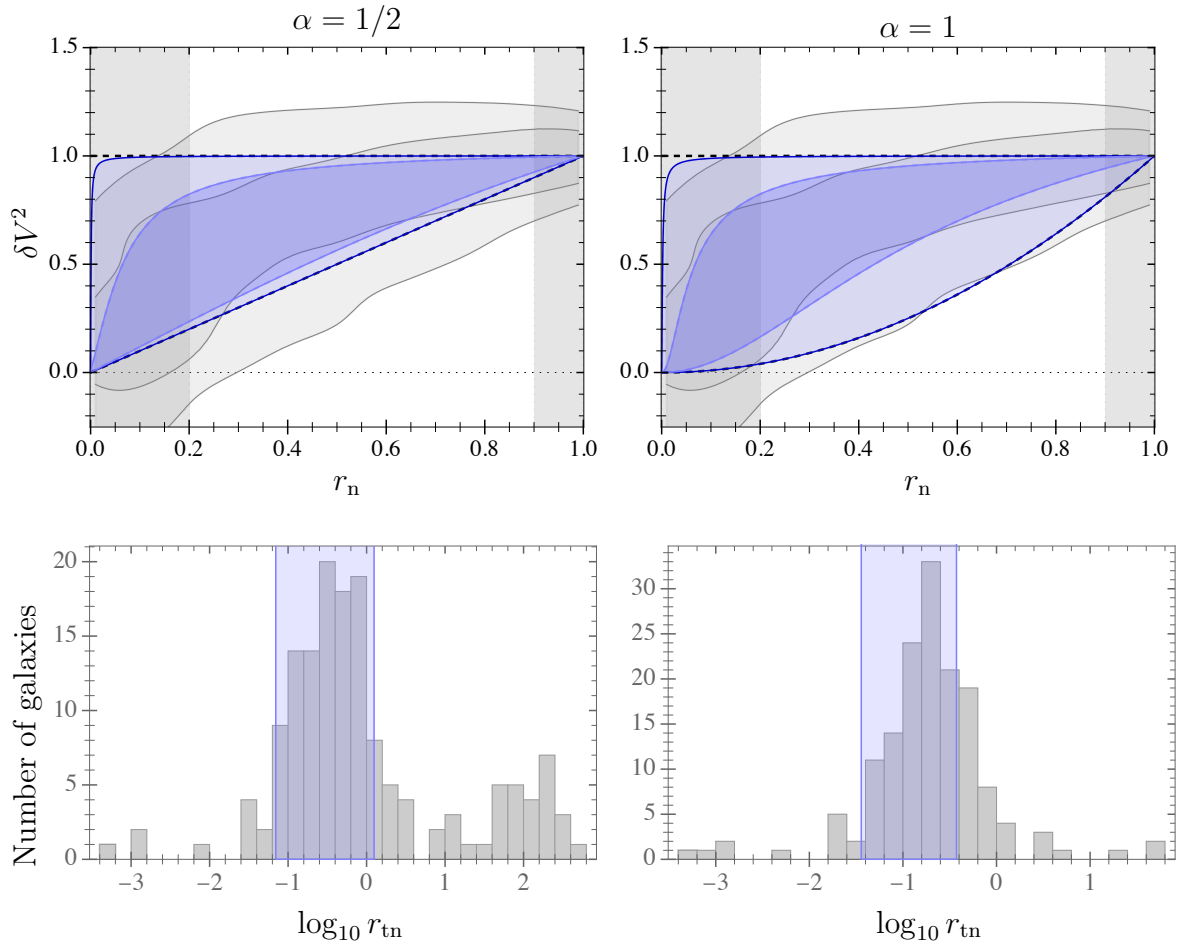

Figure 4.4: **Top:** The NAV plane for the Arctan model with $\alpha = 1/2$ (left) and $\alpha = 1$ (right). Refer also to Fig. 4.3. The two black dashed lines represent the extremum cases of the model, where r_{tn} tends to either infinity (lower limit in the plot) or 0 (upper limit in the plot), as defined by eq. (4.16). The bluish regions depict the best approximations of the arctan models for the observational 1σ and 2σ regions (4.17-4.18). The mean efficiency (4.11) for each case is respectively 0.70 and 0.60. **Bottom:** Histograms illustrating the distribution of r_{tn} from individual fits for the 153 SPARC galaxies. The case with $\alpha = 1/2$ exhibits a strong tendency to produce very large r_{tn} values, many of which are dynamically equivalent to the $r_{tn} \to \infty$ case. The transparent blue rectangle represents the 1σ region of the corresponding α case, as inferred from eqs. (4.17-4.18). There are no data beyond the plotted regions in these histograms. Image taken from [54].

4.3.1.3 Comparison with the individual fits results

The individual fits consider the parameters V_c, r_t, Y_d, and, if a bulge is present, Y_b as free variables. Specifically, r_t and V_c undergo flat priors, confined to the ranges $0.05 < r_t\,(\text{kpc}) < 500$ and $10 < V_c\,(\text{km/s}) < 1000$ to ensure reasonable values and enhance computational efficiency. Y_d and Y_b have Gaussian priors, as discussed in the preceding section.

Figure 4.4 also exhibits the distribution of $r_{\rm tn}$ values derived from individual fits. As anticipated from the prior section, the $\alpha = 1/2$ scenario results in several galaxies producing large $r_{\rm tn}$ values, effectively approaching $r_{\rm tn} \to \infty$. Additionally, the earlier analysis allows us to deduce a range of $r_{\rm tn}$ that is most prevalent across individual fits.

Given that the mean NAV efficiency ($E_{\rm M}$) is higher for the $\alpha = 1$ case, one can anticipate generally lower χ^2 values. Indeed, a comparison of the median χ^2 values for each case reveals

$$\widetilde{\chi^2_{\rm arctan_{1/2}}} \approx 18 \quad \text{and} \quad \widetilde{\chi^2_{\rm arctan_1}} \approx 9. \tag{4.22}$$

A tilde is used to denote the median. Although the mean χ^2 also favors the $\alpha = 1$ case, it provides a less robust description of the sample, as it is susceptible to substantial fluctuations induced by the data from a single galaxy. In Sec. 4.4, we collate and compare the results of all the models.

4.3.2 NFW

4.3.2.1 Model definition

The Navarro-Frenk-White (NFW) dark matter profile, formulated through N-body simulations for a dark matter-only universe [8, 64], has enjoyed considerable success across various astrophysical applications and is often regarded as the standard dark matter halo. Nevertheless, given its absence of baryonic influence, it is unsurprising that systematic deviations can arise in certain systems, such as galaxies [e.g., 53, 65, 66, 67, 68, 69, 70]. Baryonic physics is expected to introduce a level of diversity to dark matter halos beyond what is observed in pure dark matter simulations. This diversity extends to the cusp/core controversy and beyond [67].

The NFW profile is a two-parameter cuspy dark matter halo whose density profile is given by

$$\rho_{\rm NFW}(r) = \frac{\rho_{\rm s}}{r/r_{\rm s}(1 + r/r_{\rm s})^2}\,. \tag{4.23}$$

In the above, r is the spherical radial coordinate, while $r_{\rm s}$ and $\rho_{\rm s}$ are constants that can change from galaxy to galaxy.

The internal mass of this profile is given by

$$M_{\rm NFW}(r) = 4\pi r^3 \rho_s \left[\ln\left(\frac{r + r_{\rm s}}{r_{\rm s}}\right) - \frac{r}{r + r_{\rm s}}\right]. \tag{4.24}$$

4.3.2.2 NAV analysis

The additional velocity is the dark matter contribution, hence

$$\Delta V^2_{\rm NFW}(r) = G\frac{M_{\rm NFW}(r)}{r}\,. \tag{4.25}$$

Using the $M_{\rm NFW}$ expression,

$$\begin{aligned}\delta V^2_{\rm NFW}(r_n) &= \frac{\Delta V^2_{\rm NFW}(r_n\, r_{\rm max})}{\Delta V^2_{\rm NFW}(r_{\rm max})} \\ &= \frac{1}{r_{\rm n}}\frac{\frac{1}{1+r_{\rm sn}/r_{\rm n}} - \ln(1 + r_{\rm n}/r_{\rm sn})}{\frac{1}{1+r_{\rm sn}} - \ln(1 + 1/r_{\rm sn})}\,.\end{aligned} \tag{4.26}$$

For a given $0 < r_{\rm n} < 1$, one can compute the asymptotic limits,

$$\delta V^2_{\rm NFW} = \begin{cases} {r_{\rm n}}^{-1} & \text{, for small } r_{\rm sn}. \\ \\ r_{\rm n} & \text{, for large } r_{\rm sn}. \end{cases} \tag{4.27}$$

The above result for small $r_{\rm sn}$ does not contain the tight bound that the Arctan model has for small $r_{\rm tn}$ and for any α. On the other hand, the lower bound in the NAV plane, given by $r_{\rm n}$, is too stringent, and it is the same of the Arctan model with $\alpha = 1/2$.

We proceed now to fit the 1σ and 2σ regions using the integral (4.9) in the interval $0.2 < r_{\rm n} < 0.9$. The results are

$$\begin{aligned} 1\sigma &: \ 0.33 < r_{\rm sn} < 4.9\,, \\ 2\sigma &: \ 0.15 < r_{\rm sn} < \infty\,. \end{aligned} \tag{4.28}$$

These regions are plotted in Fig. 4.5.

The NAV efficiency for the NFW model is computed as

$$\begin{aligned} E_1 &= 0.77 \ \ [0.843 - 0.072]\,, \\ E_2 &= 0.63 \ \ [0.648 - 0.015]\,. \end{aligned} \tag{4.29}$$

Hence, the mean efficiency reads,

$$E_{\rm M} = 0.70\,. \tag{4.30}$$

The NFW model has the same mean efficiency of the arctan model with $\alpha = 1$, and it is better than the $\alpha = 1/2$ case due to the upper part of the NAV plane.

4.3.2.3 Comparison with the individual fits results

The individual NFW fits follow the procedures outlined in Sec. 4.3.1.3, with slight adjustments to the NFW parameter constraints: $\rho_{\rm s} > 10\,{\rm M}_\odot/{\rm k}pc^3$ and $0.05 < r_{\rm s}({\rm k}pc) < 10^4$.

In Figure 4.5, the distribution of $r_{\rm sn}$ values from individual fits is presented. Consistent with expectations, some galaxies yield very large values for $r_{\rm sn}$. Due to the logarithmic asymptotic behavior, the NFW model necessitates larger $r_{\rm sn}$ compared to the arctan model with $\alpha = 1/2$. As anticipated, the NAV analysis aids in estimating a general range of $r_{\rm sn}$ values prevalent in individual fits.

The median χ^2 value for the NFW model is approximately $\widetilde{\chi^2_{\rm NFW}} \approx 15$. This performance falls between the median χ^2 values of the arctan model with $\alpha = 1/2$ and the $\alpha = 1$ case. Further model comparisons will be explored in Sec. 4.4.

4.3.3 Burkert profile

4.3.3.1 Model definition

The Burkert profile [35] is a two-parameter cored dark matter halo that has been extensively studied and which has achieved phenomenological success [e.g., 71, 72, 73, 74]. Its density profile is given by

$$\rho_{\rm Bur}(r) = \frac{\rho_{\rm c}}{(1 + r/r_{\rm c})(1 + r^2/r_{\rm c}^2)}\,. \tag{4.31}$$

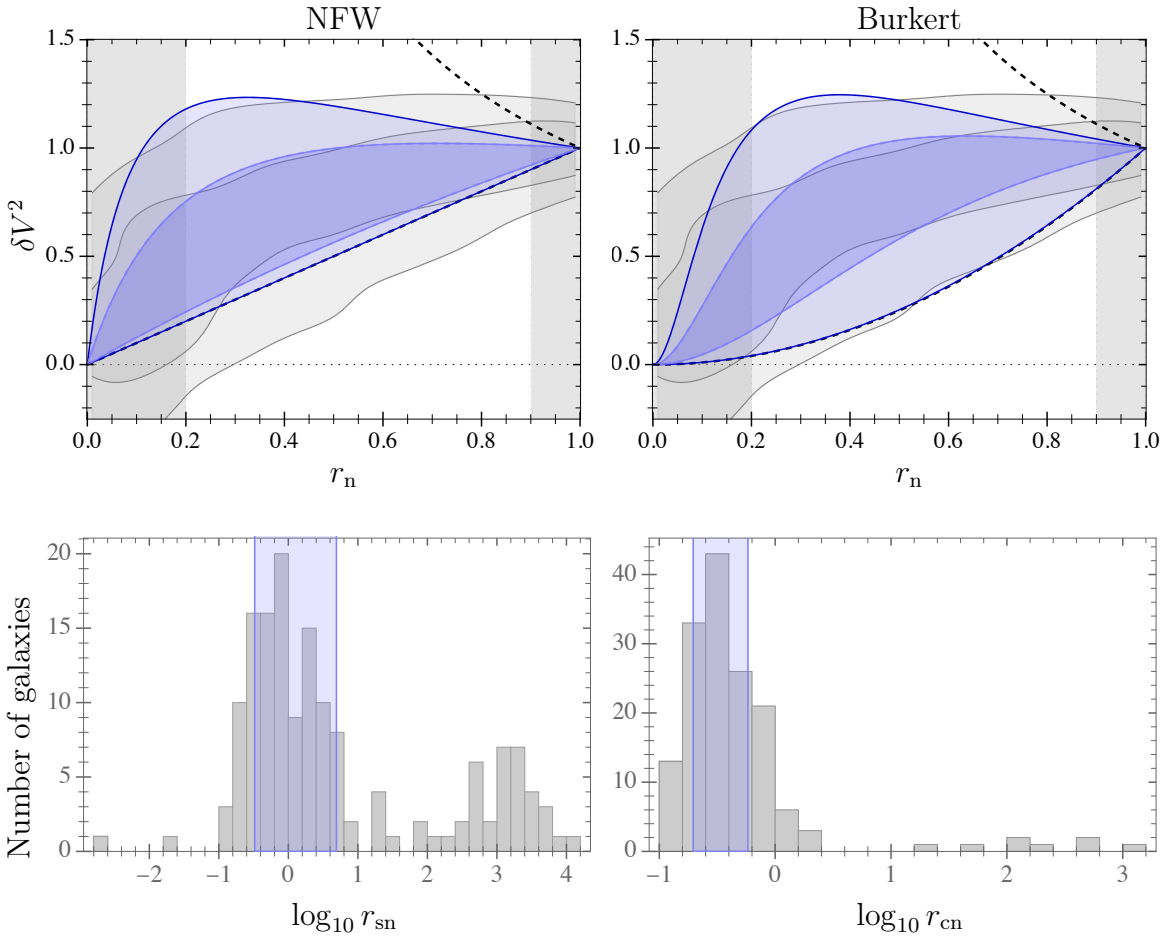

Figure 4.5: **Top:** The NAV plane for the NFW (left) and Burkert (right) models. Refer also to Figs. 4.3, 4.4. The two black dashed lines illustrate the extremum cases of the models, as defined by eq. (4.27) and eq. (4.37) respectively. The bluish regions depict the best approximations of the NFW or Burkert models for the observational 1σ and 2σ regions (4.28), (4.38). The mean efficiency values are 0.70 and 0.80 respectively, calculated using eqs. (4.30, 4.39). **Bottom:** Histograms showing the distribution of r_{sn} and r_{cn} from individual NFW and Burkert fits. The transparent blue rectangle represents the 1σ region as inferred from eq. (4.28) or eq. (4.38). Several galaxies exhibit a preference for very large r_{sn} values (with $r_s > 10r_{max}$). For Burkert, only a few galaxies favor $r_c > 10r_{max}$. Both histograms display the complete data, with no galaxy data beyond the plotted regions. Image taken from [54].

In the above, r is the spherical radial coordinate, while r_c and ρ_c are constants that can change from galaxy to galaxy.

The internal mass of the Burkert profile reads,

$$\begin{aligned} M_{\rm Bur}(r) &= 4\pi \int_0^r \rho_{\rm Bur}(r) r^2 \, dr \\ &= 2\pi \, \rho_c r_c^3 \, \xi \left(\frac{r}{r_c} \right) , \end{aligned} \tag{4.32}$$

where

$$\xi(x) \equiv \ln\left((1+x)\sqrt{1+x^2}\right) - \tan^{-1}(x)\,. \tag{4.33}$$

4.3.3.2 NAV analysis

It is convenient to introduce the normalized core radius as

$$r_{\rm cn} \equiv \frac{r_{\rm c}}{r_{\rm max}}\,. \tag{4.34}$$

Using that, for a spherical mass distribution, $V^2(r) = GM(r)/r$, we can now compute $\Delta V^2_{\rm mod}$ and $\delta V^2_{\rm mod}$ as

$$\Delta V^2_{\rm Bur}(r_{\rm n}) = 2\pi \frac{G\rho_{\rm c} r_{\rm c}^3}{r_{\rm max}} \frac{1}{r_{\rm n}} \xi\left(\frac{r_{\rm n}}{r_{\rm cn}}\right), \tag{4.35}$$

$$\delta V^2_{\rm Bur}(r_{\rm n}) = \frac{1}{r_{\rm n}} \frac{\xi(r_{\rm n}/r_{\rm cn})}{\xi(1/r_{\rm cn})}. \tag{4.36}$$

For given $0 < r_{\rm n} < 1$, one can compute the asymptotic limits,

$$\delta V^2_{\rm Bur} = \begin{cases} {r_{\rm n}}^{-1} & \text{, for small } r_{\rm cn}. \\ {r_{\rm n}}^{2} & \text{, for large } r_{\rm cn}. \end{cases} \tag{4.37}$$

This model has the same asymptotic for small $r_{\rm cn}$ as the NFW model, but for large $r_{\rm cn}$ it behaves like the arctan model with $\alpha = 1$. Hence, it is expect that its NAV efficiency is larger than the previous models, and this will be the case.

We fit the 1σ and 2σ regions using the integral (4.9) in the interval $0.2 < r_{\rm n} < 0.9$. The results are

$$\begin{aligned} 1\sigma:&\ 0.20 < r_{\rm cn} < 0.58\,, \\ 2\sigma:&\ 0.12 < r_{\rm cn} < 35\,. \end{aligned} \tag{4.38}$$

These regions are plotted in Fig. 4.5.

The efficiency for the Burkert model reads

$$E_1 = 0.74 \ \text{ and } \ E_2 = 0.86\,, \text{ hence } E_{\rm M} = 0.80\,. \tag{4.39}$$

This is the highest $E_{\rm M}$ value for the models considered up to this point, and very close to the $E_{\rm M}$ value of the polynomial description in Fig. 4.3.

4.3.3.3 Comparison with the individual fits results

The individual Burkert fits follow the procedures outlined in Sec. 4.3.1.3, with adjustments to the Burkert parameter constraints: $\rho_{\rm c} > 10\,{\rm M}_\odot/{\rm k}pc^3$ and $0.01 < r_{\rm c}({\rm k}pc) < 10^3$.

In Figure 4.5, the distribution of $r_{\rm cn}$ values from individual fits is displayed. As anticipated, the NAV analysis aids in estimating a general range of $r_{\rm cn}$ values common within individual fits (regardless of whether the stellar mass-to-light ratios are being fitted or are fixed at their central

values).

The median of the minimum χ^2 value for the Burkert halo is approximately $\widetilde{\chi^2_{\rm Bur}} \approx 8$. This stands as the lowest median χ^2 among the models considered thus far. As expected from the NAV analysis, this χ^2 result significantly outperforms that of the NFW halo or the $\text{Arctan}_{1/2}$ model.

4.3.4 Modified Newtonian Dynamics (MOND)

4.3.4.1 Model definition

MOND, a well-known and straightforward modified gravity model, has demonstrated certain success in explaining galaxy rotation curves [59, 75]. Following the original MOND formulation and its recent motivation from the Radial Acceleration Relation (RAR) [56], this model posits that the observational acceleration can be expressed as a function of the Newtonian acceleration:

$$\mathbf{a}_{\rm N} = \mu\left(\frac{a}{a_0}\right)\mathbf{a}\,, \tag{4.40}$$

where a_0 is a constant, μ is termed the interpolation function, $\mathbf{a}_{\rm N}$ is the Newtonian acceleration inferred from baryonic matter, and $\mathbf{a}$ is the observational one. Within axis-symmetric disk galaxies, both acceleration vectors $\mathbf{a}$ and $\mathbf{a}_{\rm N}$ align along the radial direction in the plane of the disk ($z = 0$), thus $\mathbf{a} = -\frac{V^2}{r}\hat{\boldsymbol{r}}$ and $a = |\mathbf{a}| = \frac{V^2}{r}$.

The interpolation function μ must satisfy $\mu(x) = 1$ for $x \gg 1$ and $\mu(x) = x$ for $x \ll 1$. For $x \sim 1$, the behavior of the interpolation function should be determined from observational data. The RAR suggests a relation between $\mathbf{a}$ and $\mathbf{a}_{\rm N}$ [56]:

$$\mathbf{a} = \frac{\mathbf{a}_{\rm N}}{1 - e^{-\sqrt{a_{\rm N}/a_0}}}\,. \tag{4.41}$$

The same data lead to $a_0 = 1.2 \times 10^{-10}$ m/s^2 as the best fit for a_0 (considering all the galaxies together). Another possible value for a_0, from the same galaxies and the same function (4.41), was derived by [7, 37], where the best value for a_0 minimizes tensions between individual galaxies, considering observational uncertainties, leading to a lower value, $a_0 = 9.6 \times 10^{-11}$ m/s^2, still consistent with $a_0 \sim 10^{-10}$ m/s^2.

MOND is considered here for its simplicity and interesting results in the NAV analysis. Some studies have indicated that assuming a common a_0 value for all galaxies is inconsistent with observational uncertainties [7, 37], with significance exceeding 5σ. This issue has been extensively discussed in the literature [76, 77, 78, 79, 80, 81, 82], along with additional works [83, 84, 85, 86, 87]. This poses a challenge for MOND (the original version based on (4.40)) as a comprehensive theory for galaxies [69, 84, 88].

The NAV analysis, as presented here, is not concerned with the foundational aspects of MOND but emphasizes a notable pattern in the rotation curves for MOND: a lack of diversity [85, 89], consistent with similar conclusions drawn from different methods.

4.3.4.2 NAV analysis

From eq. (4.41) with $a_{\rm N} = a_{\rm bar} = V^2_{\rm bar}/r$, the $\Delta V^2_{\rm mod}$ MOND expression reads

$$\Delta V^2_{\rm MOND} = V^2_{\rm MOND} - V^2_{\rm bar} = \frac{V^2_{\rm bar}}{e^{\sqrt{a_{\rm bar}/a_0}} - 1}\,, \tag{4.42}$$

hence

$$\delta V^2_{\rm MOND}(r_{\rm n}) = \frac{V^2_{\rm bar}(r_{\rm n})}{V^2_{\rm bar}(1)} \frac{e^{\sqrt{a_{\rm bar}(1)/a_0}} - 1}{e^{\sqrt{a_{\rm bar}(rn)/a_0}} - 1}\,. \tag{4.43}$$

Since MOND is nonlinear on the constant a_0, this constant is still present in $\delta V^2_{\rm mod}$.

The Newtonian limit of MOND is found in the limit $a_0 \to 0$. Assuming that $V^2_{\rm bar}(r_{\rm n}) > 0$, then, for a given $r_{\rm n} \in (0, 1)$,

$$\lim_{a_0 \to 0} \delta V^2_{\rm MOND}(r_{\rm n}) = \begin{cases} 0\,, & \text{if } a_{\rm bar}(1) < a_{\rm bar}(r_{\rm n}) \\ \infty\,, & \text{if } a_{\rm bar}(1) > a_{\rm bar}(r_{\rm n}) \end{cases}\,. \tag{4.44}$$

Therefore, in the Newtonian limit of MOND, $\delta V^2_{\rm MOND}$ becomes either zero for all or most $r_{\rm n}$ values. It is worth noting that, in general, $V^2_{\rm mod}$ is not well defined for Newtonian gravity without dark matter, and the limit of a modified gravity theory toward Newtonian gravity can exhibit different features depending on the specific theory under consideration.

On the contrary, when $a_0 \to \infty$, assuming $V^2_{\rm bar} > 0$, the limit yields:

$$\lim_{a_0 \to \infty} \delta V^2_{\rm MOND}(r_{\rm n}) = \sqrt{r_{\rm n}} \frac{V_{\rm bar}(r_{\rm n})}{V_{\rm bar}(1)}\,. \tag{4.45}$$

This regime, often termed the "deep MOND regime," is characterized by large a_0 or small $a_{\rm N}$. For large radii, where most galaxies are expected to reside in this regime and $V_{\rm bar}(1) \sim V_{\rm bar}(1)$, $\delta V^2_{\rm MOND}(r_{\rm n}) \sim \sqrt{r_{\rm n}}$. Notably, this behavior closely aligns with the best-fit curve derived from the polynomial approach (4.8). Consequently, MOND appears effective in covering the central region of the NAV plane. However, there is no independent mechanism to adjust the data distribution, especially in the 2σ region. As will be numerically verified, MOND exhibits a lack of diversity.

Unlike the previous dark matter cases, the $\delta V^2_{\rm MOND}(r_{\rm n})$ curves directly rely on $V^2_{\rm bar}(r_{\rm n})$. To consider the 1σ and 2σ HDRs for MOND, we utilize (4.43) to draw the $\delta V^2_{\rm MOND}(r_{\rm n})$ curves for each of the 153 $V^2_{\rm bar}(r_{\rm n})$ curves provided by SPARC. These curves are depicted in Fig. 4.6. Subsequently, these curves are randomly discretized to smooth out the data point distribution, and the 1σ and 2σ HDRs are computed. These regions are also illustrated in the central plot of Fig. 4.6. Additionally, we showcase the consequences of considering either very large or very small a_0 values.

The NAV efficiency for the MOND model reads

$$E_1 = 0.515\,,\ E_2 = 0.544\,,\ \text{and}\ E_{\rm M} = 0.53\,. \tag{4.46}$$

This is the lowest efficiency value here computed. Considering Fig. 4.6, it is not a surprising result, since the MONDian curves are almost entirely inside the region delimited by the arctan model with $\alpha = 1/2$. The 1σ and 2σ regions from MOND are narrower than the observational

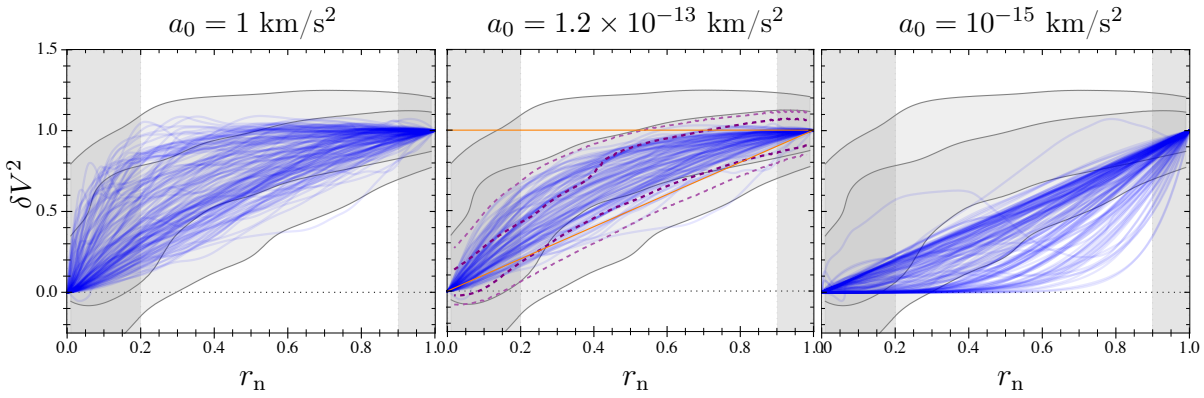

Figure 4.6: The NAV for MOND, as described by eq. (4.41), is presented for three different a_0 values. Each transparent blue curve corresponds to one of the 153 SPARC galaxies, the same dataset used for the RAR [56]. The central plot assumes the commonly used a_0 value (1.2×10^{-13} km/s^2), while the other two plots consider extreme cases (1 km/s^2 and 10^{-15} km/s^2). The central plot outlines the limits of the 1σ and 2σ highest density regions (HDRs), represented by dashed purple curves. Additionally, for reference, orange straight lines $\delta V^2 = r_n$ and $\delta V^2 = 1$ are included, marking the limits of the arctan model for $\alpha = 1/2$. The mean MOND efficiency for the central plot is 0.53, as defined in (4.46). Image taken from [54].

ones.

As the first plot of Fig. 4.6 shows, considering the NAV plane covering alone, a large value for a_0 is favored. Such large a_0 value in on the other hand incompatible with the $\Delta V^2_{\rm obs}$ data, Fig. 4.1.

4.3.4.3 Comparison with the individual fits results

In the case of MOND, following the methodology applied in previous sections, individual fits were performed for each galaxy. The only parameters subject to fitting in this scenario were the stellar mass-to-light ratios for both the disk and bulge. We adopted the standard a_0 value, specifically $a_0 = 1.2 \times 10^{-13}$ km/s^2. Given the low efficiency value $E_{\rm M}$ (4.46) associated with this model, it is anticipated that MOND will exhibit a relatively high median χ^2 value, confirming $\widetilde{\chi^2_{\rm MOND}} \approx 48$.

Among the considered models, this yields the largest $\widetilde{\chi^2}$ value, aligning with its minimal $E_{\rm M}$ value. Notably, it is essential to acknowledge that this model features the fewest free parameters, solely depending on the global a_0 value. Our analysis does not incorporate a metric for parameter compensation, as it is not the primary focus.

It is noteworthy that MOND introduces no additional parameters beyond those considered in the NAV analysis, distinguishing it from the other models. In these individual fits for MOND, variations in distance compatible with the uncertainties reported by SPARC were also explored. Within this context, the median value is reduced to $\widetilde{\chi^2_{\rm MOND}} \approx 30$.

4.3.5 DC14

4.3.5.1 Model definition

The [53] model (DC14) extends the NFW halo by considering baryonic feedback. The DC14 halo profile depends on the stellar mass of the galaxy (M_*), more specifically, on the quantity $X = \log_{10} M_*/M_{\rm halo}$, where $M_{\rm halo}$ is the dark matter halo mass.

$$
\begin{aligned}
\rho_{\rm DC14}(r) &= \frac{\rho_{\rm s}}{\frac{r^\gamma}{r_s^\gamma}\left(1+\frac{r^\alpha}{r_{\rm s}^\alpha}\right)^{(\beta-\gamma)/\alpha}}\,, \\
\alpha &= 2.94 - \log_{10}\left(\left(10^{X+2.33}\right)^{2.29} + \frac{1}{\left(10^{X+2.33}\right)^{1.08}}\right)\,, \\
\beta &= 0.26X^2 + 1.34X + 4.23\,, \\
\gamma &= \log_{10}\left(10^{X+2.56} + \frac{1}{\left(10^{X+2.56}\right)^{0.68}}\right) - 0.06\,.
\end{aligned}
\tag{4.47}
$$

The parameters above were derived for $-4.1 < X < -1.3$. The case $X = -4.1$ leads to the NFW halo (within a good approximation).

Each $\delta V^2_{\rm DC14}$ curve, as defined earlier, is contingent on X and $r_{\rm s}$. The estimation of X for each galaxy is derived from the stellar-to-halo mass relation [90]. While we do not present individual fits for this model here, previous studies, such as those conducted by [52, 74], have undertaken such analyses using SPARC data. Notably, these investigations revealed, among other enhancements, a marked improvement in the overall fit quality compared to the NFW profile. Moreover, the quality of fits was found to be quite comparable to the results obtained with the Burkert profile, as indicated by their cumulative distribution function (CDF) plots. In this section, our exploration delves into the specific enhancements that DC14 brings to the NAV plane and the degree to which it aligns with the Burkert profile.

4.3.5.2 NAV analysis

From the expression given in eq. (4.47), one can derive $\delta V^2_{\rm DC14}(r_{\rm n}, r_{\rm s}, X)$. As discussed in Sec. 4.3.2, two notable challenges associated with the NFW halo are: *i*) the elevated lower limit in the NAV plane dictated by the curve $\delta V^2_{\rm NFW} = r_{\rm n}$, which is excessively high, and *ii*) the necessity to employ exceedingly large $r_{\rm s}$ values (resulting in very low concentration values c when compared to simulation outcomes) to achieve this lower limit.

Through the NAV analysis, it can be directly demonstrated that these two issues are not inherent to the DC14 halo. In Fig. 4.7, we present $\delta V^2_{\rm DC14}$ curves for two $r_{\rm sn}$ values ($r_{\rm sn} = 0.1$ and $r_{\rm sn} = 1$) across different potential X values. For the NFW halo, the curve corresponding to $r_{\rm sn} = 0.1$ is the darkest one in the lower part of Fig. 4.7, indicating a considerable distance from the 2σ limit and still within the 1σ region. In contrast, for the DC14 model, adjusting the value of X allows one to approach the 2σ limit more closely than any NFW curve can achieve, even in the limit of $r_{\rm sn} \to \infty$. While this observation does not necessarily establish the efficacy of DC14 for individual galaxies, it does demonstrate that DC14 can circumvent the challenges inherent in the NFW halo for any given galaxy.

It is also possible to fit $\delta V^2_{\rm DC14}$ to the 1σ and 2σ HDRs, as follows:

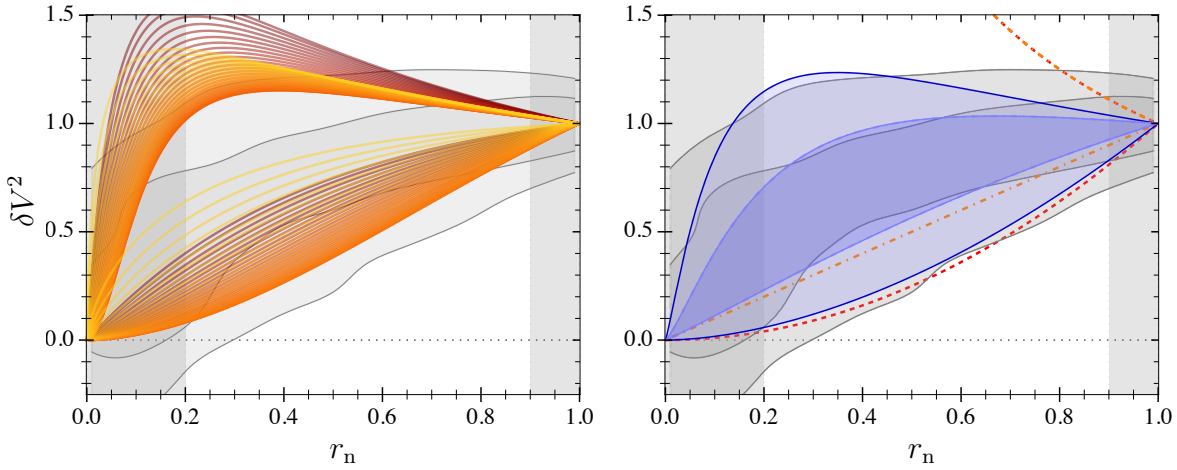

Figure 4.7: **Left.** The curves $\delta V^2_{\rm DC14}$ are depicted for two values of $r_{\rm sn}$: 0.1 and 1, and for various values of X, each represented by different colors. The upper part of the plot, utilizing $r_{\rm sn} = 0.1$, displays curves ranging from dark red to light yellow, corresponding to X values changing from -4.1 to -1.3. The lower part, using $r_{\rm sn} = 1$, similarly varies X across the same range of colors. **Right.** The NAV plane for the DC14 model is presented. The orange dot-dashed curve represents the extrema cases for NFW profile (4.27), while the red dashed curve signifies the extrema for the Burkert profile (4.37). The two bluish regions denote the best approximation for the DC14 model for the observational 1σ and 2σ regions (4.48). The mean efficiency is 0.80, defined in (4.49). Image taken from [54].

$$\begin{aligned} 2\sigma_+ &: r_{\rm sn} = 0.14\,,\ X = -3.88\,,\\ 1\sigma_+ &: r_{\rm sn} = 0.24\,,\ X = -3.76\,,\\ 1\sigma_- &: r_{\rm sn} = 1.91\,,\ X = -1.60\,,\\ 2\sigma_- &: r_{\rm sn} = \infty\,,\ X = -2.66\,. \end{aligned} \tag{4.48}$$

The corresponding curves have been depicted in Fig. 4.7.

When considering fixed values of $r_{\rm sn}$ and $r_{\rm n}$, the curves $\delta V^2_{\rm DC14}(X)$ exhibit non-monotonic behavior, making it impractical to directly infer parameter regions from the fits mentioned earlier. Figure 4.8 delineates the parameter space regions falling above $2\sigma_+$, between $2\sigma_+$ and $1\sigma_+$, within the 1σ region, between $1\sigma_-$ and the lowest conceivable $\delta V_{\rm NFW}$ curve, as well as the curves capable of descending below the $\delta V_{\rm NFW}$ ones. This classification was carried out by assessing the curves at the fixed radius $r_{\rm n} = 0.5$.

As illustrated in Figure 4.8, any stellar mass (within the range considered by [53]) can effectively cover either the 1σ region or the region above it. For the region below the 1σ threshold, reasonable $r_{\rm s}$ values are achievable when X lies in the range $-2.0 \lesssim X \lesssim -3.5$. This analysis also indicates that it is feasible to surpass the limitations imposed by NFW in the NAV plane while maintaining reasonable $r_{\rm s}$ values. It is important to note that NFW corresponds approximately to the case $X = -4.1$.

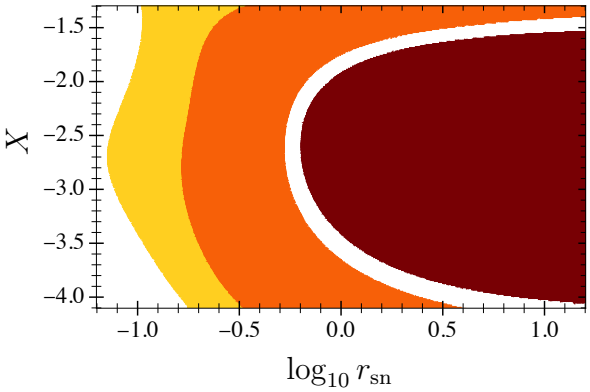

Figure 4.8: Five distinct regions within the DC14 parameter space are depicted: the leftmost white region signifies the parameter space where the curves $\delta V^2_{\mathrm{DC14}}$ surpass the $2\sigma_+$ curve (4.48). In the yellow region, the $\delta V^2_{\mathrm{DC14}}$ curves are positioned above the $1\sigma_+$ but below the $2\sigma_+$ curve. Moving to the orange region, it corresponds to the $\delta V^2_{\mathrm{DC14}}$ curves within the 1σ region. The thin white region indicates where $\delta V^2_{\mathrm{DC14}}$ falls between $1\sigma_-$ and the asymptotic lowest limit of $\delta V^2_{\mathrm{NFW}}$. Finally, the rightmost dark red region corresponds to the $\delta V^2_{\mathrm{DC14}}$ curves situated below the lowest conceivable $\delta V^2_{\mathrm{NFW}}$ curves. All comparisons are conducted at $r_{\mathrm{n}} = 0.5$. Image taken from [54].

Using the curves from eq. (4.48) one can compute the NAV efficiency of the DC14 model as

$$E_1 = 0.776\,,\ E_2 = 0.824\,,\ \text{hence}\ \ E_{\mathrm{M}} = 0.80\,. \tag{4.49}$$

This is the same E_{M} that was found for Burkert.

While we do not perform the individual DC14 fits in this context, an estimation based on the $\delta V^2_{\mathrm{DC14}}$ curves and the aforementioned efficiency values suggests that the median χ^2 values should be approximately comparable to those of the Burkert model and the arctan model with $\alpha = 1$. In support of this, [74] demonstrate that, on average, the DC14 fits are significantly superior to those of NFW and closely align with the quality of Burkert profile fits.

4.4 Model comparisons

In this section, we provide a summary and comparison of the results obtained from the various models.

Table 4.1 presents the mean efficiency (E_{M}) results for each model, along with the corresponding medians of χ^2 and χ^2_{eff}. The medians are denoted by a tilde, and the definitions of these quantities can be found in Sec. 4.2.5. A noticeable correlation exists between E_{M} and the median values of χ^2 and χ^2_{eff}.

Among the models featuring individual galaxy fits, it is unsurprising to observe that the Burkert profile excels in both E_{M} and χ^2 in Table 4.1. This model is known for its capability to deliver excellent fits to a substantial number of galaxies, often outperforming the NFW profile

Table 4.1: Model mean NAV efficiency ($E_{\rm M}$), median χ^2 and $\chi^2_{\rm eff}$ results. The models are sorted from larger to smaller $E_{\rm M}$. Larger $E_{\rm M}$ values indicate better agreement between theory and observation in the NAV plane (Sec. 4.2.4).

Model	$E_{\rm M}$	$\widetilde{\chi^2}$	$\widetilde{\chi^2_{\rm eff}}$
Polynomial	0.86	—	—
DC14	0.80	—	—
Burkert	0.80	8.0	8.1
Arctan_1	0.70	8.5	8.9
NFW	0.70	14.9	16.0
$\text{Arctan}_{1/2}$	0.60	17.7	19.0
$\text{MOND}_{\text{dist.}}$	0.53	29.6	37.1
MOND	0.53	47.6	59.6

and modified gravity approaches [e.g., 74, 91, 92].

As explained in Sec. 4.2.5, it is important to note that the NAV analysis considers $Y_{\rm d}$ and $Y_{\rm b}$ as fixed, but the sample results are applicable even when these parameters have Gaussian priors. This is reasonable since there is no expected correlation between variations in the stellar mass-to-light ratios and regions in the NAV plane. Additionally, we directly verified that for all the models tested here, the distribution of $\Upsilon_{\rm d} = \log_{10} Y_{\rm d}$ from the fits is compatible with Gaussian, centered around $\sim \log_{10} 0.5$.

For MOND, being a model particularly sensitive to small changes in the baryonic content and lacking an independent parameter controlling the magnitude of non-Newtonian effects, we considered variations in galaxy distances aligned with observational errors. When these changes are incorporated, we denote the model as $\text{MOND}_{\text{dist.}}$. Although this additional freedom reduces the median χ^2 by several units, the final $\widetilde{\chi^2}$ result still exceeds that of the $\text{Arctan}_{\alpha=1/2}$ model. More details on the distance modeling can be found in the supplementary material of [7] or [37, 93]. While one could consider changes in galaxy inclination as well, the median χ^2 for this dataset would only slightly decrease, with no substantial impact on the sample results. Changes in Υ_* and distance play a more significant role in this sample [56, 78]. Whether including or excluding distance variations, a correlation between efficiency and χ^2 is consistently observed.

Table 4.1 indicates a trend where a larger $E_{\rm M}$ corresponds to a lower median χ^2. In Figure 4.9, the cumulative distribution function (CDF) plots for χ^2 are presented, encompassing all the models fitted with individual galaxies. The horizontal line corresponding to $\widetilde{\chi^2}$ in Table 4.1 aligns with a CDF value of 0.5. This illustrates that the ordering of $\widetilde{\chi^2}$ in Table 4.1 is not an artifact tied to the use of the median; a similar order could be discerned at nearly any CDF value (or, equivalently, at any chosen percentile, not restricted to the median). The CDF plots for $\chi^2_{\rm eff}$ exhibit a qualitatively comparable pattern.

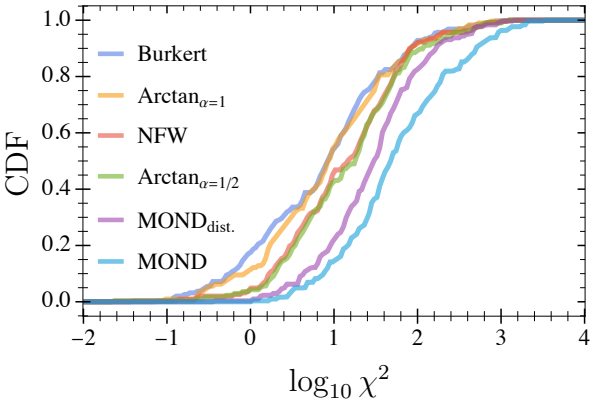

Figure 4.9: The cumulative distribution functions (CDFs) illustrate the distribution of χ^2 values derived from the individual fits of various models. The medians of χ^2, as presented in Table 4.1, can be identified at the intersection points between the curves and the CDF value of 0.5. This plot provides a comprehensive overview of the previous table results, offering insights into the distribution across different percentiles, not just the median. Image taken from [54].

4.5 Example of NAV use

Palatini f(R) gravity stands out as one of the simplest extensions of general relativity (GR) and serves as a straightforward realization of a metric-affine theory, maintaining an equivalent number of degrees of freedom as GR. In a vacuum, this theory seamlessly translates into GR with a cosmological constant. However, the mapping between GR and Palatini f(R) within a matter-filled environment necessitates a reinterpretation of the matter fields, the implications of which depend on the specific physical context.

The focus of this section is to show a further application of the NAV method to briefly investigate the potential of f(R) Palatini as a dark matter candidate. Examining a broad class of f(R) theories that allow a polynomial approximation in the weak field limit, the analysis, utilizing SPARC data and the NAV method, indicates that such theories cannot effectively replace dark matter in galaxies. Additionally, this conclusion extends to Eddington-inspired Born-Infeld gravity. Unlike the metric f(R) case, the rotation curve data alone are adequate for drawing this conclusion. Importantly, this result does not preclude the possibility of a combined scenario involving modified gravity and dark matter.

The action for (torsionless) Palatini $f(R)$ gravity, coupled with a matter action S_{m} depending on matter fields Ψ, is given by:

$$S[g,\Gamma,\Psi] = \frac{1}{2\kappa}\int f\big(R(\Gamma,g)\big)\sqrt{-g}\,d^4x + S_{\text{m}}[g,\Psi]. \tag{4.50}$$

Here, κ is a constant, $g_{\mu\nu}$ represents the spacetime metric, and $\Gamma^{\lambda}_{\mu\nu}$ is an independent and torsionless affine connection. Notably, $\Gamma^{\lambda}_{\mu\nu}$ is treated as an independent field separate from the spacetime metric, satisfying $\Gamma^{\lambda}_{\mu\nu} = \Gamma^{\lambda}_{\nu\mu}$.

The field equations derived from variations with respect to $g_{\mu\nu}$ and $\Gamma^{\mu}_{\nu\lambda}$ are given by:

$$f'(R)R_{\mu\nu} - \frac{1}{2}f(R)g_{\mu\nu} = \kappa T_{\mu\nu}, \tag{4.51}$$

$$\nabla_\lambda\left(\sqrt{-g}f'(R)g^{\mu\nu}\right) = 0. \tag{4.52}$$

The energy-momentum tensor $T_{\mu\nu}$ is defined by:

$$T_{\mu\nu} = -\frac{2}{\sqrt{-g}}\frac{\delta S_{\rm m}}{\delta g^{\mu\nu}}. \tag{4.53}$$

Equation (4.51), together with the matter field equations, leads to $\nabla^\mu T_{\mu\nu} \neq 0$, implying that the connection $\Gamma^{\lambda}_{\mu\nu}$ results in non-geodesic motion for test particles. This is in contrast to the metric $f(R)$ case. The trace of eq. (4.51) gives:

$$f'(R)R - 2f(R) = \kappa T. \tag{4.54}$$

This implies that R can be algebraically expressed as a function of T, unlike the metric $f(R)$ case. For the weak field limit, considering a specific $f(R)$ case given by $f(R) = R + \alpha R^2 + O(R^3)$, the field equation does not depend on α up to the first nontrivial order, and it is equivalent to the Einstein field equation for the metric $\overline{g}_{\mu\nu}$, coupling constant κ, and energy-momentum tensor $T_{\mu\nu}$.

In this weak field regime, the modified Poisson equation for the gravitational potential Φ becomes:

$$\nabla^2\Phi \approx \frac{\kappa}{2}\left(\rho + 2\alpha\nabla^2\rho\right). \tag{4.55}$$

This equation, derived from Palatini $f(R)$ gravity in [94], differs from the standard Poisson equation due to the additional term involving the parameter α. It is important to note that this modification arises from the unique features of Palatini gravity, and similar results hold for Eddington-inspired Born-Infeld (EiBI) gravity.

From eq. (4.55) with $\kappa = 8\pi G$, the expressions of $\Delta V^2_{\rm mod}$ and $\delta V^2_{\rm mod}$ for Palatini $f(R)$ are given by:

$$\Delta V^2_{\rm P}(r) = 8\pi G\alpha r\rho'(r), \tag{4.56}$$

leading to:

$$\delta V^2_{\rm P}(r_{\rm n}) = r_{\rm n}\frac{\rho'(r_{\rm n})}{\rho'(1)}. \tag{4.57}$$

The NAV plane for $f(R)$ Palatini gravity is illustrated in Fig. 4.10. Each blue curve represents one of the 122 bulgeless SPARC galaxies, generated using the $\delta V^2_{\rm P}$ expression (4.57). The dashed purple contours show the limits of the 1σ and 2σ highest density regions for Palatini.

Importantly, $\delta V^2_{\rm P}$ is independent of α, indicating that the NAV tests the shape of the additional contribution to the rotation curve, irrespective of its amplitude. The results show challenges for Palatini in covering the bottom part of the observational NAV region, with a notable excess of data outside the observational NAV region. These findings are independent of specific α values, which may vary from galaxy to galaxy.

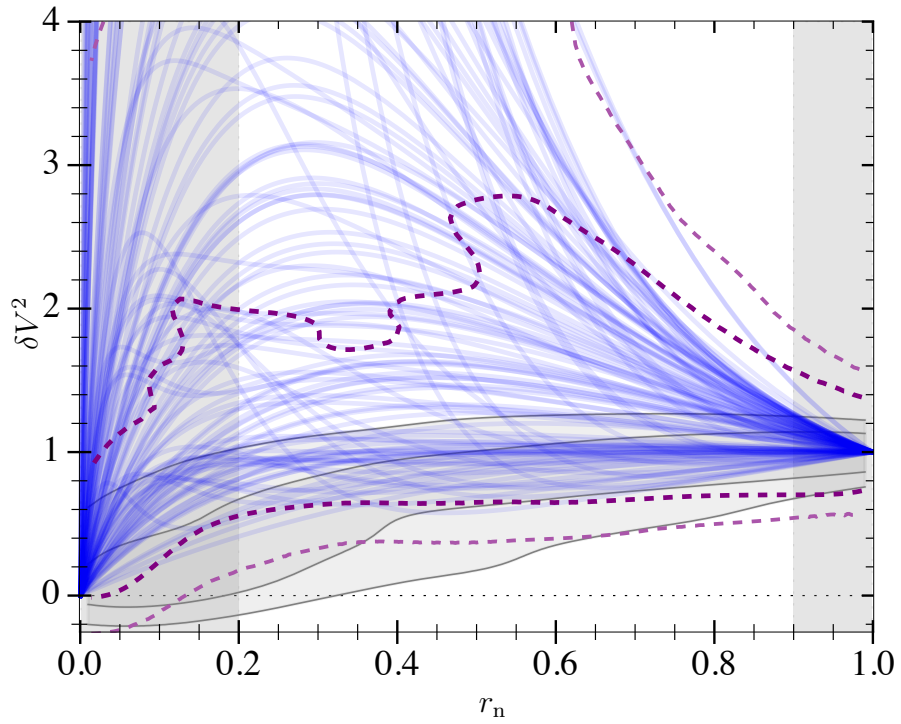

Figure 4.10: The NAV plane for $f(R)$ Palatini gravity is juxtaposed with the observational NAV plane. Each blue curve on the plot represents one of the 122 bulgeless SPARC galaxies. These curves are generated by employing the approximations outlined in this section, along with the $\delta V_{\rm P}^2$ expression given in (4.57). Image taken from [95].

The mean efficiency ranges from a maximum of $E_{\rm M} = 1$ (maximum concordance) to a minimum of $E_{\rm M} < -2.0$. According to the findings, Palatini $f(R)$ gravity, or any theory that satisfies eq. (4.57), is deemed incompatible with the observational data. This implies that such theories cannot serve as a replacement for dark matter in galaxies, regardless of variations in α from one galaxy to another.

Vainshtein Screening and Galaxy Rotation Curves

Current constraints on gravity are relatively weak on galactic and intergalactic scales. Screened modified gravity models can exhibit complex behavior there without violating stringent tests of gravity within our Solar System. They might hence provide viable extensions of the theory of gravity. Here, we use galaxy kinematics to constrain screened modified gravity models. We focus on Vainshtein screened dark matter models of gravity and predict its impact on galaxy rotation curves. This is achieved by post-processing the individual galaxy data from the SPARC catalogue, using the MAGMA and emcee codes. For a given galaxy, we determined the so called screening parameter γ, which determines if and galaxy is screened and how strong is it. After a careful selection of the appropriate galaxies, our findings show a mild screening for the vast majority of the galaxies that consider either the NFW or Burkert DM profiles, and a cluster non zero value for the screening parameter γ for either model. The locations of the cluster value appears not to be correlated with any relevant quantity as the mass, luminosity or galaxy distance, but it appears to be correlated with the galaxies for which the screening is actually plausible.

5.1 Introduction

In this preliminary section, we outline the overarching goals of our research. Our primary objective is to examine the impact of Υ on determining the dark matter within galaxies, with a specific emphasis on identifying the optimal Υ value that improves the goodness-of-fit for our models. We exclude galaxies deviating from this best-fit Υ value from subsequent analysis. To determine the global optimal Υ value, we adopt the approach outlined in [37], calculating posteriors for Υ up to 2σ and extending them using Gaussian distributions. It is essential to note that we refrain from dismissing the model by enforcing a constant Υ, acknowledging uncertainties in both baryonic factors and dark matter halo properties, suggesting the need for cosmological simulations for accurate halo characterization.

Our analysis will focus on the NFW and Burkert halos with the Υ parametrization. Gaussian priors will be employed for mass-to-light ratios, distance, and inclination, while a flat prior for Υ will be applied, bounded within -10 to 10. This broad range is chosen to allow for extensive exploration of the Υ distribution within the context of modified gravity.

Qualitative analyses have been preliminarily conducted, as referenced in [54], utilizing NAV analysis to estimate the most suitable Υ and r_s values. Preliminary results suggest an optimal Υ value around -2, corresponding to γ = -0.5. Our next step involves refining the 153 Υ distributions, ensuring each adheres to the specified Υ prior range. If necessary, these distributions will be extended as required.

Subsequently, we aim to determine the collective Υ distribution inferred from all galaxies and identify its mode. This process differs from finding the distribution of individual modes and will require a straightforward simulation. Additionally, we intend to investigate whether the best Υ value significantly differs from zero, with an expectation that it will be negative.

To further assess our findings, we will fix Υ at the mode value and reevaluate all galaxies using this new halo model, comparing its performance against the NFW model. Various metrics will be employed for this comparison, including the cumulative distribution function (CDF) of χ^2, as demonstrated in [74], or the Deviance Information Criterion (DIC). Ideally, we will compute the Bayes factor to quantify the relative strength of evidence between the two models.

5.2 Vainshtein mechanism, dark matter halo and the resulting effective potential

5.2.1 DHOST gravity effects inside matter

Kobayashi et al. [96] discovered a potential breakdown in the Vainshtein mechanism [97, 98, 99] within a matter distribution. While the mechanism might effectively operate outside a matter source, concealing deviations from General Relativity (GR) up to the Vainshtein radius, inside a matter distribution, these GR deviations may become significant. This observation is supported by the work of Koyama and Sakstein [100], who investigated a scalar-tensor gravitational model named G^3-galileon. This model, a specific instance of the beyond Horndeski Lagrangian [101], is subject to the Vainshtein screening mechanism.

Apart from the matter fields, the G^3-galileon action, in the Einstein frame, is given by

$$S[g,\phi] = \kappa \int \left(R - \frac{1}{2}\partial_\mu\phi\partial^\mu\phi + \frac{\mathcal{L}_4}{\Lambda^4} \right) \sqrt{-g}\, d^4x \,. \tag{5.1}$$

In the above, κ and Λ are constants and

$$\mathcal{L}_4 \equiv -X\left[(\Box\phi)^2 - \phi_{\mu\nu}\phi^{\mu\nu}\right] - (\phi^\mu\phi^\nu\phi_{\mu\nu}\Box\phi - \phi^\mu\phi_{\mu\nu}\phi_\sigma\phi^{\sigma\nu}) \,, \tag{5.2}$$

with $X \equiv -\frac{1}{2}\,\phi_\mu\phi^\mu$, $\phi_\mu \equiv \partial_\mu\phi$, and $\phi_{\mu\nu} = \nabla_\mu\nabla_\nu\phi$.

Disregarding the temporal evolution of perturbations and assuming a spherically symmetric scenario, Koyama and collaborators [100] identified an unscreened departure from General Relativity (GR) characterized by the constant Υ. In the Jordan frame, where the matter energy-momentum tensor $T_{\mu\nu}$ is conserved independently, a potential Φ can be defined from the perturbation in the time-time metric component (g_{00}). In the non-relativistic limit, this potential Φ satisfies $\mathbf{a} = -\nabla\Phi$, with $\mathbf{a}$ representing the acceleration vector field. From the G^3-galileon field equations, on finds that [100]

$$\Phi'(r) = G_\mathrm{N}\frac{M(r)}{r^2} + G_\mathrm{N}\frac{\Upsilon}{4}M''(r) \,, \tag{5.3}$$

where G_N is the Newtonian constant and Υ is a constant that depends on the ϕ field at the background level, denoted by ϕ_0, $\Upsilon = \left(\dot{\phi}_0/\Lambda\right)^4$. The scenario where $\Upsilon = 0$ corresponds to the conventional (Newtonian) case. In the G^3-galileon model, where both ϕ_0 and Λ must be nonzero, the equation (5.3) clearly indicates an unscreened contribution within the matter distribution.

The stipulation of $\Upsilon > 0$ is a characteristic of the specific G^3-galileon model under consideration. Other theories beyond Horndeski or Degenerate Higher-Order Scalar-Tensor (DHOST) theories [102] produce equation (5.3) with arbitrary Υ values [103, 104, 105].

5.2.2 Constraints on Υ

Phenomenological consequences of the gravitational force above have been explored in various scenarios, resulting in constraints on Υ due to the fifth force between baryons. These constraints commonly indicate $|\Upsilon| \lesssim 0.1$ [106] or $|\Upsilon| \lesssim 10^{-3}|$ [107]. Alternatively, it is plausible that the gravitational force between baryons adheres to Newtonian dynamics, while the gravitational interaction between baryons and dark matter deviates. In such a scenario, prior bounds on the Υ parameter may not be applicable. Testing this hypothesis is challenging, but feasible. First, let us briefly review this scenario.

To effectively test this scenario, an ideal cosmological simulation accounting for this gravitational interaction would be necessary. However, such simulations are computationally demanding and subject to inherent approximations. Therefore, it is crucial to evaluate qualitative aspects before engaging in detailed simulations. Two different approaches, to test the scenario above, can be considered in the context of galaxies: the fixed effective gravitational force, or the firxed dark matter distribution.

In regards to the fixed force approach, phenomenologically successful dark matter halos should accurately describe the effective gravitational force. In this scenario, the gravitational force experienced by baryons remains constant, while the dark matter distribution changes due to the altered gravitational interaction. Tests could examine whether the resulting dark matter distribution is plausible. Additionally, if dark matter particles can interact non-gravitationally with baryons or among themselves (e.g., via the weak force), this scenario has implications for direct dark matter detections, as it alters the local density of dark matter.

While for the fixed dark matter distribution approach assuming the gravitational force between dark matter particles approximates a Newtonian one (excluding cosmological constant effects), N-body dark matter simulations would provide a good approximation, and resultant dark matter halos should resemble Navarro-Frenk-White (NFW) profiles. This condition is satisfied in the scenario proposed by [108] and generally holds for sufficiently small Υ values. Even for larger Υ values, NFW may still be a good approximation, as N-body simulations for different gravitational theories often yield NFW-like halos [109, 110, 111, 112]. Several publications have employed the fixed-dark-matter-distribution approach for various models [100, 105, 108, 112, 113, 114, 115, 116]. For the G^3-galileon model, a preliminary analysis by [100] suggested that, for $\Upsilon = 0.5$, the impact on the rotation curve velocity of the Milky Way would be at most around 1%. More recent studies [105, 116] utilize the combination of internal dynamics and lensing data from galaxy clusters to propose that $\Upsilon \sim O(1)$ could moderately enhance the agreement with observational data compared to General Relativity.

5.2.3 Vainshtein-extended NFW halo

The NFW halo is defined by the following matter density [8, 36],

$$\rho_{\rm NFW}(r) = \frac{\rho_s}{\frac{r}{r_s}\left(1+\frac{r}{r_s}\right)^2}\,, \tag{5.4}$$

thus implying that the total DM mass inside the radius r is

$$M_{\rm NFW}(r) = 4\pi r_s^3 \rho_s \left(\ln(1 + r/r_s) - \frac{r/r_s}{1 + r/r_s} \right) . \tag{5.5}$$

For the NFW halo, the Newtonian acceleration together with the Vainshtein-screening violation term (5.3) leads to the following acceleration,

$$\Phi'(r) = G_{\rm N} \frac{M_{\rm NFW}(r) + \Upsilon M_\Upsilon(r)}{r^2} , \tag{5.6}$$

where

$$M_\Upsilon(r) = \frac{1}{4} r^2 M''_{\rm NFW}(r) = \pi \rho_s r_s \frac{1 - r/r_s}{(1 + r/r_s)^3} r^2 . \tag{5.7}$$

Utilizing the expression $\Phi' = v^2/r$ for the circular velocity of test particles, the same v^2 expression as found in [100] is derived. For $\Upsilon > 0$, the Vainshtein-breaking induces a circular velocity correction with the following characteristics:

- It is zero at $r = 0$.
- Positive in the region $0 < r < r_s$.
- Zero at $r = r_s$.
- Negative for $r > r_s$.
- Returns to zero in the limit $r \to \infty$.

Given that the Milky Way data extends beyond its r_s value, Koyama and Sakstein [100] observed a slight reduction in the circular velocity at large radii for $\Upsilon = 0.5$.

It is important to note that v^2, as defined above, need not be positive. A negative v^2 implies that the contribution to the centripetal acceleration is negative. If, at a particular radius, the total squared circular velocity is negative, then no circular orbits are possible at that radius. The circular velocity of a given component is commonly defined in the context of galaxy rotation curve analyses as follows: $v \equiv \text{sign}(v^2)\sqrt{|v^2|}$, ensuring that v is always real, and its sign reflects the sign of v^2.

5.3 Vainshtein Screening and χ^2 function

In this section we summarize the most relevant details of the models we studied. Defining $\gamma = \Upsilon/4$ and considering that only dark matter (DM) feels the modified gravity given by

$$\Phi'_M(r) = \Phi'_N(r) + \gamma G_N M''_{DM}(r) \quad , \quad M_{DM}(r) = 4\pi \int_0^r dr' r'^2 \rho_{DM}(r') \quad , \quad \Phi'_N(r) = G_N \frac{M_b(r)}{r^2}, \tag{5.8}$$

where $M_b(r)$ is the baryonic matter contribution, which includes stars, gas and, when is present, bulge; ρ_{DM} is the DM density, which will change according to the DM model considered, and M_{DM} is the mass corresponding to the DM density. Using the expressions of eqn. (5.8), we can express the circular velocity in a galaxy as

$$v(r) = r\Phi'_M(r). \tag{5.9}$$

This model is fitted to each galaxy in the SPARC catalog using the following χ^2 function

$$\chi^2\left(r_c, \rho_c, \gamma, \Upsilon_D, \delta, \theta\right) = \sum_{i=1}^{N} \left(\frac{V_M\left(r_i \mid r_c, \rho_c, \gamma, \Upsilon_D, \delta\right) - V_{c,i} \frac{\sin(\theta_{ref})}{\sin(\theta_{ref}+\theta)}}{\sigma_{V,i}} \right)^2 ,$$

$$V_M^2\left(r_i \mid r_c, \rho_c, \gamma, \Upsilon_D, \delta\right) = \delta\left\{\Upsilon_D |V_D(r_i)| V_D(r_i) + |V_g(r_i)| V_g(r_i)\right\} + \frac{G_N}{\delta}\left\{ \frac{m(r_i)}{r_i} + 4\pi\gamma\, r_i^2 \left(2\rho(r_i) + r_i \rho'(r_i\ )\right) \right\},$$

where the symbols are defined as follows

- N is the number of measured radius r_i for each galaxy.
- r_c is the characteristic radius of the DM profile.
- ρ_c is the characteristic density of the DM profile.
- γ is the screening parameter.
- Υ_D is the mass-to-light ratio for the disk.
- V_D is the disk velocity component, provided by the SPARC catalog.
- V_g is the gas velocity component, provided by the SPARC catalog.
- δ is the scaling error of the total distance to the galaxy, which modifies the internal distances on each galaxy according to $r_i' = (\delta) r_i$. This is just another way to account for the distance of the galaxy in the model, since this parameter is defined based on

  $$D + \Delta D \equiv D\left(1 + \frac{\Delta D}{D}\right) \equiv D\left(1 + \delta\right),$$

  where D denotes the distance from earth to the galaxy. Its introduction is done only because MAGMA was programmed to use account for the distance of the galaxy in the form of δ.
- $V_{c,i}$ denotes the total circular velocity measured at r_i, which is provided by the SPARC catalog.
- θ_{ref} denotes the reference inclination provided by the SPARC catalog, while θ denotes the error on the inclination of the galaxy to be fitted as a parameter of the model. Both are measured in degrees.
- $\sigma_{V,i}$ denotes the error on the total circular velocity measured at r_i, provided by the SPARC catalog.

Whenever the galaxy has a bulge, the model velocity V_M is modified as

$$V_M^2\left(r_i \mid r_c, \rho_c, \gamma, \Upsilon_D, \Upsilon_B, \delta\right) = (\delta)\left\{\Upsilon_B |V_B(r_i)| V_B(r_i) + \Upsilon_D |V_D(r_i)| V_D(r_i) + |V_g(r_i)| V_g(r_i)\right\} + \frac{G_N}{(\delta)}\left\{ \frac{m(r_i)}{r_i} + 4\pi\gamma\, r_i^2 \left(2\rho(r_i) + r_i \rho'(r_i\ )\right) \right\},$$

where Υ_B, V_B are the mass-to-light ratio and velocity component corresponding to the bulge, respectively.

Note that

- If there is no bulge, there are 6 parameters in the model, which are $r_c,\ \rho_c,\ \gamma,\ \Upsilon_D,\ \delta,\ \theta$. Whenever there is a bulge, a there are 7 parameters in the model, corresponding to $r_c,\ \rho_c,\ \gamma,\ \Upsilon_D,\ \Upsilon_B,\ \delta,\ \theta$.
- The absolute value was used because of the gas, whose velocity component can be negative in the innermost regions of a galaxy, generating an overestimation of the magnitude of the velocity if accounted just as the squared of the component. This is mainly generated when there is an great absence of gas in the central region of a galaxy, generating a stronger gravitational force of the outer parts when compared to the inner ones [6].

Special care must be taken with the screening parameter γ, since due to the fact this parameter is directly associated with the dark matter profile, there might be added singularities to the profile other than at $r \to 0$ or $r \to \infty$. To clarify this, consider first the NFW profile, which density is given by

$$\rho_{NFW} = \frac{\rho_s}{\frac{r_n}{rsn}\left(1+\frac{r_n}{r_{sn}}\right)^2}. \tag{5.10}$$

In there, the normalized radius $r_n = r/R_{max}$ and normalized characteristic radius $r_{sn} = rs/Rmax$ were used to further simplify the analysis (further details about this treatment can be seen in [54]). The normalized additional squared velocity generated by this profile is given by

$$\begin{aligned}\delta V^2_{NFW}(r_n) &= \frac{\Delta V^2_{NFW}(r_n R_{max})}{\Delta V^2_{NFW}(R_{max})} \\ &= \frac{(r_{sn}+1)^3\left(r_n\left(\gamma r_n(r_n-r_{sn})+(r_n+r_{sn})^2\right)+(r_n+r_{sn})^3(\log(r_{sn})-\log(r_n+r_{sn}))\right)}{r_n(r_n+r_{sn})^3\left(\gamma+r_{sn}(-\gamma+r_{sn}+2)+(r_{sn}+1)^3\log(r_{sn})-(r_{sn}+1)^3\log(r_{sn}+1)+1\right)}.\end{aligned}$$

The singularities of $\delta V^2_{NFW}(r_n)$ are located at

$$\gamma_{sing,NFW} = \frac{-r_{sn}^2-2r_{sn}+2(r_{sn}+1)^3\coth^{-1}(2r_{sn}+1)-1}{1-r_{sn}}.$$

Following the exact same procedure but now for the Burkert profile

$$\rho_{Burkert} = \frac{\rho s}{\left(\frac{r_n}{r_{sn}}+1\right)\left(\frac{r_n^2}{r_{sn}^2}+1\right)}, \tag{5.11}$$

we get

$$\begin{aligned}\delta V^2_{Burkert}(r_n) &= \frac{\Delta V^2_{Burkert}(r_n R_{max})}{\Delta V^2_{Burkert}(R_{max})} \\ &= \frac{\log\left(r_n^2+r_{sn}^2\right)+\frac{4\gamma r_n^3\left(-r_n^3+r_n r_{sn}^2+2r_{sn}^3\right)}{(r_n+r_{sn})^2(r_n^2+r_{sn}^2)^2}+2\log(r_n+r_{sn})-2\tan^{-1}\left(\frac{r_n}{r_{sn}}\right)-4\log(r_{sn})}{r_n\left(\log\left(r_{sn}^2+1\right)+\frac{4\gamma(2r_{sn}^3+r_{sn}^2-1)}{(r_{sn}^3+r_{sn}^2+r_{sn}+1)^2}-4\log(r_{sn})+2\log(r_{sn}+1)-2\cot^{-1}(r_{sn})\right)},\end{aligned}$$

which leads to

$$\gamma_{sing,Burkert} = \frac{\left(r_{sn}^3+r_{sn}^2+r_{sn}+1\right)^2\left(-\log\left(r_{sn}^2+1\right)+4\log(r_{sn})-2\log(r_{sn}+1)+2\cot^{-1}(r_{sn})\right)}{4\left(2r_{sn}^3+r_{sn}^2-1\right)}.$$

The functions $\gamma_{sing,NFW}$ and $\gamma_{sing,Burkert}$ are shown in Fig. 5.1. These plots mean that the screening parameter γ must be restricted to specific intervals in order not to have any singularity, and these intervals are specified in the table below

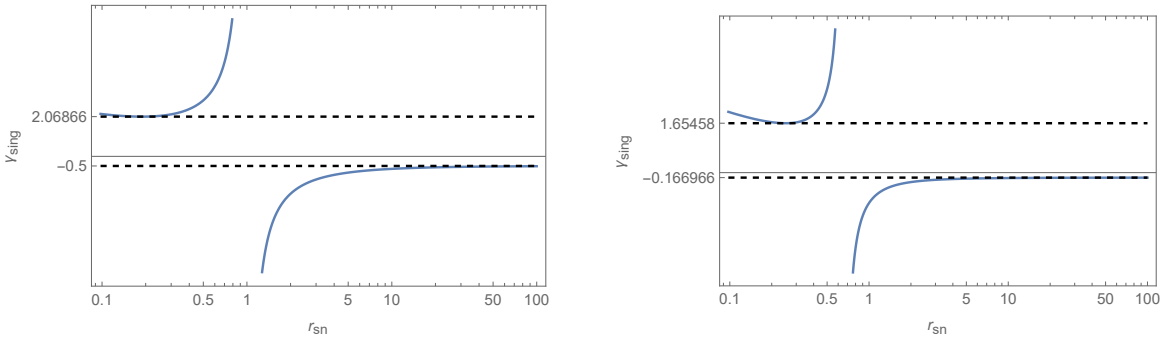

(a) NFW profile.

(b) Burkert profile.

Figure 5.1: γ_{sing} for each profile.

	γ Interval Limits	
Profile	**Lower Limit**	**Upper Limit**
Burkert	-0.166966	1.65458
NFW	-0.5	2.06866

Table 5.1: Intervals the screening parameter.

5.4 Model parametrization and priors

In order to cross check our work, we take as reference the results from [74] and re-parametrize the model in in terms of the variables

$$c_{200} = \frac{r_{200}}{r_c} \quad , \quad v_{200} = 10 c_{200} r_c H_0$$

where $H_0 = 73$ km s^{-1} Mpc^{-1} following the SPARC catalog assumption. With that, the parameters of the models now are as follows

- When there is no bulge, the parameters are c_{200}, v_{200}, γ, Υ_D, df2, D_{inc}.
- When there is a bulge, the parameters are c_{200}, v_{200}, γ, Υ_D, Υ_B, df2, D_{inc}.

Taking that into account, we used the MAGMA Mathematica based program developed by professors Davi Rodrigues and Valerio Marra [7] to find the best fit values of the parameters mentioned above for each galaxy, and using the best fit as starting point, I then run emcee with 2000 steps per walker, and 200 walkers to sample the posterior of each galaxy, which provides 400000 points per galaxy. It is important to note that before that, a burn in phase of 1000 steps per walker was run in order to discard non relevant points for the posterior. The priors used for each parameter were the following

- Flat prior $0 < c_{200} < 1000$ following [74].
- Flat prior $10\frac{\text{km}}{\text{s}} < v_{200} < 500\frac{\text{km}}{\text{s}}$ following [74].

- Flat prior on γ according to the intervals summarized on Table 5.1. The γ parameter is dimensionless.
- Gaussian prior on Υ_D with mean $0.5\frac{M_\odot}{L_\odot}$ and variance $0.1\frac{M_\odot}{L_\odot}$. Plus, for consistency it is required $\Upsilon_D > 0$. This is equivalent to the lognormal prior used in [74].
- When needed, gaussian prior on Υ_B with mean $0.6\frac{M_\odot}{L_\odot}$ and variance $0.1\frac{M_\odot}{L_\odot}$. Plus, for consistency it is required $\Upsilon_B > 0$. This is equivalent to the lognormal prior used in [74].
- Gaussian prior on df2 with mean 1 and variance given by the error on the distance of the galaxy divided by the distance of the galaxy itself $\frac{\delta D}{D}$. This is equivalent to the gaussian prior for D used in [74].
- Gaussian prior on θ with mean and variance given by the values for each galaxy on the SPARC catalog.

All the above discussed priors are the same regardless of the dark model profile used.

5.5 Screening Results

It is worth nothing that some quality cuts were made for this analysis, specifically, out of the 185 total SPARC galaxies

- 10 galaxies were cut due to having inclination $i < 30°$, these correspond to face on galaxies which are not appropriate for galaxy rotation fitting as done in this work.
- Twelve galaxies with asymmetric rotation curves labelled with quality flag $Q = 3$ were excluded as well since those manifestly do not trace the equilibrium gravitational potential.

The previous cuts are the same done for the Radial Acceleration Relation [6], which leaves 153 total galaxies, upon which a minimum precision of 10% in velocity is further required, leaving a total of 2693 combined data points so far. In our analysis, we further impose other cuts mainly related with the screening parameter, which are specified below.

- We exclude galaxies which have 0 degrees of freedom for which our model would uniquely fit these galaxies, therefore leaving no room to either affirm or negate our model. This is independent of the DM profile used and there are a total of 11 excluded galaxies, which are D512-2, D564-8, NGC4068, NGC4138, NGC6789, UGC00634, UGC00891, UGC05414, UGC06923, UGC07232, and UGC09992.
- Since in our fits we use the python program emcee, we follow the guidelines given in [117] to assess the convergence of the chains, and imposing that the mean acceptance fraction of the entire chain for each galaxy to be between 0.2 and 0.5, a total of 16 galaxies are excluded for the Burkert profile, which are DDO161, ESO079-G014, ESO563-G021, IC2574, IC4202, NGC0024, NGC0801, NGC3953, NGC6674, UGC00891, UGC02916, UGC02953, UGC03546, UGC05764, UGC11820, and UGC11914. Similarly, 33 galaxies are excluded for the NFW profile, which are D564-8, DDO064, DDO161, ESO079-G014, ESO116-G012, F571-8, F583-4, IC2574, NGC3521, NGC3953, NGC5585, NGC6674, NGC6946, UGC00191, UGC00634, UGC00891, UGC02487, UGC02916, UGC02953, UGC03546, UGC04278, UGC05253, UGC05414, UGC05716, UGC05764, UGC05829, UGC05986, UGC06787, UGC07323, UGC08699, UGC11557, UGC11820, and UGC11914.

That leaves 127 total galaxies to be analyzed in the Burkert profile and 113 in the NFW profile. The core of our analysis focuses on the γ parameter, therefore, in what follows we are going to solely focus on analyzing the behavior of it galaxy by galaxy. To begin with Figures 5.2 and 5.3 shows the modes of the γ distributions for all studied SPARC galaxies in each model.

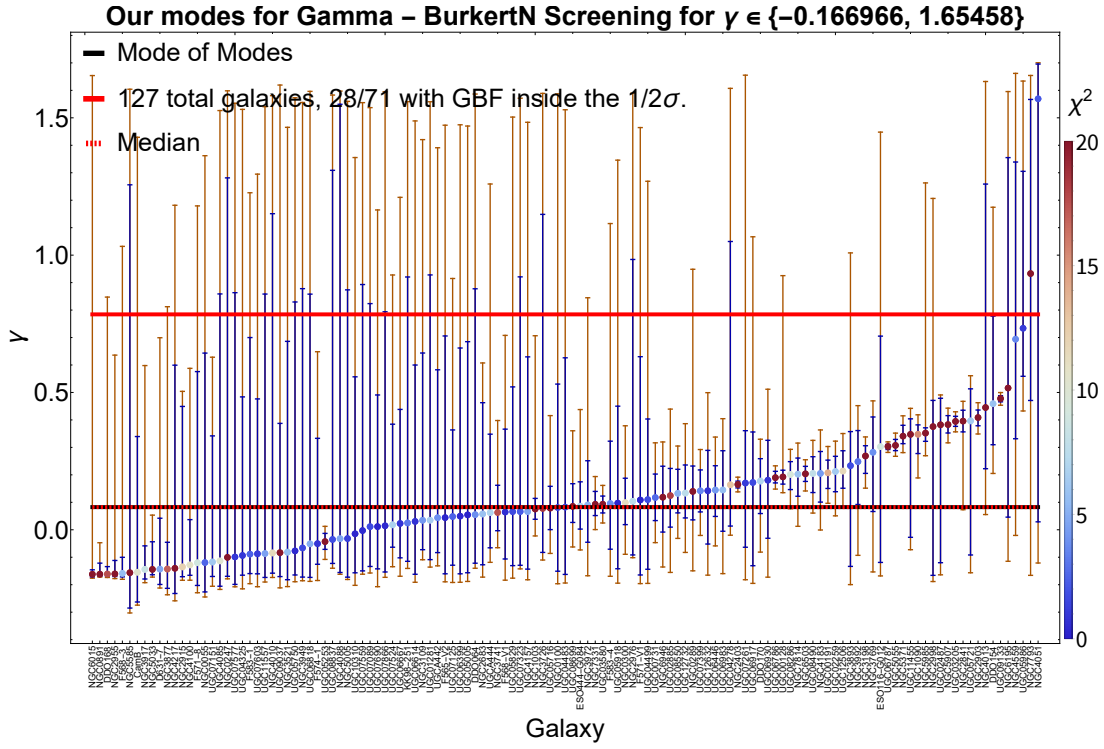

Figure 5.2: γ parameter color-coded with the χ^2 value in the Burkert profile. The blue and orange intervals represent the 1σ and 2σ regions.

Alternatively, the same plots are shown below but this time colored according to the χ^2_{Red} value of each galaxy. The Mode of modes references in the above figures refers to considering all the modes shown, and calculating the mode of their (smooth-kernel) distribution. The explicit distributions of the modes are shown in Figure 5.6 along side with their respective modes and the location of the global best fits for each profile. The global best fit was calculated following the same procedure as in [7], beyond that, the rejection level was also calculated according to the details in the aforementioned article, which just to have present in this article directly, we repeat below.

5.5.1 Global best fit.

For each galaxy we compute the mean and the variance of the posterior according to:

$$\bar{\gamma}_j = \int \mathrm{d}\gamma\, \gamma\, f_j(\gamma)\,, \tag{5.12}$$

$$\sigma^2_{\gamma,j} = \int \mathrm{d}\gamma\, (\gamma - \bar{\gamma}_j)^2\, f_j(\gamma)\,, \tag{5.13}$$

where $f_j(\gamma)$ is the (marginalized) posterior on γ for the galaxy j, with $1 \leq j \leq N$ where N is the number of galaxies that passed the quality cuts discussed above. Then, in order to find the

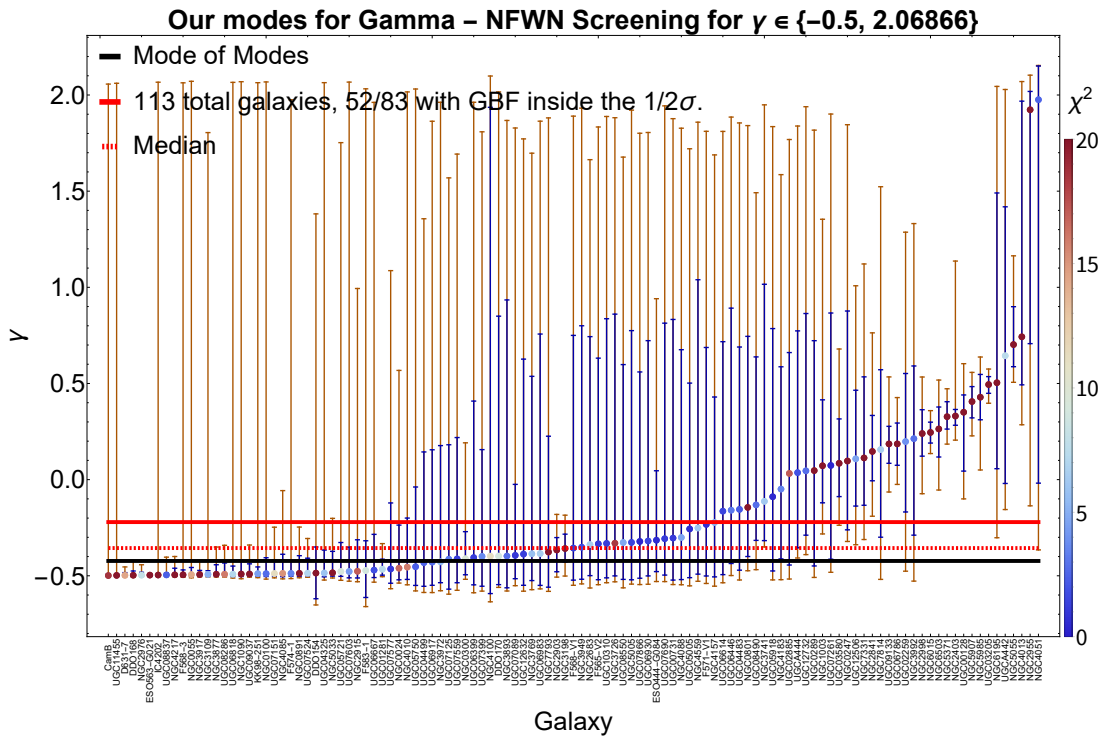

Figure 5.3: γ parameter color-coded with the χ^2 value in the NFW profile. The blue and orange intervals represent the 1σ and 2σ regions.

global best-fit value of γ we introduce the following χ^2 statistic:

$$\chi^2(\gamma) = \sum_{j=1}^{N} \frac{(\bar{\gamma}_j - \gamma)^2}{\sigma^2_{\gamma,j}}\,, \tag{5.14}$$

which follows a χ^2-distribution with $k = N - 1$ degrees of freedom, under the approximation that the γ values for the $j-th$ galaxy are distributed according to a Gaussian distribution with mean $\bar{\gamma}_j$ and variance $\sigma^2_{\gamma,j}$. This key assumption may not be true for almost any of the galaxies in our study as it is shown in Figures 5.7 and 5.8, since not only the mode and mean are in general very far apart from each other, but also the 1σ region is not symmetrical.
Despite this, for the moment we proceed with the calculations and the minimization of $\chi^2(\gamma)$ yields the "global best fit" γ^{bf}.

5.5.2 Confidence level in rejecting a single global screening parameter.

As the degrees of freedom k of the χ^2 defined in Equation (5.14) is high ($k \sim 100$), we can approximate the χ^2-distribution with a Gaussian with mean k and standard deviation $\sqrt{2k}$. We can then estimate the number of σ at which MOND is rejected according to:

$$n_\sigma = \frac{\chi^2(\gamma^{bf}) - k}{\sqrt{2k}}\,. \tag{5.15}$$

Table 5.2 presents a compendium of all the results for the screening case so far. It appears that some galaxies with too high of χ^2 or χ^2_{Red} could be removed due to lying very far away from

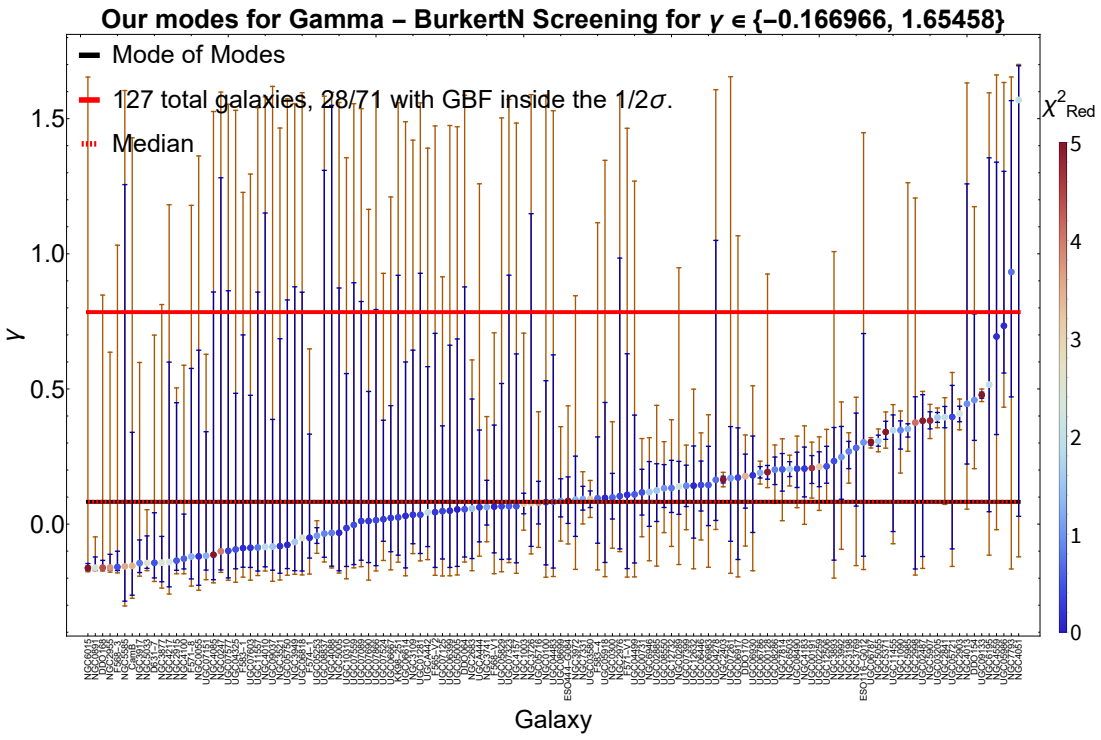

Figure 5.4: γ parameter color-coded with the χ^2_{Red} value in the Burkert profile. The blue and orange intervals represent the 1σ and 2σ regions.

	Bayesian Approach			
Profile	**Global Best Fit γ^{bf}**	**1σ(31.73%)**	**2σ(4.55%)**	**Rejection Level n_σ**
Burkert	0.78	77.95	44.10	596.94
NFW	-0.22	48.03	23.62	45.76

Table 5.2: Summary of the results for the screening parameter γ so far.

the median (or mode of modes or even the global best fit). This is further emphasized in the cumulative distributions of χ^2 and χ^2_{Red} values for each profile shown in Figures 5.9 and 5.10. Several model comparisons were performed between each profile and the ΛCDM case, beginning with the BIC and DIC statistics displayed in Figures 5.11 and 5.12, where we define values in the range $|\Delta BIC| > 2$ as 'mildly significant', and values in the range $|\Delta BIC| > 6$ as 'strongly significant' as explained in [118].

Table 5.3 presents a compendium of all the results for the model comparisons so far. It is relevant to note that the BIC and DIC differ according to the strength to which one model is preferred over the other. According to the BIC results, 48.82%(62/127) of the galaxies in the Burkert profile have some preference for the Screening model, while 68.14%(77/113) of the galaxies in the NFW have some preference for the Screening model. Emphasis should be made on the fact that it is only

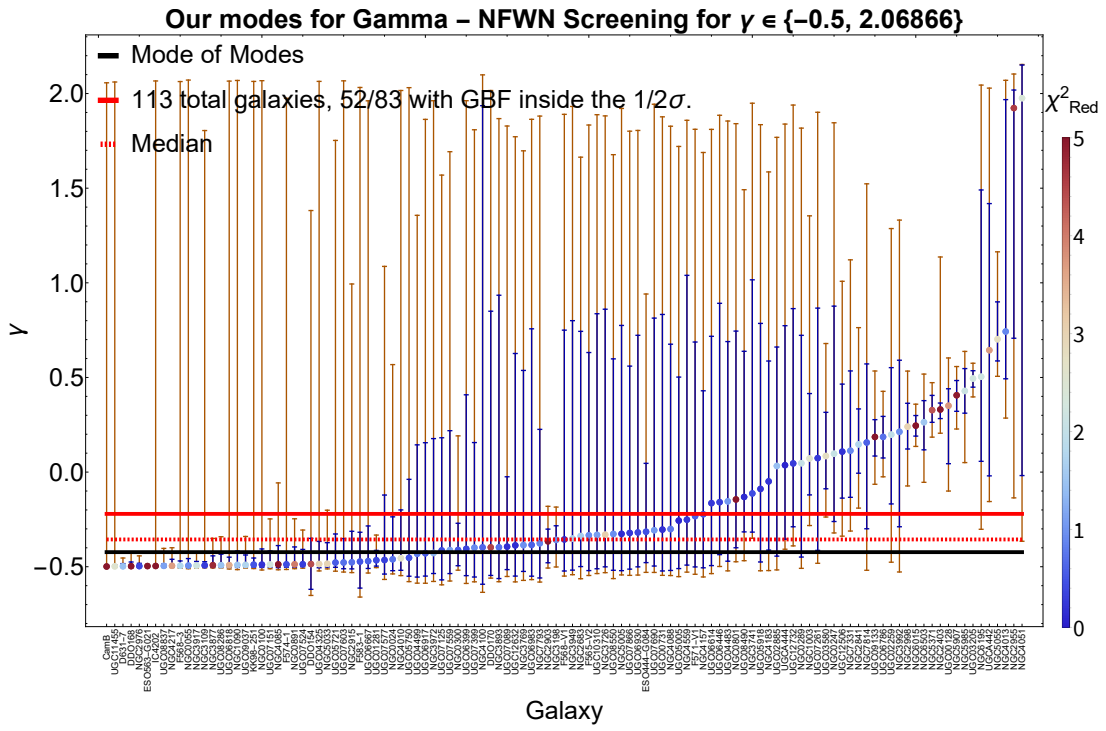

Figure 5.5: γ parameter color-coded with the χ^2_{Red} value in the NFW profile. The blue and orange intervals represent the 1σ and 2σ regions.

	Percentages for strong preference			
Profile	BIC-Screening(%)	BIC-ΛCDM(%)	DIC-Screening(%)	DIC-ΛCDM(%)
Burkert	22.83	0.79	11.81	58.27
NFW	30.97	1.77	26.55	54.87

Table 5.3: Summary of the results for the screening parameter γ so far.

for some screening model since as shown in Table 5.2, the rejection levels for the global best fits in each case are way high. On the other hand, those percentages are much smaller according to the DIC results, which indicate that only 30.71%(39/127) of the galaxies in the Burkert profile have some preference for the Screening, and 36.28%(41/113) of the galaxies in the NFW profile have some preference for the Screening model. That is, as whole, the BIC statistics seems to suggest that around half or more of the galaxies prefer the screening model in either profile, which is in contrast with what the DIC statistics appears to suggest, with only around 30% of the galaxies showing such preference. This discrepancy can also be seen in the percentages shown in Table 5.3, where the strong preference percentages for ΛCDM according BIC are significantly smaller than according to DIC.

We also performed a Log-likelihood and χ^2_{Red} model comparison as shown in Figures 5.13 and

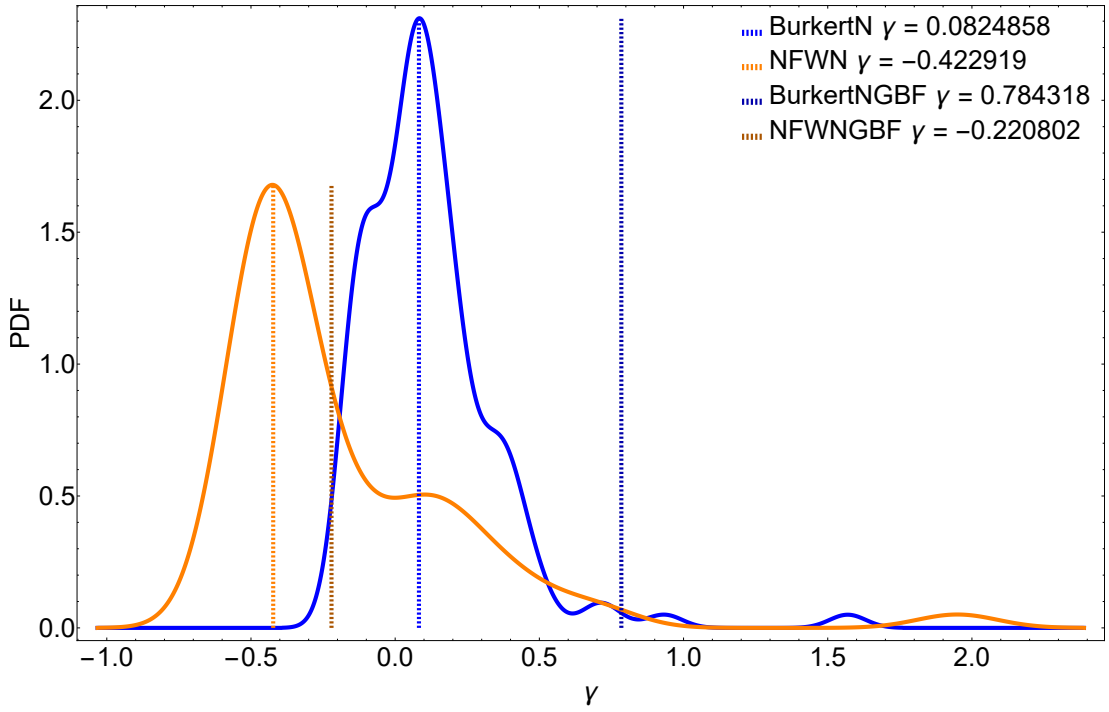

Figure 5.6: Modes distribution for the Dm profiles.

5.14.

These last model comparisons present again some discrepancies between them. According to the Log-Likelihood test, almost all the galaxies (90% or more) prefer the Screening model, while according to the χ^2_{Red} test, using the Burkert profile leads to a ΛCDM preference of the galaxies, and using the NFW profile leads to Screening Preference of the galaxies. Table 5.4 presents a compendium of the results of the last model comparisons made.

	Last model comparison preferences	
Profile	**Log-Likelihood test**	$\boldsymbol{\chi^2_{Red}}$ **test**
Burkert	Screening (89.76%)	ΛCDM (1.00857)
NFW	Screening (95.56%)	Screening (1.08083)

Table 5.4: Summary of the results for the last model comparison made.

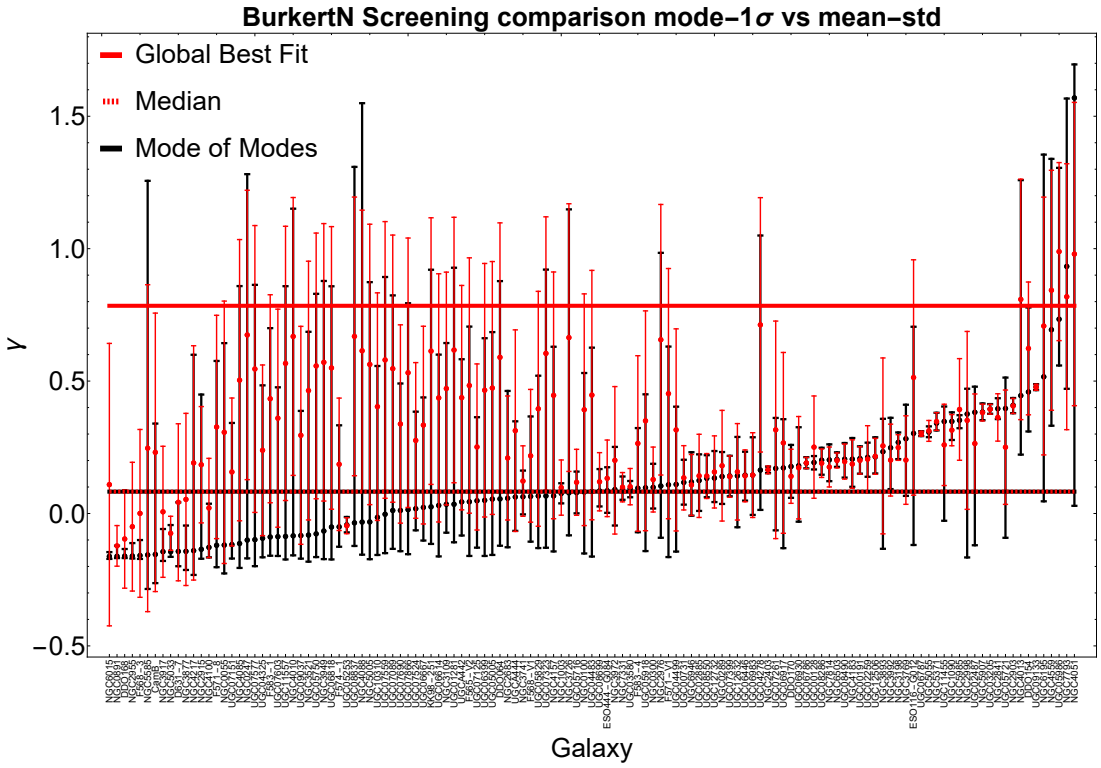

Figure 5.7: 1σ region vs mean and standard deviation comparison for the γ in the Burkert profile. The black points and bars correspond to the mode and 1σ region respectively, and the red points and bars to the mean and standard deviation respectively.

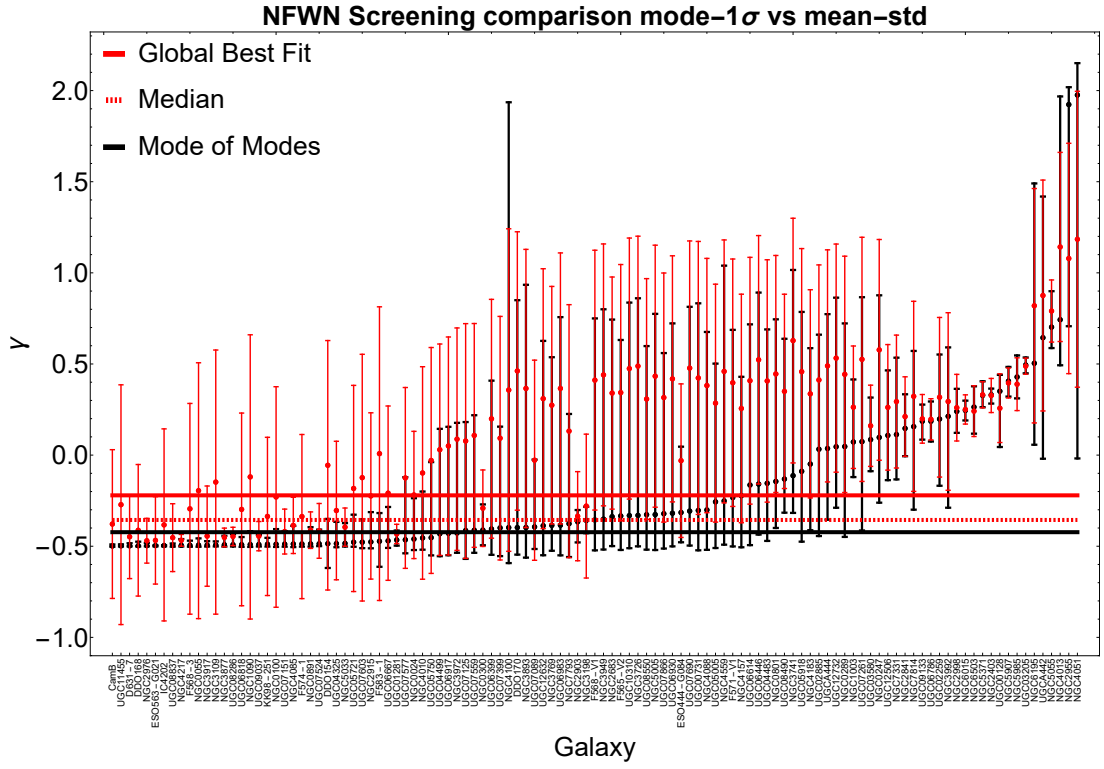

Figure 5.8: 1σ region vs mean and standard deviation comparison for the γ in the NFW profile. The black points and bars correspond to the mode and 1σ region respectively, and the red points and bars to the mean and standard deviation respectively.

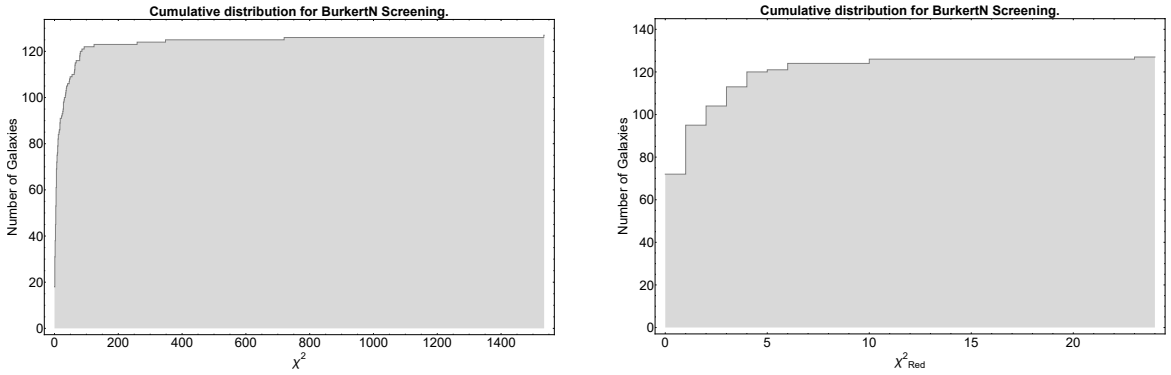

(a) χ^2 cumulative histogram.

(b) χ^2_{Red} cumulative histogram.

Figure 5.9: Cumulative l best fit). This is further emphasized in the cumulative histograms of χ^2 and χ^2_{Red} histograms for the burkert profile.

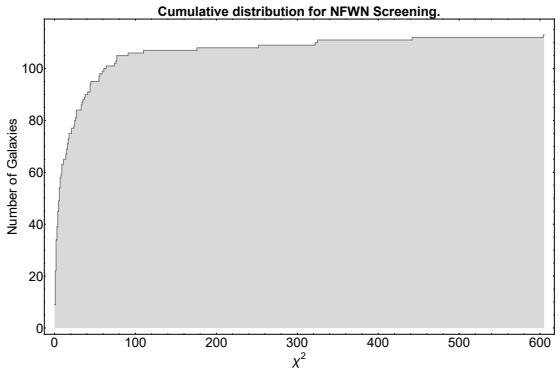

(a) χ^2 cumulative histogram.

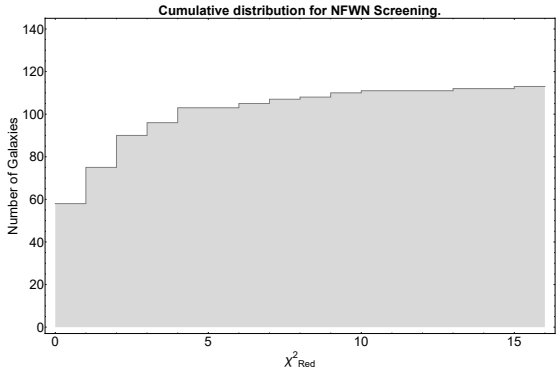

(b) χ^2_{Red} cumulative histogram.

Figure 5.10: Cumulative l best fit). This is further emphasized in the cumulative distributions of χ^2 and χ^2_{Red} histograms for the NFW profile.

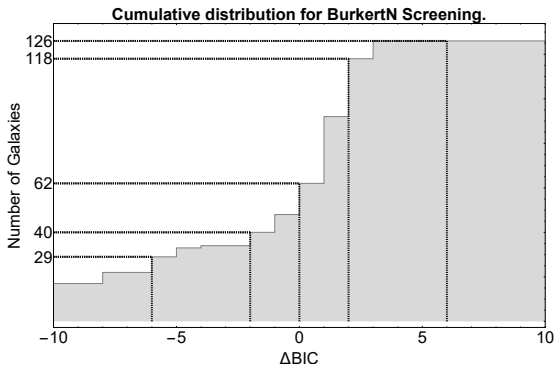

(a) ΔBIC cumulative histogram.

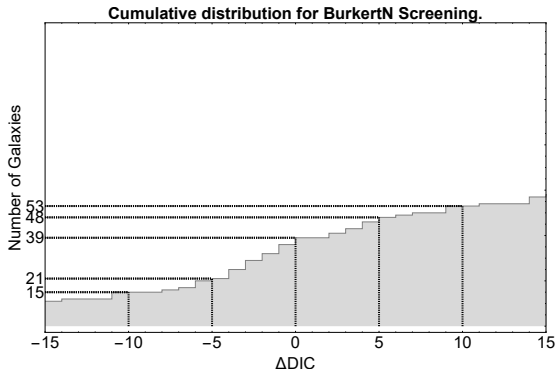

(b) ΔDIC cumulative histogram.

Figure 5.11: Cumulative ΔBIC and ΔDIC histograms for the burkert profile.

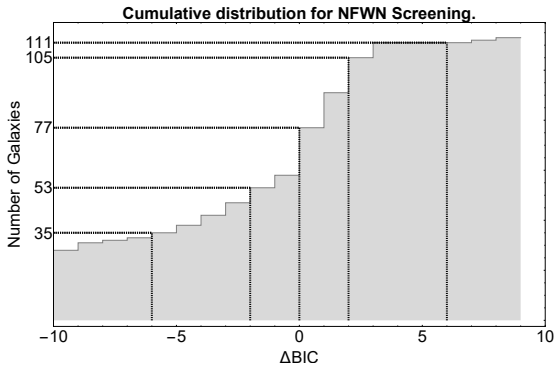

(a) ΔBIC cumulative distribution.

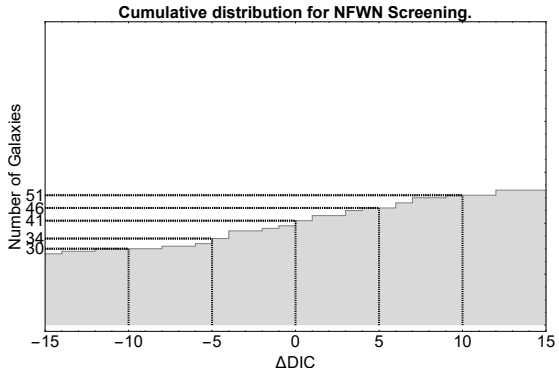

(b) ΔDIC cumulative distribution.

Figure 5.12: Cumulative ΔBIC and ΔDIC histograms for the NFW profile.

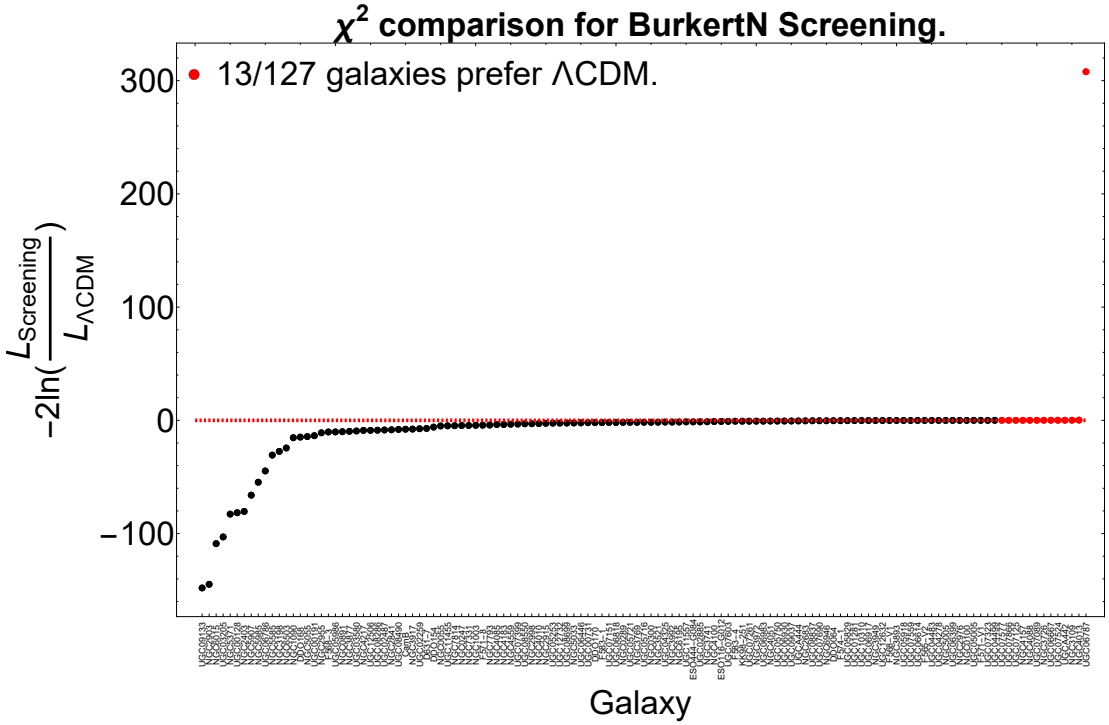

(a) χ^2 model comparison.

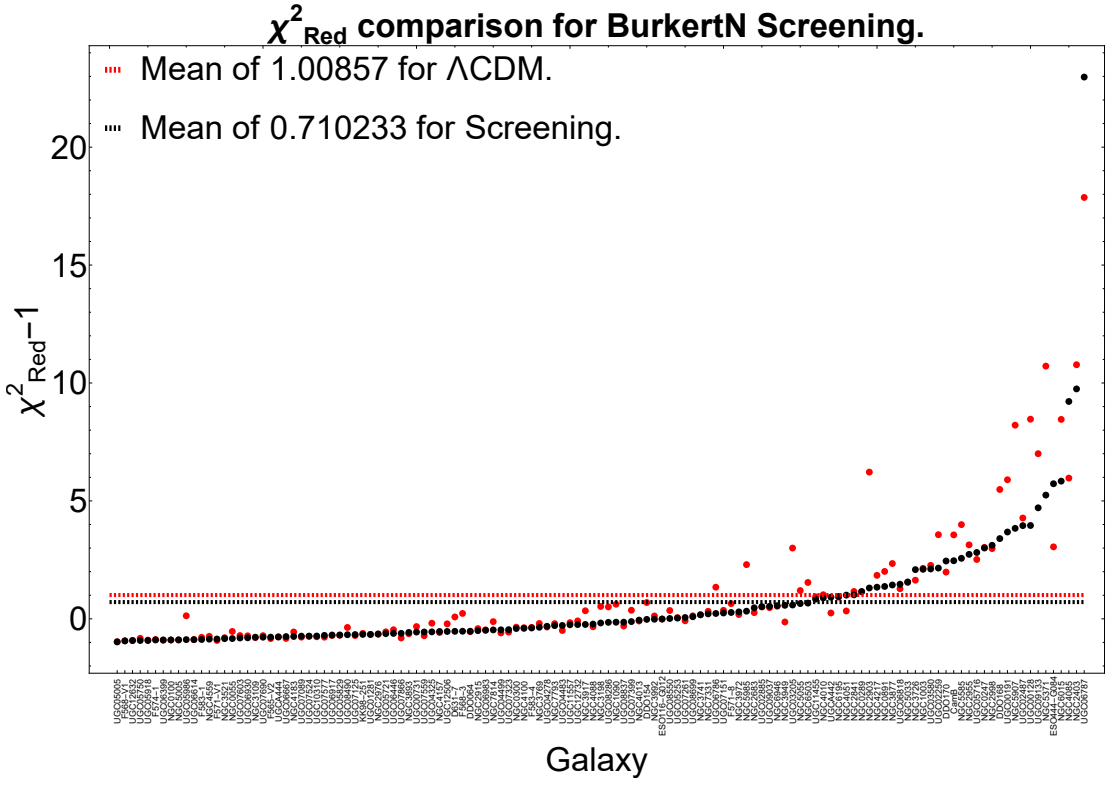

(b) χ^2_{Red} model comparison.

Figure 5.13: Screening vs ΛCDM model comparisons in the Burkert profile.

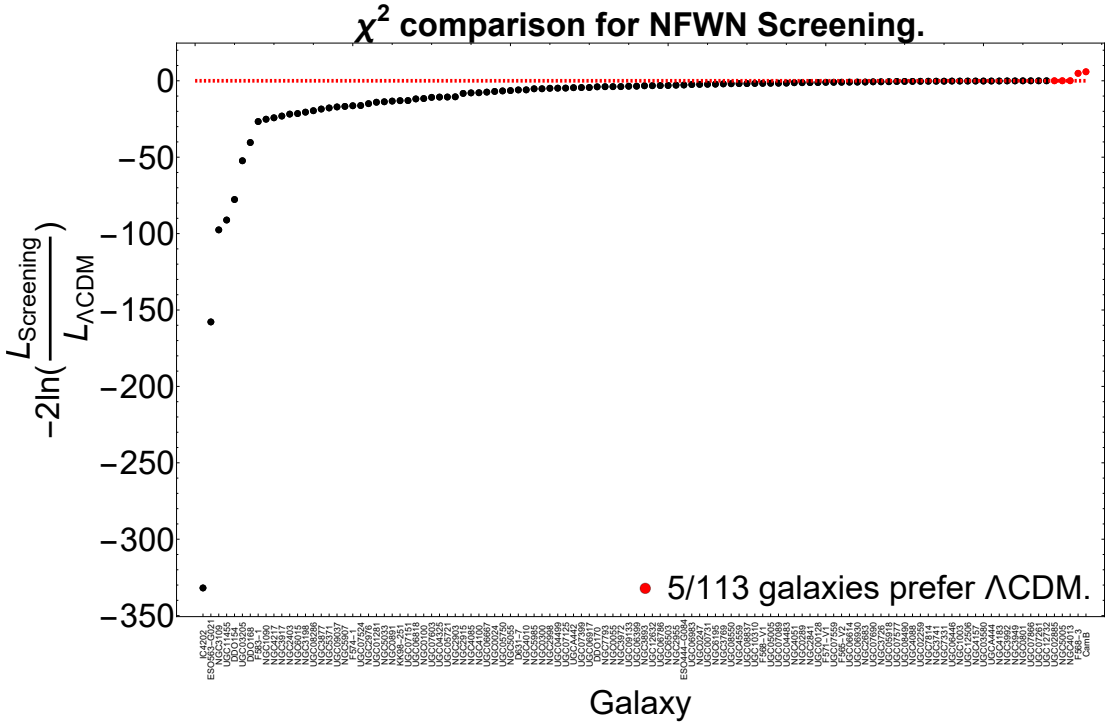

(a) χ^2 model comparison.

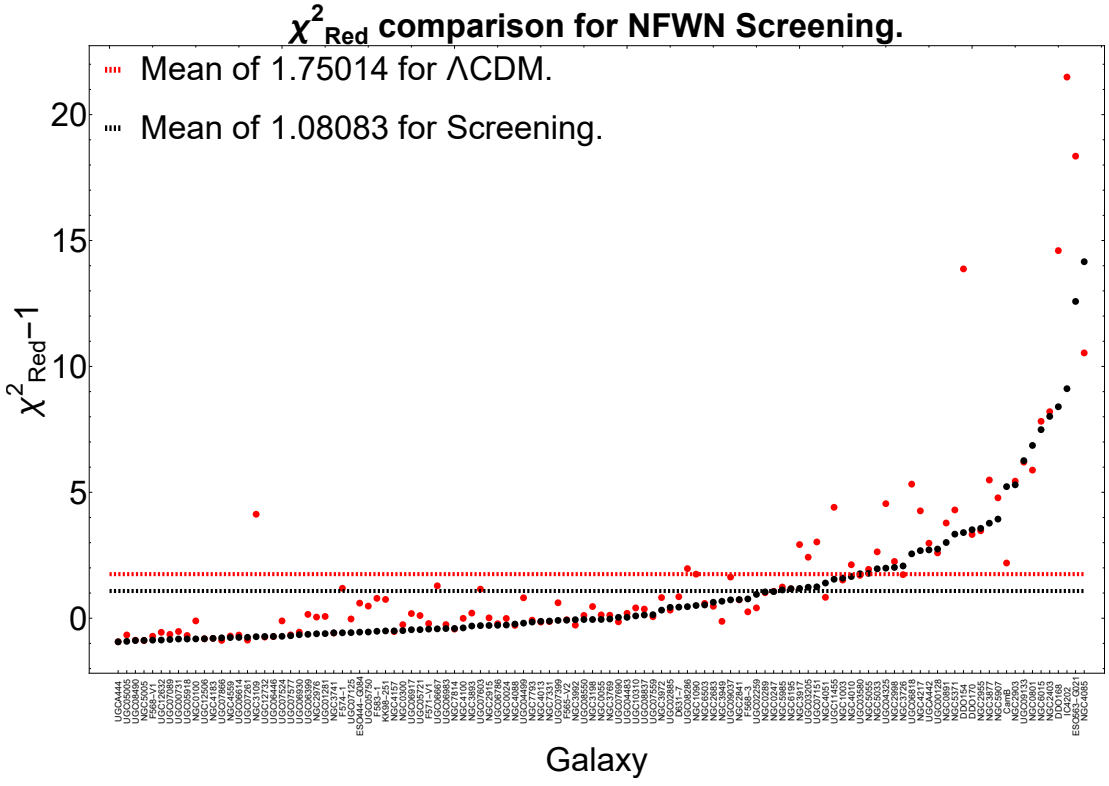

(b) χ^2_{Red} model comparison.

Figure 5.14: Screening vs ΛCDM model comparisons in the NFW profile.

Conclusions

We have introduced a method, based on the normalized additional velocity (NAV) (4.7), for a comprehensive study of galaxy rotation curves (RCs) directly from a galaxy sample. Inspired by previous analyses [119, 120] and a normalized version of [55], this approach focuses on the radial dependence of the expected dark matter contribution or non-Newtonian contribution in modified gravity. The method, while not designed as a complete data assessment, efficiently compares galaxies in terms of a crucial aspect of RCs—their shape. Applications include eliminating model parameter regions, identifying probable parameter regions, revealing intricate trends not easily discernible from standard individual fits, and model comparisons.

The SPARC galaxy sample [6] provides essential observational data for NAV evaluation (see Fig. 4.2). The method, relevant even analytically for some models, simplifies the analysis by commonly eliminating one model parameter, enabling data-based inferences on the remaining parameters.

Establishing a correlation between the NAV analysis and average minimum χ^2 values (as discussed in Sec. 4.2), Table 4.1 confirms such a relationship.

We considered five models: three dark matter profiles (NFW, Burkert, and DC14 profiles), a modified gravity model (MOND), and a phenomenological model, Arctan_α. The $\text{Arctan}_{\alpha=1}$ model, tested primarily to assess the NAV method, proved efficient in providing good rotation curve fits. Although we did not explicitly evaluate the pseudo-isothermal model [e.g., 121], similar results are expected. The $\text{Arctan}_{\alpha=1/2}$ model, as anticipated from NAV analysis and confirmed by individual fits, performed significantly worse.

For SPARC galaxies, the NAV method illustrated that, on average, the Burkert halo outperforms NFW and $\text{Arctan}_{\alpha=1/2}$. The result is unrelated to the core-cusp issue but pertains to the necessary diversity of dark matter halos, a feature lacking in NFW. The DC14 halo, presenting a more improved physical picture, similarly demonstrates the capability to provide diverse halo shapes, aligning with previous findings [52, 74].

MOND, in its original form, adeptly covers the central NAV plane, but like the NFW halo, it lacks diversity, resulting in large individual fit χ^2 values. This aligns with findings from [85, 87], though derived through a distinct method.

The NAV method can be extended to broader modified gravity models. For MOND, this is straightforward due to its rotation curve being expressed as a function of V_{bar}^2. For other modified

gravity models requiring knowledge of the three-dimensional baryonic matter distribution [see 122, for details], this method offers a promising approach. We intend to extend its applicability in this direction.

Regarding the Vainshtein screening analysis, it is important to highlight that the Vainshtein screening work is still in very early stages, but so far, we have found promising results which we summarize briefly here. Despite model selection differences, the key conclusion is that, at this stage, there is no single preferred screening parameter value adhered to by all galaxies. Even after removing galaxies with substantial χ^2 or χ^2_{Red} values, a single globally preferred screening model parameter value is unlikely to emerge. While χ^2-based comparisons generally favor the screening model over ΛCDM, χ^2_{Red}-based comparisons yield mixed results. The most robust test, the Deviance Information Criterion (DIC), suggests that more than half of the galaxies prefer ΛCDM. Ongoing work involves calculations with a fixed screening parameter value to directly compare whether a single global γ screening model performs better or worse than ΛCDM for individual galaxy fits, but initial expectations lean toward no clear preference. If a universal γ is assumed to exist, we recently performed a test based on the combination of the posteriors and find that the value of $\gamma = -2$ is favored. This result will be further developed in a future publication.

Bibliography

[1] J. H. Oort. *The force exerted by the stellar system in the direction perpendicular to the galactic plane and some related problems.* Bulletin Astronomical Institute of the Netherlands **6** 249 (1932). Cited on page 1.

[2] F. Zwicky. *Die Rotverschiebung von extragalaktischen Nebeln.* Helvetica Physica Acta **6** 110 (1933). Cited on page 1.

[3] F. Zwicky. *On the Masses of Nebulae and of Clusters of Nebulae.* Astrophysical Journal **86** 217 (1937). Cited on page 1.

[4] J. H. Oort. *Some Problems Concerning the Structure and Dynamics of the Galactic System and the Elliptical Nebulae NGC 3115 and 4494.* Astrophysical Journal **91** 273 (1940). Cited on page 1.

[5] K. C. Freeman. *On the Disks of Spiral and S0 Galaxies.* Astrophysical Journal **160** 811 (1970). Cited on pages 1 and 6.

[6] F. Lelli, S. S. McGaugh, and J. M. Schombert. *SPARC: Mass Models for 175 Disk Galaxies with Spitzer Photometry and Accurate Rotation Curves.* Astronomical Journal **152** 157 (2016). arXiv:1606.09251. Cited on pages 2, 12, 16, 23, 50, 52, and 63.

[7] D. C. Rodrigues, V. Marra, A. del Popolo, and Z. Davari. *Absence of a fundamental acceleration scale in galaxies.* Nature Astronomy **2** 668 (2018). arXiv:1806.06803. Cited on pages 2, 28, 35, 41, 51, and 53.

[8] J. F. Navarro, C. S. Frenk, and S. D. M. White. *A Universal Density Profile from Hierarchical Clustering.* Astrophysical Journal **490** 493 (1997). arXiv:astro-ph/9611107. Cited on pages 1, 9, 25, 31, and 47.

[9] C. M. Will. *The Confrontation between General Relativity and Experiment.* Living Reviews in Relativity **17** 4 (2014). arXiv:1403.7377. Cited on page 2.

[10] K. Akiyama et al. *First M87 Event Horizon Telescope Results. I. The Shadow of the Supermassive Black Hole.* Astrophysical Journal **875** L1 (2019). arXiv:1906.11238. Cited on page 5.

[11] E. Opik. *An estimate of the distance of the Andromeda Nebula.* Astrophysical Journal **55** 406 (1922). Cited on page 5.

[12] E. P. Hubble. *A spiral nebula as a stellar system, Messier 31.* Astrophysical Journal **69** 103 (1929). Cited on page 5.

[13] H. S. Leavitt. *1777 variables in the Magellanic Clouds.* Annals of Harvard College Observatory **60** 87–108 (1908). Cited on page 5.

[14] H. S. Leavitt and E. C. Pickering. *Periods of 25 Variable Stars in the Small Magellanic Cloud.* Harvard College Observatory Circular **173** 1 (1912). Cited on page 5.

[15] E. P. Hubble. *The Realm of the Nebulae.* Yale University Press 1936. Cited on page 5.

[16] G. de Vaucouleurs. *Classification and Morphology of External Galaxies.* Handbuch der Physik (1959). Cited on page 5.

[17] A. R. Sandage. *The Hubble atlas of galaxies.* Washington: Carnegie Institution (1961). Cited on page 5.

[18] E. F. Bell and R. S. de Jong. *Stellar Mass-to-Light Ratios and the Tully-Fisher Relation.* Astrophysical Journal **550** 212 (2001). arXiv:astro-ph/0011493. Cited on page 6.

[19] S. Courteau, M. Cappellari, R. S. de Jong, A. A. Dutton, E. Emsellem, H. Hoekstra, L. V. E. Koopmans, G. A. Mamon, C. Maraston, T. Treu, and L. M. Widrow. *Galaxy masses.* Reviews of Modern Physics **86** 47 (2014). arXiv:1309.3276. Cited on pages 6 and 7.

[20] J. Binney and S. Tremaine. *Galactic dynamics.* 2 edition 1994. Cited on pages 6 and 7.

[21] A. J. Moffett, R. Lange, S. P. Driver, A. S. Robotham, L. S. Kelvin, M. Alpaslan, S. K. Andrews, J. Bland-Hawthorn, S. Brough, M. E. Cluver, et al. *Galaxy and Mass Assembly (GAMA): the stellar mass budget of galaxy spheroids and discs.* Monthly Notices of the Royal Astronomical Society **462** 4336 (2016). Cited on page 6.

[22] S. E. Meidt, E. Schinnerer, G. van de Ven, D. Zaritsky, R. Peletier, J. H. Knapen, K. Sheth, M. Regan, M. Querejeta, J.-C. Muñoz-Mateos, T. Kim, J. L. Hinz, A. Gil de Paz, E. Athanassoula, A. Bosma, R. J. Buta, M. Cisternas, L. C. Ho, B. Holwerda, R. Skibba, E. Laurikainen, H. Salo, D. A. Gadotti, J. Laine, S. Erroz-Ferrer, S. Comerón, K. Menéndez-Delmestre, M. Seibert, and T. Mizusawa. *Reconstructing the Stellar Mass Distributions of Galaxies Using S^4G IRAC 3.6 and 4.5 μm Images. II. The Conversion from Light to Mass.* Astrophysical Journal **788** 144 (2014). arXiv:1402.5210. Cited on pages 6, 23, and 27.

[23] J. L. Sersic. *Atlas de galaxias australes.* 1968. Cited on page 6.

[24] G. A. Mamon and E. L. Łokas. *Dark matter in elliptical galaxies - II. Estimating the mass within the virial radius.* MNRAS **363** 705 (2005). arXiv:astro-ph/0405491. Cited on page 7.

[25] M. Cappellari, E. Emsellem, D. Krajnović, R. M. McDermid, N. Scott, G. A. Verdoes Kleijn, L. M. Young, K. Alatalo, R. Bacon, L. Blitz, M. Bois, F. Bournaud, M. Bureau, R. L. Davies, T. A. Davis, P. T. de Zeeuw, P.-A. Duc, S. Khochfar, H. Kuntschner, P.-Y. Lablanche, R. Morganti, T. Naab, T. Oosterloo, M. Sarzi, P. Serra, and A.-M. Weijmans. *The ATLAS3D project – I. A volume-limited sample of 260 nearby early-type galaxies: science goals and selection criteria.* Monthly Notices of the Royal Astronomical Society **413** 813 (2011). URL: https://doi.org/10.1111/j.1365-2966.2010.18174.x arXiv:https://academic.oup.com/mnras/article-pdf/413/2/813/18746669/mnras0413-0813.pdf. Cited on page 7.

[26] Y. Sofue and V. Rubin. *Rotation Curves of Spiral Galaxies.* ARA&A **39** 137 (2001). arXiv:astro-ph/0010594. Cited on page 7.

[27] F. Walter, E. Brinks, W. J. G. de Blok, F. Bigiel, J. Kennicutt,Robert C., M. D. Thornley, and A. Leroy. *THINGS: The H I Nearby Galaxy Survey.* AJ **136** 2563 (2008). arXiv:0810.2125. Cited on page 7.

[28] W. J. G. de Blok, F. Fraternali, G. H. Heald, E. A. K. Adams, A. Bosma, B. S. Koribalski, and the HI Science Working Group. *The SKA view of the Neutral Interstellar Medium in Galaxies.* arXiv e-prints page arXiv:1501.01211 (2015). arXiv:1501.01211. Cited on page 7.

[29] K. G. Begeman. *HI rotation curves of spiral galaxies. I. NGC 3198.* Astronomy and Astrophysics **223** 47 (1989). Cited on page 7.

[30] G. I. G. Józsa, F. Kenn, T. A. Oosterloo, and U. Klein. *TiRiFiC: Tilted Ring Fitting Code.* Astrophysics Source Code Library, record ascl:1208.008 2012. arXiv:1208.008. Cited on page 7.

[31] E. M. Di Teodoro and F. Fraternali. ^{3D} *BAROLO: a new 3D algorithm to derive rotation curves of galaxies.* Monthly Notices of the RAS **451** 3021 (2015). arXiv:1505.07834. Cited on pages 7 and 9.

[32] F. Zwicky. *Die Rotverschiebung von extragalaktischen Nebeln.* Helvetica Physica Acta **6** 110 (1933). Cited on page 7.

[33] J. H. Oort. *Some Problems Concerning the Structure and Dynamics of the Galactic System and the Elliptical Nebulae NGC 3115 and 4494.* Astrophysical Journal **91** 273 (1940). Cited on page 8.

[34] D. Clowe, M. Bradač, A. H. Gonzalez, M. Markevitch, S. W. Randall, C. Jones, and D. Zaritsky. *A Direct Empirical Proof of the Existence of Dark Matter.* Astrophysical Journal **648** L109 (2006). arXiv:astro-ph/0608407. Cited on page 8.

[35] A. Burkert. *The Structure of Dark Matter Halos in Dwarf Galaxies.* Astrophysical Journal **447** L25 (1995). arXiv:astro-ph/9504041. Cited on pages 8 and 32.

[36] J. F. Navarro, C. S. Frenk, and S. D. M. White. *The Structure of Cold Dark Matter Halos.* Astrophysical Journal **462** 563 (1996). arXiv:astro-ph/9508025. Cited on pages 9 and 47.

[37] V. Marra, D. C. Rodrigues, and Á. O. F. de Almeida. *A fundamental test for MOND.* Monthly Notices of the RAS **494** 2875 (2020). arXiv:2002.03946. Cited on pages 10, 35, 41, and 45.

[38] J. Kormendy and R. C. Kennicutt Jr. *Secular evolution and the formation of pseudobulges in disk galaxies.* Annual Reviews of Astronomy and Astrophysics **42** 603 (2004). Cited on page 11.

[39] P. Erwin, R. P. Saglia, M. Fabricius, J. Thomas, N. Nowak, S. Rusli, R. Bender, J. C. Vega Beltrán, and J. E. Beckman. *Composite bulges: the coexistence of classical bulges and discy pseudo-bulges in S0 and spiral galaxies.* Monthly Notices of the Royal Astronomical Society **446** 4039 (2015). Cited on page 11.

[40] S. S. McGaugh, F. Lelli, and J. M. Schombert. *Scaling Relations for Molecular Gas and Metallicity: Impact on the Baryonic Tully–Fisher Relation.* Research Notes of the AAS **4** 45 (2020). URL: https://dx.doi.org/10.3847/2515-5172/ab8471. Cited on page 11.

[41] M. A. Bershady, M. A. Verheijen, R. A. Swaters, D. R. Andersen, K. B. Westfall, and T. Martinsson. *The DiskMass survey. I. overview.* The Astrophysical Journal **716** 198 (2010). Cited on page 12.

[42] M. W. Grootes and S. P. o. Driver. *Galaxy And Mass Assembly (GAMA): Gas Fueling of Spiral Galaxies in the Local Universe. I. The Effect of the Group Environment on Star Formation in Spiral Galaxies.* Astronomical Journal **153** 111 (2017). arXiv:1612.07322. Cited on page 13.

[43] F. Lelli, S. S. McGaugh, and J. M. Schombert. *The small scatter of the baryonic Tully–Fisher relation.* The Astrophysical Journal Letters **816** L14 (2016). Cited on page 13.

[44] A. Di Cintio and F. Lelli. *The mass discrepancy acceleration relation in a ΛCDM context.* Monthly Notices of the Royal Astronomical Society: Letters **456** L127 (2015). Cited on page 13.

[45] H. Katz, F. Lelli, S. S. McGaugh, A. Di Cintio, C. B. Brook, and J. M. Schombert. *Testing feedback-modified dark matter haloes with galaxy rotation curves: estimation of halo parameters and consistency with ΛCDM scaling relations.* Monthly Notices of the Royal Astronomical Society **466** 1648 (2017). Cited on page 13.

[46] K. Sheth, M. Regan, J. L. Hinz, A. G. De Paz, K. Menéndez-Delmestre, J.-C. Muñoz-Mateos, M. Seibert, T. Kim, E. Laurikainen, H. Salo, et al. *The Spitzer Survey of Stellar Structure in Galaxies (S^4G).* Publications of the Astronomical Society of the Pacific **122** 1397 (2010). Cited on page 14.

[47] P. Serra, T. Oosterloo, R. Morganti, K. Alatalo, L. Blitz, M. Bois, F. Bournaud, M. Bureau, M. Cappellari, A. F. Crocker, et al. *The ATLAS3D project–XIII. Mass and morphology of H i in early-type galaxies as a function of environment.* Monthly Notices of the Royal Astronomical Society **422** 1835 (2012). Cited on page 15.

[48] M. Den Heijer, T. A. Oosterloo, P. Serra, G. I. Józsa, J. Kerp, R. Morganti, M. Cappellari, T. A. Davis, P.-A. Duc, E. Emsellem, et al. *The H I Tully-Fisher relation of early-type galaxies.* Astronomy and Astrophysics **581** A98 (2015). Cited on page 15.

[49] B. García-Lorenzo, I. Márquez, J. Barrera-Ballesteros, J. Masegosa, B. Husemann, J. Falcón-Barroso, M. Lyubenova, S. Sánchez, J. Walcher, D. Mast, et al. *Ionized gas kinematics of galaxies in the CALIFA survey-I. Velocity fields, kinematic parameters of the dominant component, and presence of kinematically distinct gaseous systems.* Astronomy and Astrophysics **573** A59 (2015). Cited on page 15.

[50] K. Bundy, M. A. Bershady, D. R. Law, R. Yan, N. Drory, N. MacDonald, D. A. Wake, B. Cherinka, J. R. Sánchez-Gallego, A.-M. Weijmans, et al. *Overview of the SDSS-IV MaNGA survey: mapping nearby galaxies at Apache Point observatory.* The Astrophysical Journal **798** 7 (2014). Cited on page 15.

[51] S. Casertano. *Rotation curve of the edge-on spiral galaxy NGC 5907 : disc and halo masses.* Monthly Notices of the RAS **203** 735 (1983). Cited on page 17.

[52] H. Katz, F. Lelli, S. S. McGaugh, A. Di Cintio, C. B. Brook, and J. M. Schombert. *Testing feedback-modified dark matter haloes with galaxy rotation curves: estimation of halo parameters and consistency with ΛCDM scaling relations.* Monthly Notices of the RAS **466** 1648 (2017). arXiv:1605.05971. Cited on pages 18, 38, and 63.

[53] A. Di Cintio, C. B. Brook, A. A. Dutton, A. V. Macciò, G. S. Stinson, and A. Knebe. *A mass-dependent density profile for dark matter haloes including the influence of galaxy formation.* Monthly Notices of the RAS **441** 2986 (2014). arXiv:1404.5959. Cited on pages 20, 31, 38, and 39.

[54] D. C. Rodrigues, A. Hernández-Arboleda, and A. Wojnar. *Normalized additional velocity distribution: Testing the radial profile of dark matter halos and MOND.* Physics of the Dark Universe **41** 101230 (2023). arXiv:2204.03762. Cited on pages 22, 24, 25, 30, 33, 37, 39, 40, 42, 45, and 50.

[55] S. S. McGaugh, W. J. G. de Blok, J. M. Schombert, R. Kuzio de Naray, and J. H. Kim. *The Rotation Velocity Attributable to Dark Matter at Intermediate Radii in Disk Galaxies.* Astrophysical Journal **659** 149 (2007). arXiv:astro-ph/0612410. Cited on pages 22 and 63.

[56] S. S. McGaugh, F. Lelli, and J. M. Schombert. *Radial Acceleration Relation in Rotationally Supported Galaxies.* Physical Review Letters **117** 201101 (2016). arXiv:1609.05917. Cited on pages 23, 35, 37, and 41.

[57] B. W. Silverman. *Density estimation for statistics and data analysis.* Chapman & Hall/CRC 1998. Cited on page 24.

[58] D. W. Scott. *Multivariate density estimation: theory, practice, and visualization.* Wiley 2 edition 2014. Cited on page 24.

[59] M. Milgrom. *A modification of the Newtonian dynamics as a possible alternative to the hidden mass hypothesis.* Astrophysical Journal **270** 365 (1983). Cited on pages 26 and 35.

[60] S. S. McGaugh and J. M. Schombert. *Color-Mass-to-light-ratio Relations for Disk Galaxies.* Astronomical Journal **148** 77 (2014). arXiv:1407.1839. Cited on page 27.

[61] P. C. Gregory. *Bayesian Logical Data Analysis for the Physical Sciences: A Comparative Approach with 'Mathematica' Support.* 2010. Cited on page 28.

[62] K. Price, R. M. Storn, and J. A. Lampinen. *Differential Evolution: A Practical Approach to Global Optimization (Natural Computing Series).* Springer 2006. Cited on page 28.

[63] S. Courteau. *Optical Rotation Curves and Linewidths for Tully-Fisher Applications.* Astronomical Journal **114** 2402 (1997). arXiv:astro-ph/9709201. Cited on page 28.

[64] H. Mo, F. C. van den Bosch, and S. White. *Galaxy Formation and Evolution.* 2010. Cited on page 31.

[65] W. J. G. de Blok. *The Core-Cusp Problem.* Advances in Astronomy **2010** 789293 (2010). arXiv:0910.3538. Cited on page 31.

[66] F. Governato, A. Zolotov, A. Pontzen, C. Christensen, S. H. Oh, A. M. Brooks, T. Quinn, S. Shen, and J. Wadsley. *Cuspy no more: how outflows affect the central dark matter and baryon distribution in Λ cold dark matter galaxies.* Monthly Notices of the RAS **422** 1231 (2012). arXiv:1202.0554. Cited on page 31.

[67] K. A. Oman, J. F. Navarro, A. Fattahi, C. S. Frenk, T. Sawala, S. D. M. White, R. Bower, R. A. Crain, M. Furlong, M. Schaller, J. Schaye, and T. Theuns. *The unexpected diversity of dwarf galaxy rotation curves.* Monthly Notices of the RAS **452** 3650 (2015). arXiv:1504.01437. Cited on page 31.

[68] A. Del Popolo and M. Le Delliou. *Small Scale Problems of the ΛCDM Model: A Short Review.* Galaxies **5** 17 (2017). arXiv:1606.07790. Cited on page 31.

[69] A. A. Dutton, A. V. Macciò, A. Obreja, and T. Buck. *NIHAO - XVIII. Origin of the MOND phenomenology of galactic rotation curves in a ΛCDM universe.* Monthly Notices of the RAS **485** 1886 (2019). arXiv:1902.06751. Cited on pages 31 and 35.

[70] M. Frosst, S. Courteau, N. Arora, C. Stone, A. V. Macciò, and M. Blank. *The diversity of spiral galaxies explained.* Monthly Notices of the RAS **514** 3510 (2022). arXiv:2204.02412. Cited on page 31.

[71] P. Salucci and A. Burkert. *Dark Matter Scaling Relations.* Astrophysical Journal **537** L9 (2000). arXiv:astro-ph/0004397. Cited on page 32.

[72] P. Salucci, A. Lapi, C. Tonini, G. Gentile, I. Yegorova, and U. Klein. *The universal rotation curve of spiral galaxies - II. The dark matter distribution out to the virial radius.* Monthly Notices of the RAS **378** 41 (2007). arXiv:astro-ph/0703115. Cited on page 32.

[73] D. C. Rodrigues, A. del Popolo, V. Marra, and P. L. C. de Oliveira. *Evidence against cuspy dark matter haloes in large galaxies.* Monthly Notices of the RAS **470** 2410 (2017). arXiv:1701.02698. Cited on page 32.

[74] P. Li, F. Lelli, S. McGaugh, and J. Schombert. *A Comprehensive Catalog of Dark Matter Halo Models for SPARC Galaxies.* Astrophysical Journals **247** 31 (2020). arXiv:2001.10538. Cited on pages 32, 38, 40, 41, 46, 51, 52, and 63.

[75] B. Famaey and S. S. McGaugh. *Modified Newtonian Dynamics (MOND): Observational Phenomenology and Relativistic Extensions.* Living Reviews in Relativity **15** 10 (2012). arXiv:1112.3960. Cited on page 35.

[76] S. S. McGaugh, P. Li, F. Lelli, and J. M. Schombert. *Presence of a fundamental acceleration scale in galaxies.* Nature Astronomy **2** 924 (2018). Cited on page 35.

[77] P. Kroupa, I. Banik, H. Haghi, A. H. Zonoozi, J. Dabringhausen, B. Javanmardi, O. Müller, X. Wu, and H. Zhao. *A common Milgromian acceleration scale in nature.* Nature Astronomy **2** 925 (2018). arXiv:1811.11754. Cited on page 35.

[78] D. C. Rodrigues, V. Marra, A. Del Popolo, and Z. Davari. *Reply to 'Presence of a fundamental acceleration scale in galaxies' and 'A common Milgromian acceleration scale in nature'.* Nature Astronomy **2** 927 (2018). arXiv:1811.05882. Cited on pages 35 and 41.

[79] E. Cameron, G. W. Angus, and J. M. Burgess. *Overconfidence in Bayesian analyses of galaxy rotation curves.* Nature Astronomy **4** 132 (2020). Cited on page 35.

[80] D. C. Rodrigues, V. Marra, A. Del Popolo, and Z. Davari. *Reply to: Overconfidence in Bayesian analyses of galaxy rotation curves.* Nature Astronomy **4** 134 (2020). arXiv:2002.01970. Cited on page 35.

[81] D. C. Rodrigues and V. Marra. *The radial acceleration relation and its emergent nature.* In T. Storchi Bergmann, W. Forman, R. Overzier, and R. Riffel, editors, *Galaxy Evolution and Feedback across Different Environments* volume 359 pages 457–459 2021. arXiv:2005.12384. Cited on page 35.

[82] P. Li, F. Lelli, S. McGaugh, J. Schombert, and K.-H. Chae. *A cautionary tale in fitting galaxy rotation curves with Bayesian techniques. Does Newton's constant vary from galaxy to galaxy?* Astronomy and Astrophysics **646** L13 (2021). arXiv:2101.11644. Cited on page 35.

[83] Z. Chang and Y. Zhou. *Is there a fundamental acceleration scale in galaxies?* Monthly Notices of the RAS **486** 1658 (2019). arXiv:1812.05002. Cited on page 35.

[84] C. Stone and S. Courteau. *The Intrinsic Scatter of the Radial Acceleration Relation.* Astrophysical Journal **882** 6 (2019). arXiv:1908.06105. Cited on page 35.

[85] T. Ren, A. Kwa, M. Kaplinghat, and H.-B. Yu. *Reconciling the Diversity and Uniformity of Galactic Rotation Curves with Self-Interacting Dark Matter.* Physical Review X **9** 031020 (2019). arXiv:1808.05695. Cited on pages 35 and 63.

[86] Y. Zhou, A. Del Popolo, and Z. Chang. *On the absence of a universal surface density, and a maximum Newtonian acceleration in dark matter haloes: Consequences for MOND.* Physics of the Dark Universe **28** 100468 (2020). arXiv:2008.04065. Cited on page 35.

[87] M. H. Eriksen, M. T. Frandsen, and M. H. From. *A cusp-core-like challenge for modified Newtonian dynamics.* Astronomy and Astrophysics **656** A123 (2021). Cited on pages 35 and 63.

[88] J. F. Navarro, A. Benítez-Llambay, A. Fattahi, C. S. Frenk, A. D. Ludlow, K. A. Oman, M. Schaller, and T. Theuns. *The origin of the mass discrepancy-acceleration relation in ΛCDM.* Monthly Notices of the RAS **471** 1841 (2017). arXiv:1612.06329. Cited on page 35.

[89] M. Kaplinghat, T. Ren, and H.-B. Yu. *Dark matter cores and cusps in spiral galaxies and their explanations.* Journal of Cosmology and Astroparticle Physics **2020** 027 (2020). arXiv:1911.00544. Cited on page 35.

[90] B. P. Moster, T. Naab, and S. D. M. White. *Galactic star formation and accretion histories from matching galaxies to dark matter haloes.* Monthly Notices of the RAS **428** 3121 (2013). arXiv:1205.5807. Cited on page 38.

[91] G. Gentile, P. Salucci, U. Klein, D. Vergani, and P. Kalberla. *The cored distribution of dark matter in spiral galaxies.* Monthly Notices of the RAS **351** 903 (2004). arXiv:astro-ph/0403154. Cited on page 41.

[92] D. C. Rodrigues, P. L. de Oliveira, J. C. Fabris, and G. Gentile. *Modified gravity models and the central cusp of dark matter haloes in galaxies.* Monthly Notices of the RAS **445** 3823 (2014). arXiv:1409.7524. Cited on page 41.

[93] P. Li, F. Lelli, S. McGaugh, and J. Schombert. *Fitting the radial acceleration relation to individual SPARC galaxies.* Astronomy and Astrophysics **615** A3 (2018). arXiv:1803.00022. Cited on page 41.

[94] J. D. Toniato, D. C. Rodrigues, and A. Wojnar. *Palatini f (R) gravity in the solar system: Post-Newtonian equations of motion and complete PPN parameters.* Physical Review D **101** 064050 (2020). arXiv:1912.12234. Cited on page 43.

[95] A. Hernández-Arboleda, D. C. Rodrigues, J. D. Toniato, and A. Wojnar. *Palatini f(R) gravity tests in weak field limit: Solar system, seismology and galaxies.* International Journal of Geometric Methods in Modern Physics **0** 2450028 (2023). URL: https://doi.org/10.1142/S0219887824500282 arXiv:https://doi.org/10.1142/S0219887824500282. Cited on page 44.

[96] T. Kobayashi, Y. Watanabe, and D. Yamauchi. *Breaking of Vainshtein screening in scalar-tensor theories beyond Horndeski.* Physical Review D **91** 064013 (2015). arXiv:1411.4130. Cited on page 46.

[97] A. I. Vainshtein. *To the problem of nonvanishing gravitation mass.* Physics Letters B **39** 393 (1972). Cited on page 46.

[98] A. Joyce, B. Jain, J. Khoury, and M. Trodden. *Beyond the cosmological standard model.* Physics Reports **568** 1 (2015). arXiv:1407.0059. Cited on page 46.

[99] B. Falck, K. Koyama, and G.-B. Zhao. *Cosmic web and environmental dependence of screening: Vainshtein vs. chameleon.* Journal of Cosmology and Astroparticle Physics **2015** 049 (2015). arXiv:1503.06673. Cited on page 46.

[100] K. Koyama and J. Sakstein. *Astrophysical probes of the Vainshtein mechanism: Stars and galaxies.* Physical Review D **91** 124066 (2015). arXiv:1502.06872. Cited on pages 46, 47, and 48.

[101] J. Gleyzes, D. Langlois, F. Piazza, and F. Vernizzi. *New Class of Consistent Scalar-Tensor Theories.* Physical Review Letters **114** 211101 (2015). arXiv:1404.6495. Cited on page 46.

[102] D. Langlois and K. Noui. *Degenerate higher derivative theories beyond Horndeski: evading the Ostrogradski instability.* Journal of Cosmology and Astroparticle Physics **2016** 034 (2016). arXiv:1510.06930. Cited on page 47.

[103] R. Saito, D. Yamauchi, S. Mizuno, J. Gleyzes, and D. Langlois. *Modified gravity inside astrophysical bodies.* Journal of Cosmology and Astroparticle Physics **2015** 008 (2015). arXiv:1503.01448. Cited on page 47.

[104] J. Sakstein. *Hydrogen Burning in Low Mass Stars Constrains Scalar-Tensor Theories of Gravity.* Physical Review Letters **115** 201101 (2015). arXiv:1510.05964. Cited on page 47.

[105] E. Laudato, V. Salzano, and K. Umetsu. *Multicomponent DHOST analysis in galaxy clusters.* Monthly Notices of the RAS **511** 1878 (2022). arXiv:2110.11019. Cited on page 47.

[106] S. Chowdhury and T. Sarkar. *The Schönberg-Chandrasekhar limit in presence of small anisotropy and modified gravity.* Monthly Notices of the RAS **523** 518 (2023). arXiv:2209.07389. Cited on page 47.

[107] I. D. Saltas and J. Christensen-Dalsgaard. *Searching for dark energy with the Sun.* Astronomy and Astrophysics **667** A115 (2022). arXiv:2205.14134. Cited on page 47.

[108] F. Piazza and C. Marinoni. *Model for Gravitational Interaction between Dark Matter and Baryons*. Physical Review Letters **91** 141301 (2003). arXiv:hep-ph/0304228. Cited on page 47.

[109] F. Schmidt, M. Lima, H. Oyaizu, and W. Hu. *Nonlinear evolution of f(R) cosmologies. III. Halo statistics*. Physical Review D **79** 083518 (2009). arXiv:0812.0545. Cited on page 47.

[110] V. F. Cardone and S. Capozziello. *Systematic biases on galaxy haloes parameters from Yukawa-like gravitational potentials*. Monthly Notices of the RAS **414** 1301 (2011). arXiv:1102.0916. Cited on page 47.

[111] H. Wilcox, R. C. Nichol, G.-B. Zhao, D. Bacon, K. Koyama, and A. K. Romer. *Simulation tests of galaxy cluster constraints on chameleon gravity*. Monthly Notices of the RAS **462** 715 (2016). arXiv:1603.05911. Cited on page 47.

[112] A. P. Naik, E. Puchwein, A.-C. Davis, and C. Arnold. *Imprints of Chameleon f(R) gravity on Galaxy rotation curves*. Monthly Notices of the RAS **480** 5211 (2018). arXiv:1805.12221. Cited on page 47.

[113] Á. de Almeida, L. Amendola, and V. Niro. *Galaxy rotation curves in modified gravity models*. Journal of Cosmology and Astroparticle Physics **2018** 012 (2018). arXiv:1805.11067. Cited on page 47.

[114] A. P. Naik, E. Puchwein, A.-C. Davis, D. Sijacki, and H. Desmond. *Constraints on chameleon f(R)-gravity from galaxy rotation curves of the SPARC sample*. Monthly Notices of the RAS **489** 771 (2019). arXiv:1905.13330. Cited on page 47.

[115] J. Henrichs, M. Lembo, F. Iocco, and L. Amendola. *Testing gravity with the Milky Way: Yukawa potential*. Physical Review D **104** 043009 (2021). arXiv:2010.15190. Cited on page 47.

[116] L. Pizzuti, I. D. Saltas, K. Umetsu, and B. Sartoris. *Probing vainsthein-screening gravity with galaxy clusters using internal kinematics and strong and weak lensing*. Monthly Notices of the RAS **512** 4280 (2022). arXiv:2112.12139. Cited on page 47.

[117] D. Foreman-Mackey, D. W. Hogg, D. Lang, and J. Goodman. *emcee: The MCMC Hammer*. Publications of the ASP **125** 306 (2013). arXiv:1202.3665. Cited on page 52.

[118] R. E. Kass and A. E. Raftery. *Bayes Factors*. Journal of the American Statistical Association **90** 773 (1995). URL: https://www.tandfonline.com/doi/abs/10.1080/01621459.1995.10476572 arXiv:https://www.tandfonline.com/doi/pdf/10.1080/01621459.1995.10476572. Cited on page 55.

[119] D. C. Rodrigues, P. S. Letelier, and I. L. Shapiro. *Galaxy rotation curves from general relativity with renormalization group corrections*. Journal of Cosmology and Astroparticle Physics **2010** 020 (2010). arXiv:0911.4967. Cited on page 63.

[120] D. C. Rodrigues, P. S. Letelier, and I. L. Shapiro. *Galaxy Rotation Curves from General Relativity with Infrared Renormalization Group Effects*. arXiv e-prints page arXiv:1102.2188 (2011). arXiv:1102.2188. Cited on page 63.

[121] K. G. Begeman, A. H. Broeils, and R. H. Sanders. *Extended rotation curves of spiral galaxies : dark haloes and modified dynamics.* Monthly Notices of the RAS **249** 523 (1991). Cited on page 63.

[122] M. A. Green and J. W. Moffat. *Modified Gravity (MOG) fits to observed radial acceleration of SPARC galaxies.* Physics of the Dark Universe **25** 100323 (2019). arXiv:1905.09476. Cited on page 64.